PHOTOACOUSTIC IMAGING IN THE NIR-II WINDOW USING SEMICONDUCTING POLYMERS

by

Jiayingzi Wu

A Dissertation

Submitted to the Faculty of Purdue University

In Partial Fulfillment of the Requirements for the degree of

Doctor of Philosophy

Department of Chemistry

West Lafayette, Indiana

May 2020

THE PURDUE UNIVERSITY GRADUATE SCHOOL

STATEMENT OF COMMITTEE APPROVAL

Dr. Jianguo Mei, Chair

Department of Chemistry

Dr. Ji-Xin Cheng

Department of Chemistry

Dr. Shelley Claridge

Department of Chemistry

Dr. Chengde Mao

Department of Chemistry

Approved by:

Dr. Christine A. Hrycyna

This dissertation is dedicated to my loving and supportive advisors, friends, and family.

ACKNOWLEDGMENTS

I would like to thank my co-advisors Prof. Jianguo Mei and Prof. Ji-Xin Cheng for their research guidance and continuous support in my Ph.D. study. I wholeheartedly thank Dr. Mei for supporting me through all the new challenges and adventures, inspiring me with new ideas and monitoring me to be an independent scientist. I also deeply thank Dr. Ji-Xin Cheng whose passion, curiosity, creativity, and persistence on research strongly inspires me and guides me to pursue my academic career.

I am also grateful to have Prof. Chengde Mao, Prof. Shelley Claridge to be my advisory committees, who have been offering their valuable advice and supports on my research in the past years. In addition, I would like to thank all the current and former group members, who I have had great pleasure working with. In particular, I would like to thank Dr. Hyeon-Jeong Lee, Dr. Kai-Chih Huang, Dr. Lu Lan, Dr. Rui Li, Dr. Liyan You, Dr. Jiazhi He, Xuyi Luo, Saadia Chaudhry, Peng Lin for their insightful comments or significant contributions to my research. I also appreciate helps from Dr. Pu Wang, Dr. Junjie Li, Dr. Brittani Bungart, Dr. Yingchun Cao, Dr. Delong Zhang, Dr. Chi Zhang, Dr. Fengyuan (Max) Deng, Yifan Zhu, and Dr. Cheng Zong.

Furthermore, I thank Prof. Timothy Ratliff, Prof. Minoru Ashizawa for the great collaborations that lead to fruitful research achievements. I also thank Dr. Ben Elzey, Sandra Torregrosa-Allen, and Melanie Currie for their technical support.

Finally, I give my greatest appreciation to my boyfriend and colleague, Jiazhi He, for his unlimited support and love. I also thank my parents for their unconditional support and love.

TABLE OF CONTENTS

LIST OF FIGURES

LIST OF ABBREVIATIONS

ANSI	American National Standards Institute
AOM	acousto-optic modulator
ATCC	American Type Culture Collection
AUC	area under curve
BTII	bis-isoindigo
BV	blood vessel
CCD	charge coupled device
CDI	1,1'-Carbonyldiimidazole
CO2	carbon dioxide
CT	computed tomography
DCM	dichloromethane
DI	deionized
DIPEA	N,N-diisopropylethylamine,
DLS	dynamic light scattering
DM	dichromic mirror
DMEM	Dulbecco's Modified Eagle Medium
DSPE-PEG	1,2-distearoyl-sn-glycero-3-phosphoethanolamine-N-[methoxy(polyethylene glycol)-2000]
DUPA	2-[3-(1,3-dicarboxypropyl) ureido] pentanedioic acid
EDOT	3,4-ethylenedioxythiophene
EPR	enhanced permeability and retention
F	filter

FBS	fetal bovine serum
FG	function generator
FWHM	neutral-density
GM	galvo mirror
GPC	gel permeation chromatography
HFB	human fibroblast
HOMO	highest occupied molecular orbital
HWP	half-wave plate
IR	infrared
ITO	Indium tin oxide
LASSO	least absolute shrinkage and selection operator
LUMO	lowest unoccupied molecular orbital
MB	methylene blue
MEM	Minimum Essential Medium
MPE	maximum exposure energy
MRI	magnetic resonance imaging
MS	motorized stage
MTS	(3-(4,5-dimethylthiazol-2-yl)-5-(3-carboxymethoxyphenyl)-2-(4-sulfophenyl)-2H-tetrazolium)
MTT	(4,5-dimethylthiazol-2-yl)-2,5-diphenyl tetrazolium bromide
NA	numerical aperture
ND	neutral-density
NIR-I	first near-infrared
NIR-II	second near-infrared

NMR	nuclear magnetic resonance
NP	nanoparticle
NSG	NOD scid gamma
OPO	optical parametric oscillator
PA	photoacoustic
PBS	phosphate Buffered Saline
PBS	polarization beam splitter
PC	personal computer
PD	photodiode
PE	poly(ProDOT-EDOT)
PEG	polyethylene glycol
PES	polyethersulfone
PET	positron emission tomography
PMPA	2-(Phosphonomethyl)pentanedioic acid
PSA	prostate-Specific Antigen
PSMA	prostate-specific membrane antigen
RC	resonant circuit
RES	reticuloendothelial system
RMS	root mean square
ROI	region of interest
RPMI	Roswell Park Memorial Institute
SNR	single to noise ratio
SP	semiconducting polymer

SPECT	single-photon emission computed tomography
SPN	semiconducting polymer nanoparticle
MB-SPS	MBraun solvent purification system
SRS	stimulated Raman scattering
TA	transient absorption
TEG	triethylene glycol
TEM	transmission electron microscopy
TFA	trifluoroacetic acid
THF	tetrahydrofuran
TII	thienoisoindigo
TSPN	thienoisoindigo-based semiconducting polymer nanoparticles
US	ultrasound
UV	ultraviolet
VIS	visible
BTII-DUPA	bis-isoindigo-based semiconducting polymer nanoparticles functionalized with 2-[3-(1,3-dicarboxypropyl) ureido] pentanedioic acid

ABSTRACT

Molecular imaging revolutionized the way researchers and clinicians visualize and investigate complex biochemical phenomena, and it is beneficial for disease diagnosis, drug design and therapy assessment. Among a variety of different imaging techniques, the non-ionizing and non-invasive photoacoustic (PA) imaging is attracting increased attentions, owing to its high spatial and temporal resolutions with reasonable penetration depth in tissue. Parallel efforts have been the preparation of PA imaging agents which has high PA efficacy and can specifically label the targets at cellular or molecular level. Particularly, there is exponentially growing interest in imaging in the second near-infrared (NIR-II) window (1000–1700 nm), where offers reduced tissue background and improved penetration depth. However, study of PA imaging in the NIR-II window is incomplete, partly due to the lack of suitable materials. Therefore, in my dissertation work I studied NIR-II PA imaging through semiconducting polymer.

Firstly, the performance of PA imaging in the NIR-II window is explored by using a semiconducting polymer nanoparticle (SPN) which has strong absorption in the NIR-II window. Compared with lipid, blood and water, such SPN shows outstanding PA contrast in the NIR-II window *in situ* and *in vivo*, and an imaging depth of more than 5 cm at 1064 nm excitation is achieved in chicken-breast tissue. These results suggest that SPN as a PA contrast in the NIR-II window opens new opportunities for biomedical imaging with improved imaging contrast and centimeter-deep imaging depth.

Next, targeted PA imaging of prostate cancer is achieved by functionalizing a NIR-II absorbing SPN with prostate-specific membrane antigen (PSMA)-targeted ligands. Insights into the interaction of the imaging probes with the biological targets are obtained from single-cell to whole-organ by transient absorption (TA) microscopy and PA imaging. TA microscopy reveals

the targeting efficiency, kinetics, and specificity of the functionalized SPN to PSMA-positive prostate cancer at cellular level. Meanwhile, the functionalized SPN demonstrates selective accumulation and retention in the PSMA-positive tumor after intravenous administration *in vivo*. Taken together, it is demonstrated that BTII-DUPA SPN is a promising targeted probe for prostate cancer diagnosis by PA imaging.

Lastly, PA imaging in the NIR-II window is also achieved water-soluble semiconducting polymer, which is prepared by oxygen-doping. After doping, it shows broadband absorption in the entire NIR-II window, with great chemical stability, photostability and biocompatibility. Owing to its merit of broadband absorption, the imaging depth comparison among different NIR-II wavelengths is also achieved. Moreover, this doped semiconducting polymer is readily soluble in normal physiological pH by virtue of carboxyl groups on side chains and tends to aggregate at an acidic environment which results in a 7.6-fold PA enhancement at pH 5.0. Importantly, a 3.4±1.0-fold greater signal in tumor tissue than that in muscle is revealed *in vivo*. This study provides a more attainable yet effective platform to the field for achieving water-soluble NIR-II absorbing contrast agents for activatable PA imaging.

CHAPTER 1. INTRODUCTION

1.1 Molecular Imaging and Cancer

Cancer is a major public health problem worldwide and is the second leading cause of death in the United States.[1] In 2020, there will be approximately 1,806,590 new cancer cases diagnosed and 606,520 American will die from cancer.[1] Therefore, there is an crucial need to develop effective cancer prevention, early detection, and treatment strategies.

Molecular imaging plays an important role in accelerating the progress against cancer, as it revolutionized the way researchers and clinicians visualize and investigate complex biochemical phenomena.[2, 3] Molecular imaging is defined as the noninvasive, real-time visualization of physiological or pathological process at the cellular and molecular level within living subjects.[2-4] It requires specified imaging techniques which alone or in combination with targeted imaging agents can identify specific biomedical events at molecular level.[2] Hence, multidisciplinary efforts have been devoted to the field of molecular imaging, including imaging techniques, biology, chemistry, nanotechnology, physics, mathematics, pharmacology, genetics and medicine.[2]

1.2 Limitations of Conventional Imaging Modalities

The molecular imaging has its roots back to nuclear medicine including single-photon emission computed tomography (SPECT) and positron emission tomography (PET), and now is tailored to many other imaging modalities, such as computed tomography (CT), ultrasound imaging (US), magnetic resonance imaging (MRI) and optical imaging.[2]

Those conventional clinical imaging modalities (CT, SPECT, PET, MRI and US) have limitless penetration for diagnosis.[2] Yet, they show certain drawbacks, such as being ionizing

radiative (for CT, PET, and SPECT), poor-soft tissue contrast (for CT), limited spatial resolution (for US, MRI, SPECT, and PET), long acquisition time for (MRI) and the high cost (for CT, PET, SPECT and MRI).[2, 5] On the other hand, the translational applications of conventional optical imaging modalities (e.g. confocal microscope, two-photon microscopy, optical coherent tomography) are limited by the penetration of ballistic and quasi-ballistic photons in tissue.[6]

1.3 Photoacoustic (PA) Imaging Modality

1.3.1 The Principle of PA Imaging

PA imaging is emerging as a hybrid imaging modality that combines optical excitation and ultrasonic detection. When photons are absorbed by an agent, the optical energy is partially or completely converted into heat through non-radiative decay. The local heat induces thermal expansion, and the thermal expansion generates a pressure wave which propagates as an ultrasound wave and can be detected by an ultrasound transducer to form a high-resolution tomographic image of optical absorption. (**Figure 1.1**). [6-9] Theoretically, the initial PA signal amplitude is described by:

$$P = \xi \Gamma \mu_a F$$

where ξ is a constant related to the imaging system, Γ is the Gruneisen parameter, μ_a is the absorption coefficient of an agent, and F is the local light fluence. In order to optimize PA signal amplitudes, efforts have been made to enhance the absorption coefficient of agents by material engineering and to maximize the local light fluence by shifting the imaging wavelength to "transparent" biological windows.

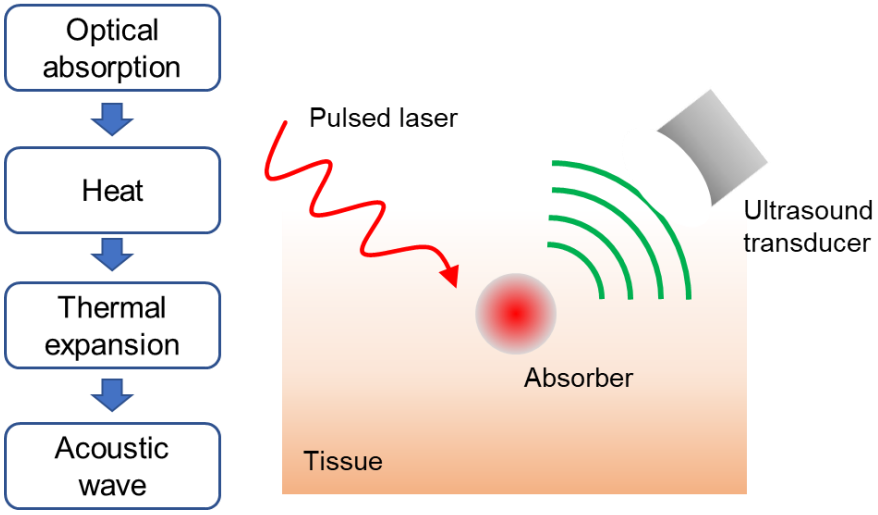

Figure 1.1 Principle of PA imaging.

1.3.2 The Fundamentals and Advantages of PA Imaging

Fortunately, the combination of optical excitation and ultrasonic detection of PA imaging brings several advantages over the conventional imaging modalities.

I. PA imaging uses nonionizing radiation, so it circumvents the radiation risk for patients.

II. PA imaging provides higher temporal resolution to realize real-time imaging, and it is also less expensive.

III. PA imaging has the advantage in providing chemical sensitivity, instead of mechanical contrast.

IV. The endogenous/exogenous agent in tissue is irradiated usually by a nanosecond-pulsed laser beam, and the temporally confined optical absorption engenders transient local temperature rise;[8] Therefore, photoacoustic imaging can provide a high signal-to-noise ratio without thermally damaging the tissue and can be repeatedly used in vivo by keeping the excitation energy below the ANSI safety limit.[8, 9]

V. Both diffused and ballistic photons contribute to the PA response, thus it breaks the penetration limits of traditional optical imaging modalities which only based on the ballistic and quasi-ballistic photons (**Figure 1.2**).[6, 7]

VI. The acoustic scattering in tissue is about three orders of magnitude less than optical scattering in tissue per unit path length.[8] Together with the abovementioned advantages, PA imaging offers greatly enhanced penetration depth in tissue with a scalable spatial resolution than optical imaging modalities do. Particularly, the penetration depth of PA imaging has reached ~4 cm *in vivo*[10] and ~12 cm *in vitro*[11] so far. This is unlikely to be achieved with optical imaging modalities, because the penetration of ballistic photon and quasi-ballistic photon is limited to ~100 μm and ~1mm;[6]

VII. According to the equation (1), PA signal is proportional to the optical absorption coefficient, which means it has 100% sensitivity to optical absorption.[6] In comparison, confocal microscopy or optical coherent tomography is two orders of magnitude less sensitive to optical absorption.[6]

VIII. The time-resolved acoustic detection effectively suppresses the interference of the surface signal and provides tomographic views.[7]

IX. PA imaging is free of the autofluorescence background in tissue as fluorescence imaging does.

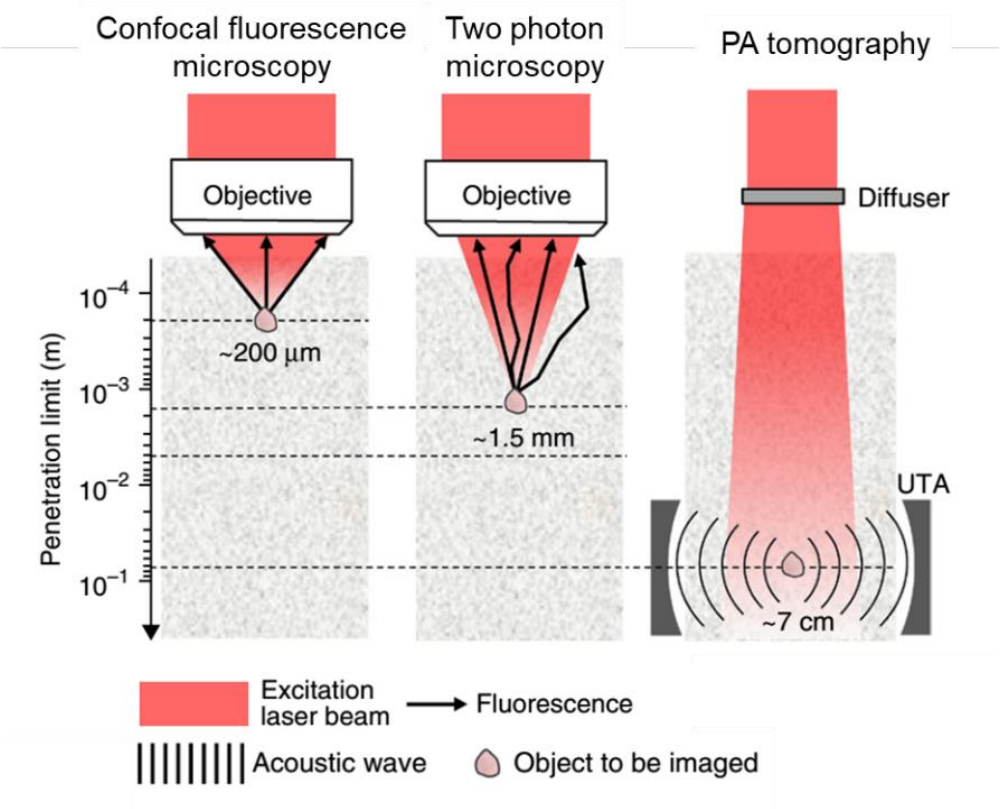

Figure 1.2 Signal generation and detection in confocal microscopy, two-photon microscopy and PA tomography, with different penetration limits in scattering tissue. The colors shown for the excitation light do not represent the true optical wavelengths. Reproduced with permission from Ref. [7]. Copyright © 2016, Springer Nature.

1.4 The Second Near-Infrared (NIR-II) Window

The NIR-II optical window (1000-1700 nm) is attracting substantial attentions, since the first NIR-II paper published in 2009 by Hongjie Dai group.[12] The advantages of NIR-II window over the NIR-I/visible window are: (I) absorption of hemoglobin is minimized, especially in the region beyond 1100 nm (**Figure 1.3a**);[13-15] (II) Less light scattering at longer wavelength, as the scattering is inversely proportional to wavelengths (λ^{-a}), in which the exponent (a) varies from 0.22 to 0.68 for different tissues (**Figure 1.3b**);[16-18] (III) higher maximum permissible exposure (MPE) of laser light according to ANSI standard (e.g. 30 mJ/cm^2 at 800 nm, 100 mJ/cm^2 at 1064

nm), so more energy can be deposited on tissue to achieve higher penetration depth (**Figure 1.3c**);[9] (IV) minimal autofluorescence, so background signal in fluorescence imaging is reduced (**Figure 1.3d**).[18, 19] Therefore, imaging in the NIR-II window can provide enhanced imaging depth, contrast and spatial resolution.[19]

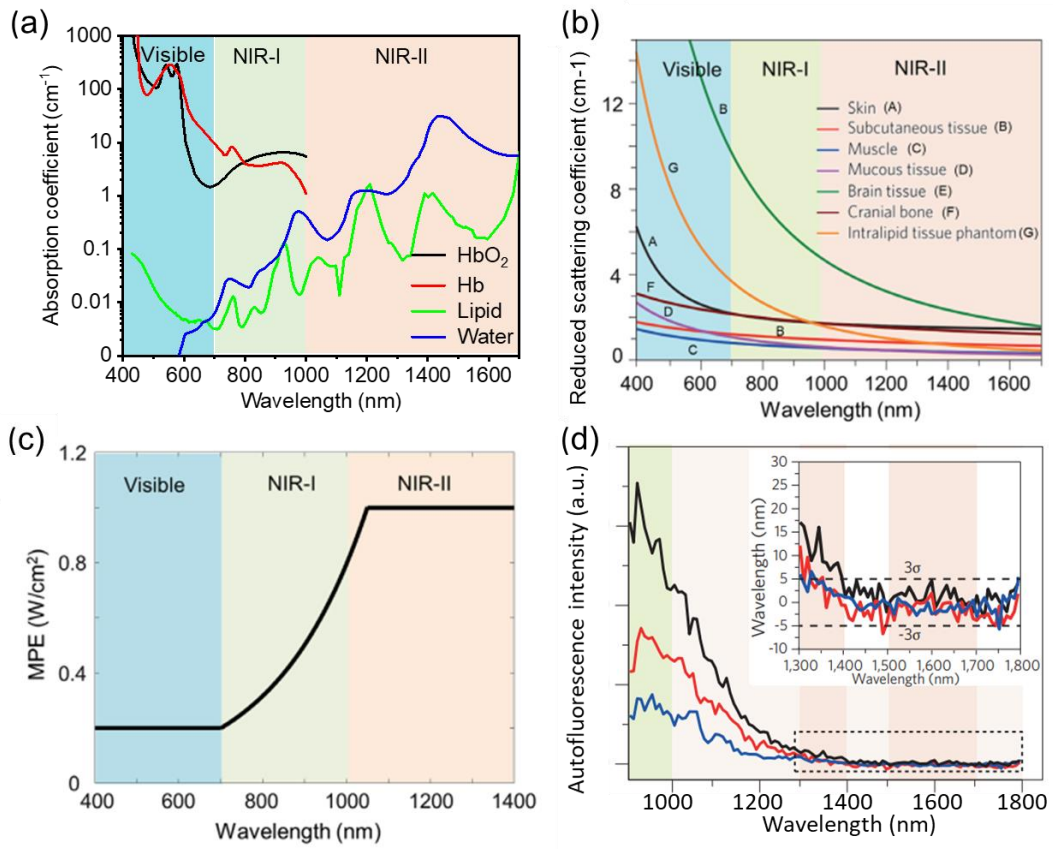

Figure 1.3 Motivation for NIR-II imaging. (a) Absorption spectra of the typical chromophores in tissue. Adapted from Ref. [13-15] (b) Reduced scattering coefficients in different types of tissues as a function of wavelength. Reproduced with permission from Ref. [18]. Copyright © 2017, Springer Nature. (c) MPE as a function of excitation wavelength. Reproduced with permission from Ref. [9] (d) Autofluorescence as a function of excitation wavelength. Reproduced with permission from Ref. [18]. Copyright © 2017, Springer Nature.

1.5 NIR-II PA Contrast Agents

1.5.1 Endogenous Contrast Agents

A variety of biological chromophores have been studied as endogenous contrast agents for PA imaging in disease detection, diagnosis and treatment-guidance.[20]

For example, the second and third overtone transition of C-H bond results in the absorption peak at ~1200 nm and ~1700 nm, respectively.[21, 22] Thus, researchers have conducted PA studies of lipid and fat at these two optical wavelengths in the NIR-II range. Accordingly, intravascular PA imaging was developed to visualize depth-resolved distribution of lipid contents in atherosclerotic plaques *in vivo* at ~1200 nm and ~1700 nm.[23-25] Meanwhile, intraoperative assessment of breast tumor margins was achieved by high-speed PA imaging of fat content in the adjacent normal tissue at ~1200 nm.[26, 27]

Due to the relatively strong absorption of hemoglobin at 1064 nm and the low background signal at this wavelength, PA imaging *in vivo* using blood contrast has been performed previously to visualize tumor angiogenesis[28] and inflammatory arthritis[29, 30]. In addition, whole-body 3-D PA imaging of small animals has also been achieved by imaging of body vasculature at 1064 nm.[31, 32]

Besides, melanin is another endogenous contrast agent in the NIR-II window, whose absorption is higher than that of hemoglobin at 1064 nm. Therefore, PA imaging with 1064 nm excitation has been utilized for detection of melanoma cells in blood circulation.[33, 34]

1.6 Exogenous Contrast Agents

PA imaging with endogenous contrast agents, which is a label-free and non-invasive method, can provide functional and even anatomical information.[35] However, they only offer access to a limited range of biological processes since their abundance is insufficient in many cases

and their photoacoustic efficiency is relatively poor, especially for deep tissue imaging. Meanwhile, endogenous contrast agents may have low specificity and sensitivity to diseases and the correlations vary from patient to patient.[20] On the other hand, exogenous contrast agents which are engineered to be highly efficient light absorbers and optoacoustic convertors can greatly enhance both the imaging depth and contrast of biological imaging. Furthermore, the functionalized contrast agents permit high-specificity and high-sensitivity imaging of the biological targets.[35]

Common PA exogeneous contrast agents include fluorescent proteins, small chromophores, carbon nanotubes, organic nanoparticles and plasmonic nanoparticles.[35-37] None of the fluorescent proteins can absorb in the NIR-II window and only a few small-molecule dyes can absorb NIR-II light but with poor photostability and aqueous solubility, so these two types of contrast agents have not been demonstrated for NIR-II PA imaging. On the other hand, carbon nanotubes exhibited a broad absorption spectrum and thus generated strong PA effective for cancer therapy and imaging under irradiation of 1064-nm pulsed laser.[38, 39] Meanwhile, phosphorus phthalocyanine also showed absorption around 1064 nm, and an imaging depth of up to ~12 cm has been achieved in chicken breast tissue.[11] In addition, quantum dots made of copper sulfide has been reported for *in vivo* lymph node imaging at 1064 nm. However, the cytotoxicity of the abovementioned contrast agents remains to be solved. Plasmonic nanoparticles, such as gold nanorods, nanoplates and nanoshells, have also been used for NIR-II PA imaging of liver and lymph nodes.[40, 41] Nevertheless, most of the NIR-II absorbing plasmonic nanoparticles were achieved either by high aspect ratios or by large dimensions with extremely thin shells, resulting in poor thermal stability, short blood circulation half-life, difficulty in extravasation and low tissue penetration rate.[42, 43]

1.7 Semiconducting Polymer for PA Imaging

Semiconducting polymer is an emerging new class of photoacoustic contrast agents. Semiconducting polymer were usually formed into water-soluble nanoparticles through nanoprecipitation method, and it has merits in controllable dimensions, outstanding photo- and aqueous stability, good biocompatibility, accessible functionality and high extinction coefficient.[44, 45] Although it has been widely used for PA imaging of tumors,[45] lymph nodes,[44] reactive oxygen species[46-48] and pH [49] in the NIR-I window, semiconducting polymer as NIR-II contrast agent has been rarely reported previously. Therefore, our work focuses on developing semiconducting polymer for photoacoustic imaging in the NIR-II window.

1.8 Development of NIR-II Semiconducting Polymer

1.8.1 Molecular Engineering

If a π-conjugated molecule is elongated from monomer to polymer, the bandgap will gradually be reduced, since the conjugation length is extended. As a result, the absorption wavelengths will be shifted to a longer wavelength in NIR-I window (**Figure 1.4a**).[44, 50-52] To further reduce the bandgap and fine-tune the absorption maxima to the NIR-II window, donor-accepter molecular engineering of conjugated polymer is the most widely used approach.[53-56] The incorporation of electron-rich donor and electron-deficient acceptor produces the quinoidal resonance in such polymer chains, which is beneficial for lowing bandgaps (**Figure 1.4b** and **Figure 1.5**).[54] Additionally, the high planarity and rigidity of the polymer background facilitate the intra/inter-molecular electronic interactions, which in turn contribute to large extinction coefficients and broad absorption spectra.[54, 57, 58] In summary, ultra-narrow bandgap of conjugated polymer can be achieved by strong donor-acceptor structures with highly flat and rigid backbones.[54, 57-59]

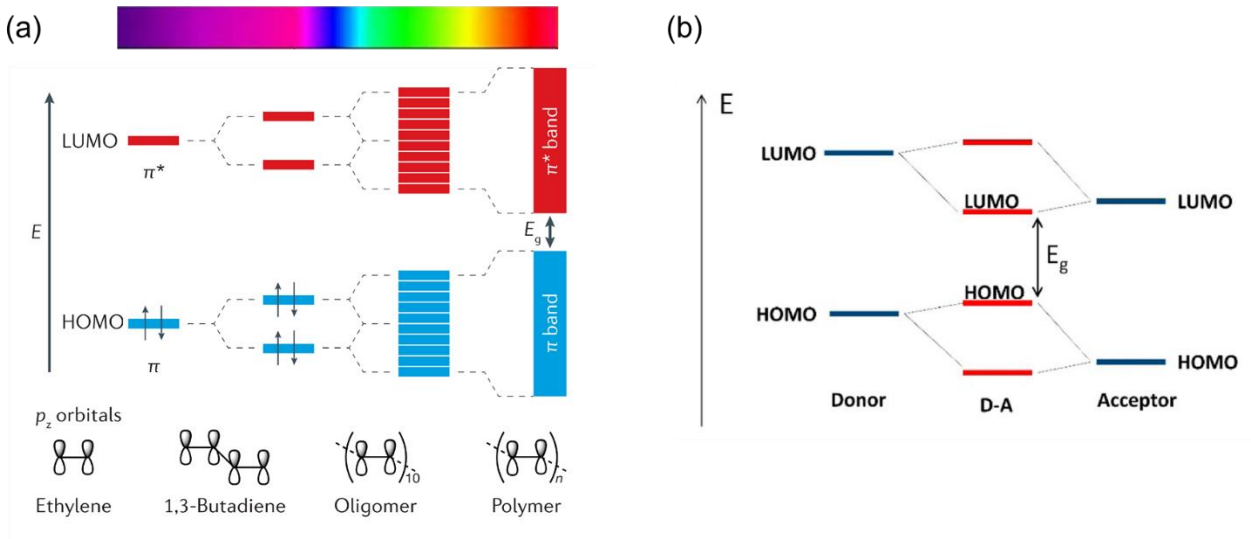

Figure 1.4 Molecular orbital theory explanation for bandgap reduction. (a) Polymerization of conjugated monomers into polymer. Reproduced with permission from Ref. [52]. Copyright © 2017, Springer Nature. (b) Donor(D)-accepter(A) molecular engineering. Reproduced with permission from Ref. [56]. Copyright © 2015, American Chemical Society. Eg: bandgap; HOMO: highest occupied molecular orbital; LUMO: lowest unoccupied molecular orbital.

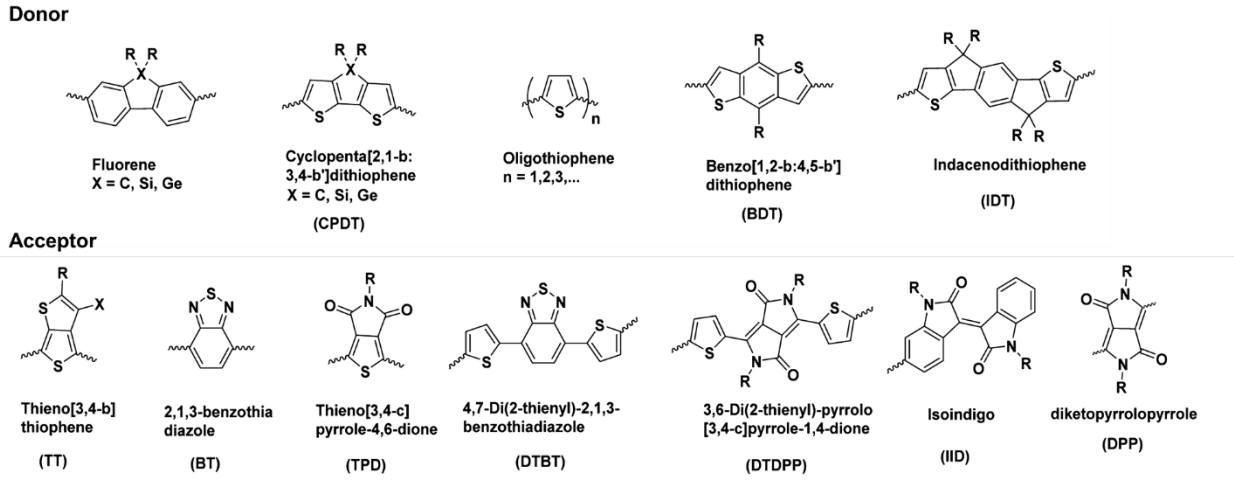

Figure 1.5 Typical donor (upper row) and acceptor (lower row) units. Reproduced with permission from Ref. [56]. Copyright © 2015, American Chemical Society.

1.8.2 Doping

Chemical/electrochemical doping is another feasible way to tune the bandgap of semiconducting polymer. In the doping process, electrons on conjugated π bonds are removed or added to form a polymeric ion, while the δ bonds are not much disrupted.[60] Thus, the doping process can be analogized to a redox reaction that an insulting neutral polymer is oxidized (or reduced) into a conducting/semiconducting polymeric cation(or anion).[60] Specifically, in the chemical p-type doping, the conjugated polymer is oxidized and gives electron to the oxidants, while in the chemical n-type doping, the conjugated polymer is reduced and gains electron from the reductants. Meanwhile, doping can also be realized by electrochemical oxidation or reduction of the conjugated polymers on an electrode. In the electrochemical p-type doping, the conjugated polymer is forced to lose an electron (be oxidized) accompanying the doping of counteranions from electrolyte solution, while in the electrochemical n-type doping, the conjugated polymer is forced to gain an electron (be reduced) accompanying the doping of countercations from electrolyte solution.[61]

Doping of conjugated polymer leads to the formation of new electronic states, which causes the red shift of absorption maxima (**Figure 1.6**).[60, 62]

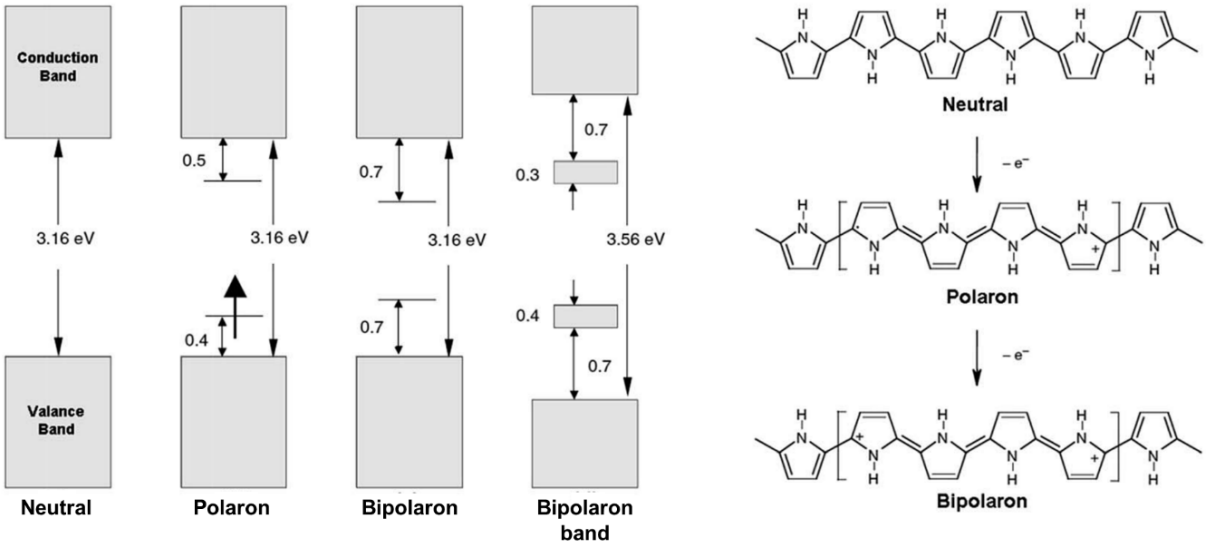

Figure 1.6 Electronic energy diagrams and structures for neutral, polaron, bipolaron, and fully doped bipolaron polypyrrole (p-type doping). Reproduced with permission from Ref. [62]. Copyright © 2014 The Royal Society of Chemistry

CHAPTER 2. CENTIMETERS-DEEP PHOTOACOUSTIC IMAGING IN THE NIR-II WINDOW BY USING SEMICONDUCTING POLYMER NANOPARTICLES

The work presented in this chapter was published in *Advanced Materials* Ref. [63]. Reprinted with permission from Ref. [63]. Copyright © 2017 WILEY-VCH Verlag GmbH & Co. KGaA, Weinheim

Thienoisoindigo-based semiconducting polymer with a strong near-infrared absorbance is synthesized and its water-dispersed nanoparticles (TSPNs) are investigated as a contrast agent for photoacoustic (PA) imaging in the second near-infrared (NIR-II) window (1000–1350 nm). The TSPNs generate a strong PA signal in the NIR-II optical window, where background signals from endogenous contrast agents, including blood and lipid, are at the local minima. By embedding a TSPN-containing tube in chicken-breast tissue, an imaging depth of more than 5 cm at 1064 nm excitation is achieved with a contrast-agent concentration as low as 40 μg mL^{-1}. The TSPNs under the skin or in the tumor are clearly visualized at 1100 and 1300 nm, with negligible interference from the tissue background. TSPN as a PA contrast in the NIR-II window opens new opportunities for biomedical imaging of deep tissues with improved contrast.

2.1 Introduction

Non-invasive imaging of targets in centimeter-deep tissues is important for preclinical and clinical studies of physiological and pathogenic processes, which could make diagnosis and/or treatments more effective and efficient.[8, 64-66] Among the various modalities for deep-tissue imaging, photoacoustic (PA) imaging is an emerging hybrid approach, which combines optical excitation and ultrasonic detection. Compared to traditional optical techniques, PA imaging provides a deeper penetration and higher spatial resolution, while maintaining rich contrast and

high sensitivity.[67-69] Although the penetration depth in PA imaging is significantly improved due to the low acoustic scattering in biological tissue (three orders of magnitude less than optical scattering) and high optical absorption sensitivity (two orders of magnitude greater than those of confocal microscopy and optical coherence tomography),[8] it is still limited by the attenuation of excitation light on account of optical absorption and scattering.[7] In addition, the optical absorption of blood and other biological compounds from tissue reduces the imaging contrast and sensitivity. To address these challenges, efforts have been devoted to developing exogenous contrast agents with absorption in the NIR-II window (1000 ~ 1350 nm),[11, 16, 39, 70-73] where light scattering is decreased and absorption of blood and other biological compounds is minimized.[19, 74]

Semiconducting polymer nanoparticles (SPNs) represent a new class of PA contrast agents with good biocompatibility as organic compounds,[75] excellent photostability, high mass extinction, and controllable dimensions.[46] SPNs have been used for *in vivo* PA imaging of tumors,[45] reactive oxygen species[46-48] and pH [49] in the first NIR window (700 ~ 1000 nm).[76] Thus far, SPNs for PA imaging in the NIR-II region have been seldom reported.[77] Here, we report a completely new SPN system, thienoisoindigo (TII) based semiconducting polymer nanoparticles (TSPNs), with strong absorption in 1000 ~ 1350 nm for PA imaging in the NIR-II window. TII, an electron-deficient unit with a high planarity, was previously developed for applications in organic electronics.[78] TII homopolymers have displayed an ultra-narrow bandgap with strong absorption in the NIR-II window.[79, 80] We designed and synthesized a new TII-based semiconducting polymer with triethylene glycol (TEG) side-chains for improving biocompatibility, and then formulated into TSPNs through nanoprecipitation. Next, we characterized the PA

properties of TSPN *in vitro*, and measured the penetration depth in chicken breast. Last, we demonstrated the potential of TSPN for skin and tumor imaging *in vivo*.

2.2 Results and Discussion

2.2.1 Design and Synthesis of TSPN with NIR-II Absorption

The synthesis of our TII-based semiconducting polymer, TII-TEG, is shown in **Figure 2.1a**. The formed highly planar backbone contributes to a long absorption wavelength in the NIR-II region.[79] Additionally, to further enhance the biocompatibility of the exogenous contrast agent, TEG-side chains were attached to the polymer backbones.[81] Stable TII-based semiconducting polymer nanoparticles (TSPNs) (**Figure 2.1b**) in aqueous solutions were formulated through the nanoprecipitation method, where a THF solution containing the polymer and DSPE-PEG2000 was quickly injected into water under sonication. THF was then removed by the nitrogen bubbling method. The resulted TSPNs exhibited broad absorption that covers both NIR-I and NIR-II regions (**Figure 2.1c**). The convex in the absorption spectrum of the TSPN aqueous solution resulted from the absorption saturation of water. In particular, its corresponding mass extinction coefficient in water at 1200 nm was 35±5 $mL \cdot mg^{-1} \cdot cm^{-1}$, which is comparable to that of NIR dyes (indocyanine green) at 800 nm (126.6 $mL \cdot mg^{-1} \cdot cm^{-1}$ (98148 $M^{-1} \cdot cm^{-1}$), with concentration of 7.75 $\mu g \cdot mL^{-1}$ (9.01 mM)),[82] as well as that of diketopyrrolopyrrole-based SPNs at 748 nm (76 $mL \cdot mg^{-1} \cdot cm^{-1}$).[45]

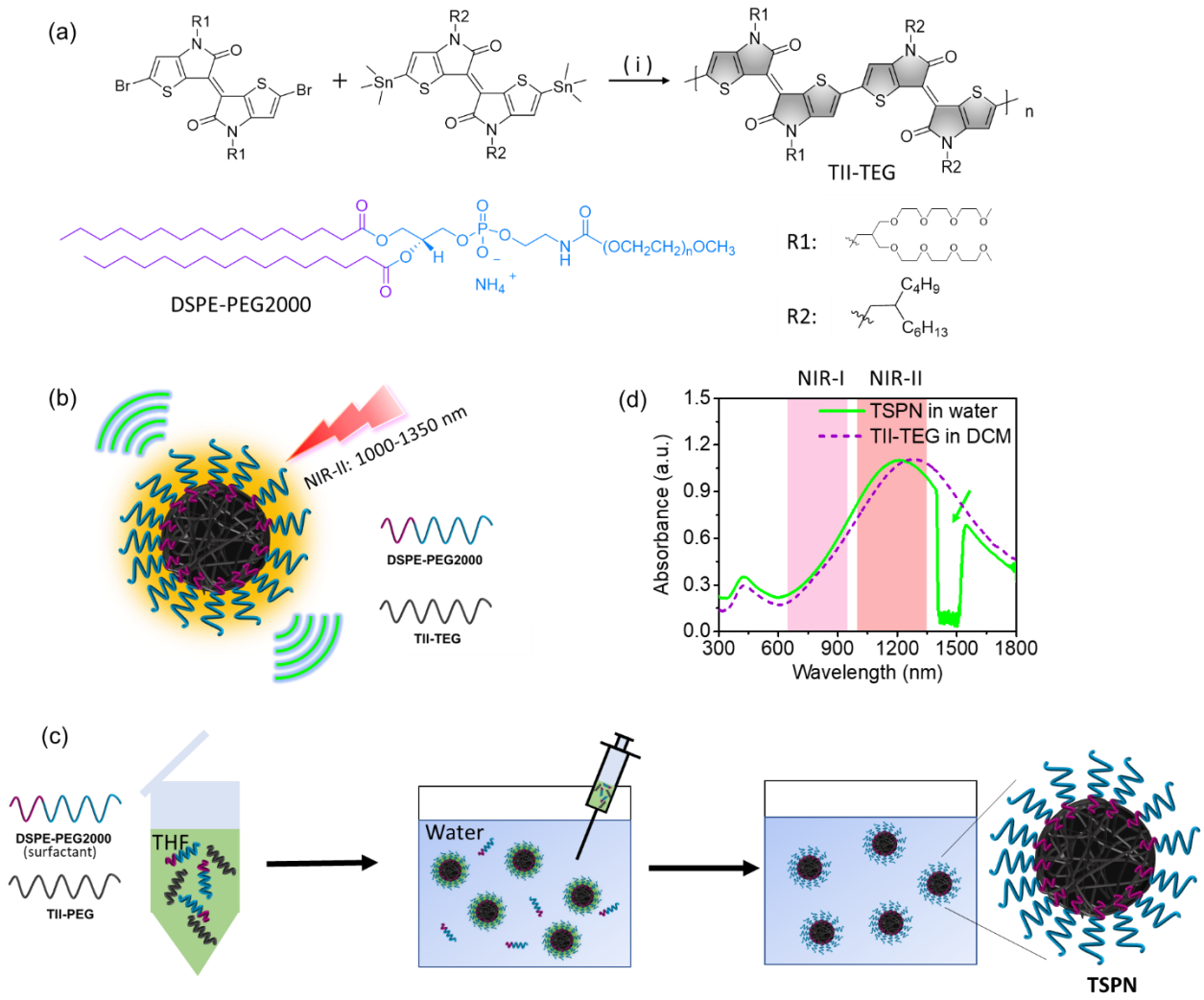

Figure 2.1 Design and Synthesis of TSPN with NIR-II Absorption. (a) Synthetic route of TII-TEG. (i) $P(o\text{-}toly)_3$, $Pd_2(dba)_3$, Toluene, 110 °C. Chemical structure of DSPE-PEG2000. (b) Schematic illustration of TSPN prepared by nanoprecipitation. (c) The illustration of nano-precipitation method for synthesis of TSPN. (d) Absorption spectra of TSPN in water (solid green line) and TII-TEG in dichloromethane (DCM) (dashed purple line). The convex in the curve of the aqueous solution resulted from the absorption saturation of water.

2.2.2 Aqueous Stability and Cytotoxicity of TSPN

The number-averaged size of TSPNs in an aqueous solution was characterized via dynamic light scattering (DLS) and was estimated to be 86 ± 11 nm (**Figure 2.2a**), which is within the desirable size range of enhanced permeability and retention effect for passive targeted drug delivery in the next stage.[83, 84] No change in size was observed after 50 days, indicating the

excellent aqueous stability. The spherical structure of TSPNs was further confirmed by transmission electron microscopy (**Figure 2.2b**). To investigate the biocompatibility of TSPN, we carried out cytotoxicity tests using various human cell lines (**Figure 2.2c**). No overt toxicity was found after incubation with TSPNs at concentrations up to 40 μg·mL^{-1}. Thus, the 40 μg·mL^{-1} concentration was used in the following experiments.

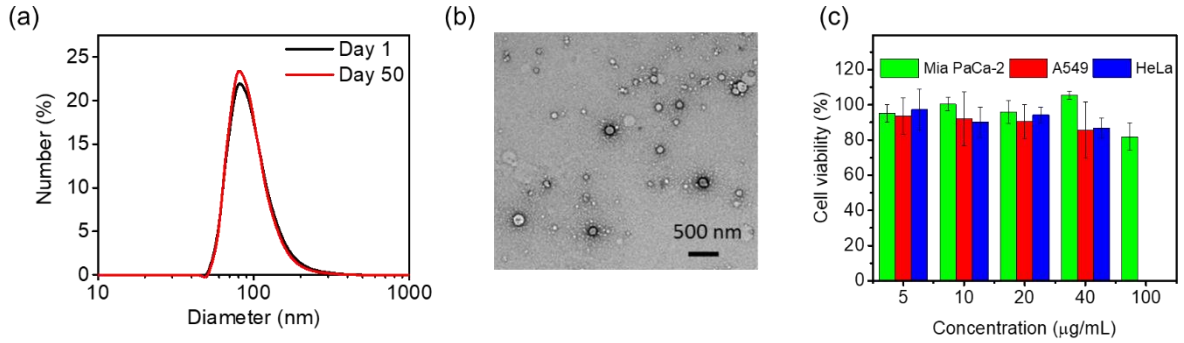

Figure 2.2 Aqueous Stability and Cytotoxicity of TSPN (a) Representative DLS profiles on the first day when the TSPN solution was freshly prepared (black line) and on the fiftieth day (red line). (b) TEM images of TSPNs with negative. (c) Cytotoxicity studies of TSPN. In vitro viability of Mia PaCa-2, A549 and HeLa cells were treated with TSPN solutions at concentrations of 5, 10, 20, 40 μg/mL for 24 h, respectively. The percentage cell viability of treated cells is calculated relative to that of cells treated with the same volume of PBS (viability was arbitrarily defined as 100%). Error bars represent standard deviations of four separate measurements.

2.2.3 Photoacoustic Signal of TSPN Compared to Biological Chromophores

As shown in **Figure 2.3a** and **2.3b**, TSPN generated a strong PA signal over the entire NIR-II region, which is consistent with its absorption spectrum. For comparison of TSPN with the major endogenous contrast agents, the PA spectra of pure olive oil (a representative of lipid), water, and hemoglobin (Hb, 150 mg·mL^{-1} [15]) were obtained. The PA signal of olive oil was dominant at 1210 nm with two local minima at ~1100 nm and ~1300 nm. The PA signal intensity of Hb was relatively large at 1000 nm but continuously decreased at longer wavelengths. On the contrary, the PA signal intensity of water gradually increased after 1100 nm, and became remarkable at ~1400

nm. Overall, the background signals from Hb, olive oil and water reached minima at ~1100 nm and ~1300 nm. Thus, by using TSPN with high PA intensity in the entire NIR-II region, the optimal contrast could be achieved at 1100 nm and 1300 nm. It is worth noting that the PA intensity of Hb was ~3.8 times lower at 1300 nm than that at 1100 nm. Therefore, PA imaging at 1300 nm is expected to provide excellent contrast in blood-rich tissues such as liver, kidney, lungs, heart, and spleen.

To further validate the spectroscopy data, we performed PA tomography imaging of above-mentioned compounds. Three transparent plastic (polyurethane) tubes containing TSPN solution, blood and olive oil were implanted in an agar gel. In **Figure 2.3c**, the blood was clearly visualized at 1000 nm, but became much less visible at 1100 nm and almost invisible at 1300 nm. For olive oil, the contrast was only apparent at 1200 nm. On the other hand, TSPN maintained a high brightness from 1000 nm to 1300 nm. The intensity values for each tube from the images were extracted for quantitative comparison, and the derived curves (wavelength vs. PA intensities) are consistent with the PA spectra results (**Figure 2.3d**).

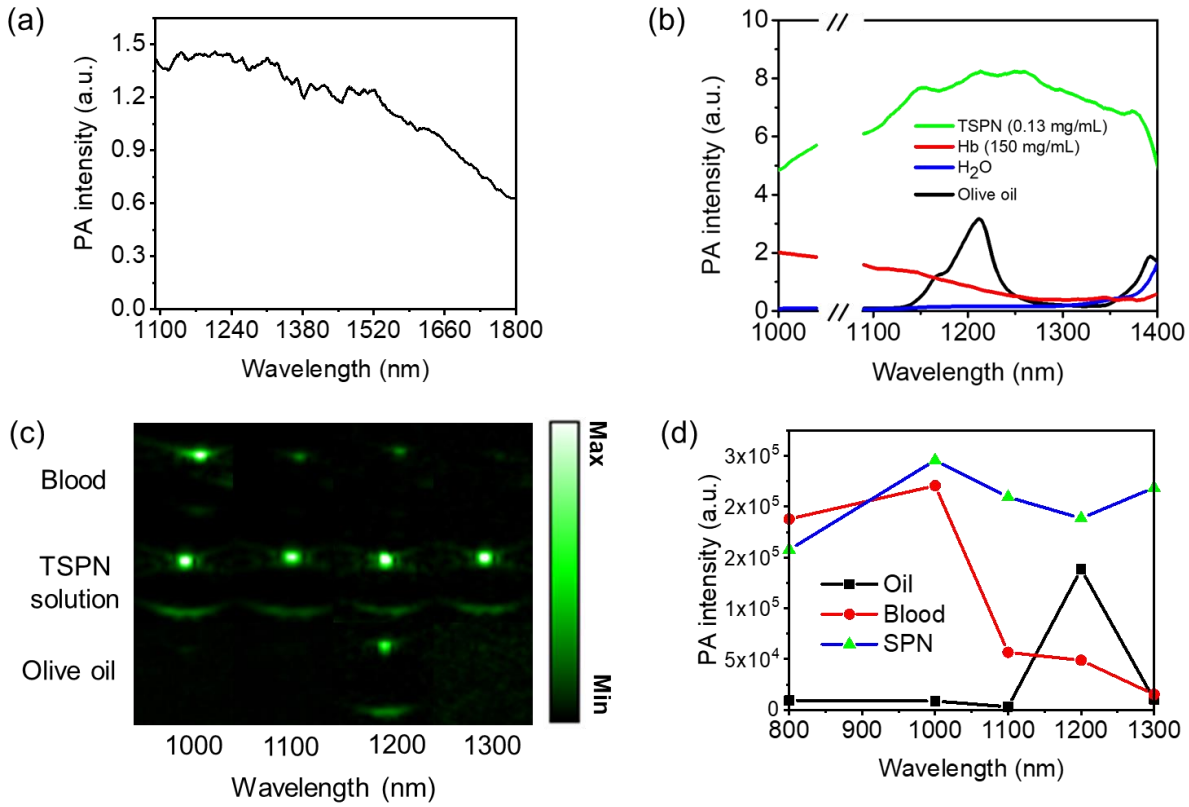

Figure 2.3 Photoacoustic Signal of TSPN Compared to Biological Chromophores. (a) PA spectrum of TSPN in D_2O with a concentration of ~2.5 μg·mL^{-1}. Laser energy, 45 μJ. (b) PA spectra of water, 150 mg·mL^{-1} hemoglobin (Hb), lipid (represented by olive oil), and 40 μg·mL^{-1} TSPN. The spectra of TSPN and Hb were obtained by subtraction of water from the spectra of TSPN and Hb aqueous solutions, respectively. (c) PA images of blood, 40 μg·mL^{-1} TSPNs, and lipid (represented by olive oil) contained in transparent plastic tubes with a laser wavelength at 1000, 1100, 1200 and 1300 nm, respectively. (d) PA intensities extracted from PA images (c) of blood, 40 μg·mL^{-1} TSPN, and lipid (represented by olive oil) contained in transparent plastic tubes with a laser wavelength at 1000, 1100, 1200 and 1300 nm, respectively. The averaged laser energy density was approximately 10 mJ·cm^{-2} at 800 nm, 9 mJ·cm^{-2} at 1000 nm, 18 mJ·cm^{-2} at 1100 nm, 5 mJ·cm^{-2} at 1200 nm and 4 mJ·cm^{-2} at 1300 nm. Each image was normalized with the corresponding laser energy density.

2.2.4 Photostability and Detection Sensitivity of TSPN

Next, the photoacoustic signal properties of TSPN were characterized. In the PA microscope spectroscopy, the PA signal intensity at NIR-II wavelengths remained stable over excitation by 12000 pulses at the energy level of ~45 μJ (~1 J·cm^{-2} at the focus), showing good photostability of TSPNs (**Figure 2.4a-c**). The PA intensities of TSPNs at 1200 nm were

determined at different concentrations, displaying a linear relationship between PA signal intensity and concentration (**Figure 2.4d**). Under the same experimental condition, the detection sensitivity, defined as 1:1 signal to background ratio, was estimated to be ~3 μg·mL^{-1}. All signal intensities were normalized with the excitation laser energy density at different wavelengths unless otherwise mentioned, mainly because the optical attenuation in the acoustic coupling media at each wavelength is different. Notably, the absorption coefficient of water, the major absorber in acoustic coupling media, is one-order of magnitude lower at 1100 nm than that at 1200 nm or 1300 nm.[14] This presents one of the advantages of using 1100 nm instead of 1300 nm for excitation.

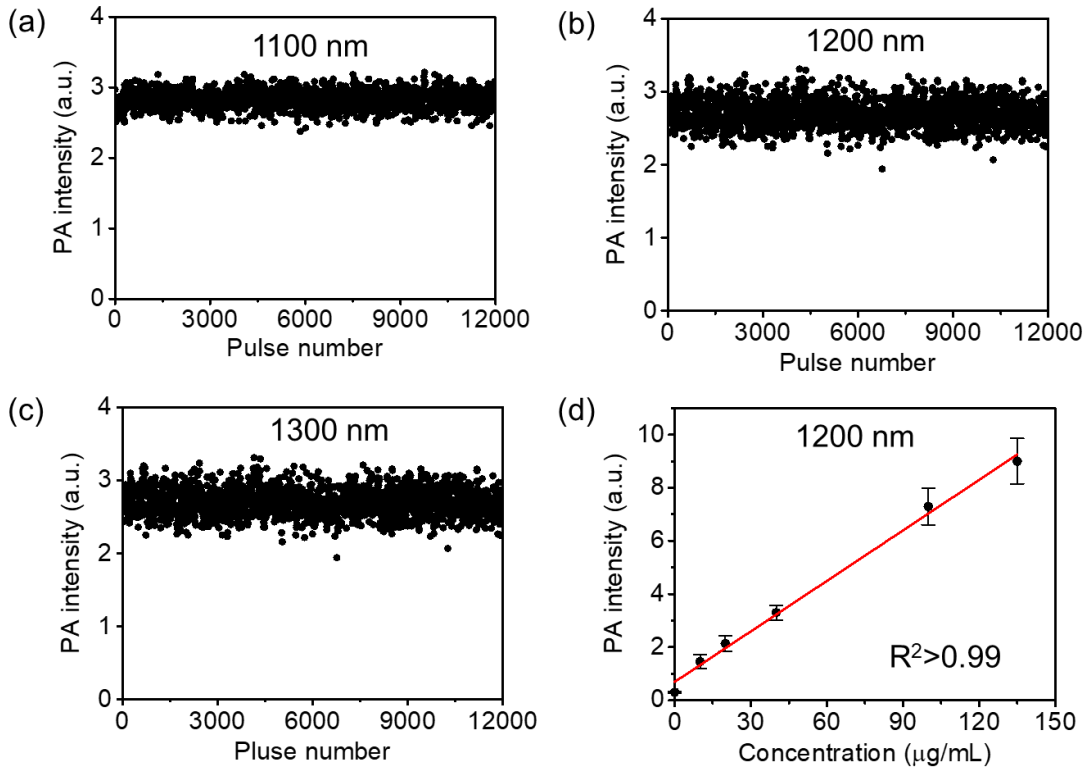

Figure 2.4 Photostability and Detection Sensitivity of TSPN. PA amplitude of 40 μg·mL^{-1} SPN over 12000 pulses with a laser wavelength at (a) 1100 nm (b) 1200 nm (c) 1300 nm. The total time is 55 minutes for repeat sweeping wavelength from 1100-1350 nm for 2000 times. The laser light energy at the focus point is ~45 μJ. (d) PA intensity of TSPN at 1200 nm as a function of mass concentration. R^2>0.99. Error bars represent for standard deviations.

2.2.5 Centimeter-Deep Imaging Depth in Chicken Breast Tissue

To explore the potential of TSPN for the deep-tissue imaging, we assessed the PA tomography imaging depth at 1064 nm using chicken breast tissue as a scattering medium. A transmission-mode detection was adopted in this experiment. To be analogous to a reflection-mode, we placed the same thicknesses of chicken breast tissues below and above a transparent plastic tube filled with TSPN solution, so that the excitation light and ultrasound traveled the same distance within the tissue (**Figure 2.5a**). The PA images at different depths were collected by changing the number of layers of chicken breast tissues below and above the tube simultaneously. The corresponding laser energy density was ~55 $mJ \cdot cm^{-2}$ and 100 images were acquired and averaged at the same position. The signal-to-noise ratio (SNR) of PA signal was plotted as a function of depth and was fitted into an exponential function based on Lambert-Beer's law (**Figure 2.5b**).[85, 86] The optical effective attenuation coefficient (defined as the slope of the fitted curve) was calculated to be 1.34 cm^{-1}, corresponding to 0.746 cm optical penetration depth. Notably, the tube containing 40 $\mu g \cdot mL^{-1}$ TSPNs was clearly visualized up to 5 cm with a SNR of 82 (**Figure 2.5c**). As a result, the achieved imaging depth is 6.7 times larger than the optical penetration depth. Furthermore, the imaging-depth limit was calculated to be 6.05 cm by extending the fitting curve to where the SNR of TSPNs was equivalent to the SNR of tissue background (SNR = 20). Compared to NIR-II copper sulfide quantum dots[71], 2.5 times less mass concentration of TSPNs is required to reach the same imaging depth of 5 cm at 1064 nm, and with only half of the laser energy density. To the best of our knowledge, the current record of the PA imaging depth is 11.2 cm by using porphysomes,[11] but the mass concentration (~50000 $\mu g \cdot mL^{-1}$ or 30 mM) is ~1270 times higher than that of TSPNs in this work. These data collectively show that TSPN is a competitive NIR-II contrast agent for centimeters-deep PA imaging.

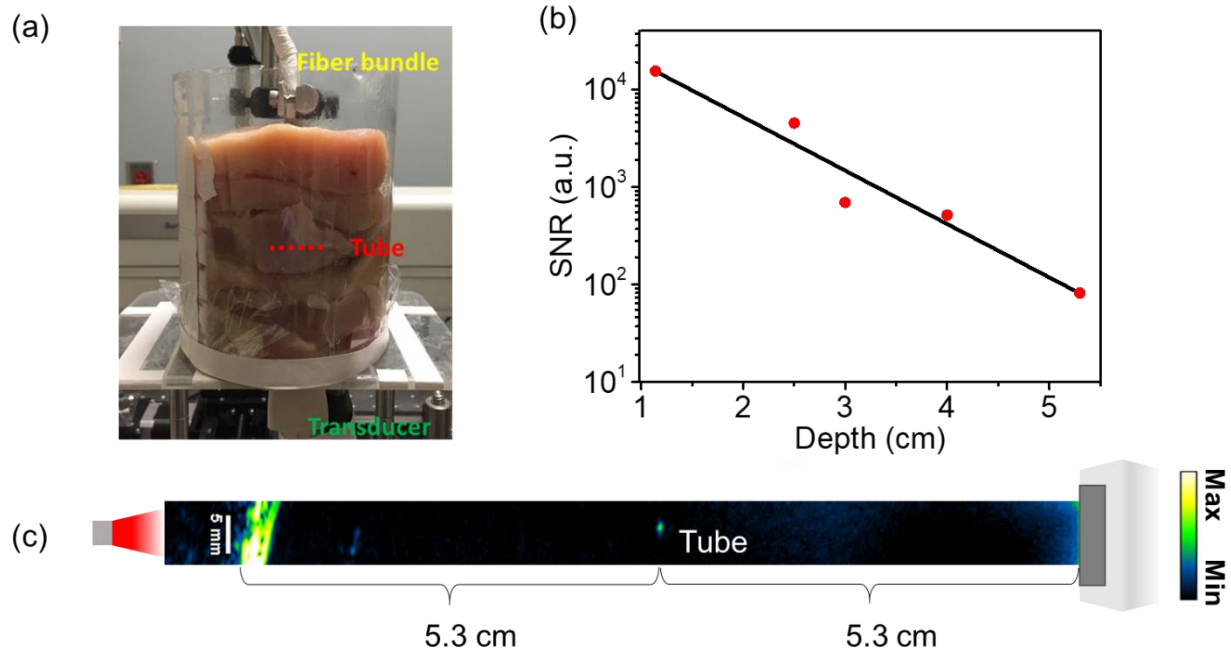

Figure 2.5 PA imaging of TSPN embedded in a chicken breast tissue. (a) Photograph of the experimental setup. The tube was placed in the middle of chicken breast tissue layers. (b) SNR of 40 μg·mL^{-1} TSPNs contained in a transparent plastic tube as a function of depth from illuminated tissue surface with a laser wavelength at 1064 nm (c) PA image of the 40 μg·mL^{-1} TSPNs in a transparent plastic tube at 5 cm depth. Laser energy density was tuned to 55 mJ·cm^{-2} at 1064 nm.

2.2.6 In Vivo PA Imaging of TSPN in the NIR-II Window

After characterizing the PA properties of TSPN *in vitro* in agar gels and *ex vivo* in chicken breast tissues, we further evaluated the performance of TSPN in living subjects by subcutaneous injection of matrigel-containing solutions of TSPNs (50 μL, 40 μg·mL^{-1}) into the dorsal area of rats. As shown in **Figure 2.6a**, for a skin tissue without injection, the lowest signal was observed at 1300 nm, possibly due to the least intrinsic blood absorption, and the signal at 1100 nm was comparably weak. In the meantime, stronger absorptions of blood at 800 nm and 1000 nm led to the higher PA signal intensities at these wavelengths. The strong signal at 1200 nm should be generated from the adipose fat in the skin layer, which matched the spectrum of lipid (Figure 2.3b). We found that the signal intensities increased by 7.3-fold at 1100 nm and 10.7-fold at 1300 nm with the injection of 50μL of 40 μg·mL^{-1} TSPNs (**Figure 2.6a** and **Figure 2.7a**), compared to the

signal found in the skin tissue without injection. This significant signal enhancement indicates the capability of TSPN as an exogenous contrast agent for *in vivo* imaging. In this study, a rat model was adopted, because rat skin has more structural similarities to human tissue than other rodents.[87, 88] Yet, the density of hair follicles in rat skin is different from human skin, which recalls future studies to better understand the performance of TSPN for PA imaging in human tissues.

We further evaluated the potential of TSPN for tumor imaging by *in vivo* PA tomography imaging of TSPNs directly injected into PC3-M xenografts in mice. Without administration of TSPNs, relatively strong PA signals were observed from the tumor tissue only at 800 nm and 1000 nm, which should be attributed to the rich blood vessels surrounding the tumor (**Figure 2.6b** and **Figure 2.7b**).[89-91] Similarly to our observation in skin, the signals at 1200 nm are more likely from adipose fats. Then, 50μL aqueous solution of 40 $\mu g \cdot mL^{-1}$ TSPNs was intratumorally injected into the tumor (**Figure 2.8**). With the administration of TSPN, strong PA signals generated within the tumor (dashed circles), with laser excitation wavelengths over 800 nm to 1300 nm, respectively. Compared to the images of the tumor without TSPN, the signal was enhanced ~7.0-fold at 1100 nm and ~13.3-fold at 1300 nm (Figure 2.6b and Figure 2.7b). The overlays between the skin and TSPNs signals might be resulted from the leaking of TSPNs after the injection. Because of the movement of the transducer during the injection of TSPNs, the images (with or without TSPNs) represented the transverse slices of the same tumor at different positions.

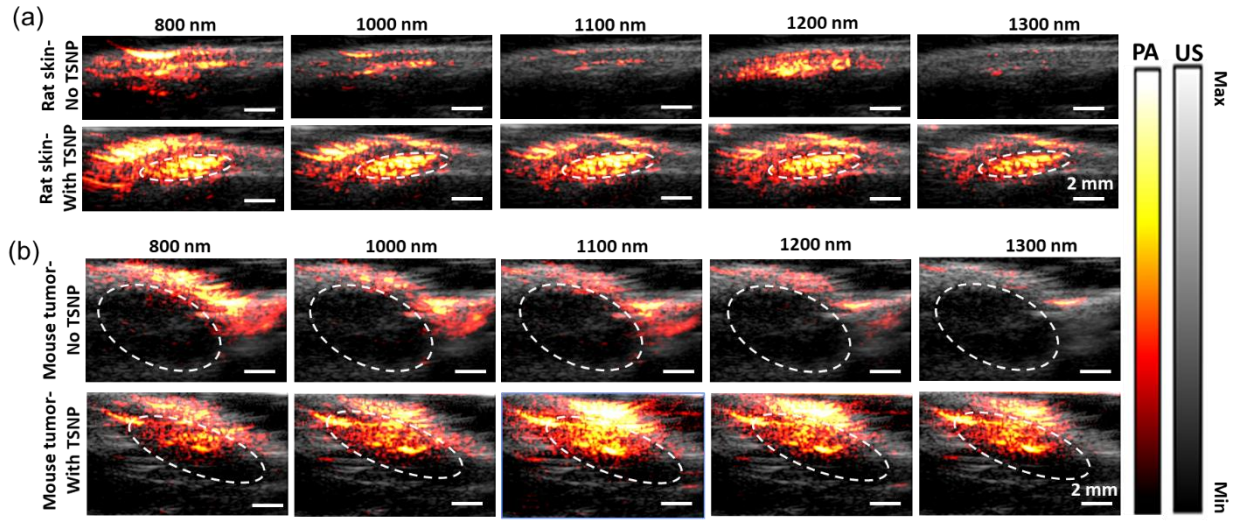

Figure 2.6 *In vivo* PA/US imaging of TSPNs. (a) Rat skin without injection of TSPNs (upper) and with injection of 50 μL, 40μg·mL^{-1} matrigel inclusions of TSPNs (dashed circles) (lower), and in (b) Mouse tumor (dashed circles) without injection of TSPNs (upper) and with injection of 50 μL, 40μg·mL^{-1} aqueous solution of TSPNs (lower). The averaged laser energy density was approximately 10-26 mJ·cm^{-2} at 800 nm, 19-49 mJ·cm^{-2} at 1000 nm, 33-40 mJ·cm^{-2} at 1100 nm, 37-46 mJ·cm^{-2} at 1200 nm and 25-35 mJ·cm^{-2} at 1300 nm. Each image was normalized with the corresponding laser energy density.

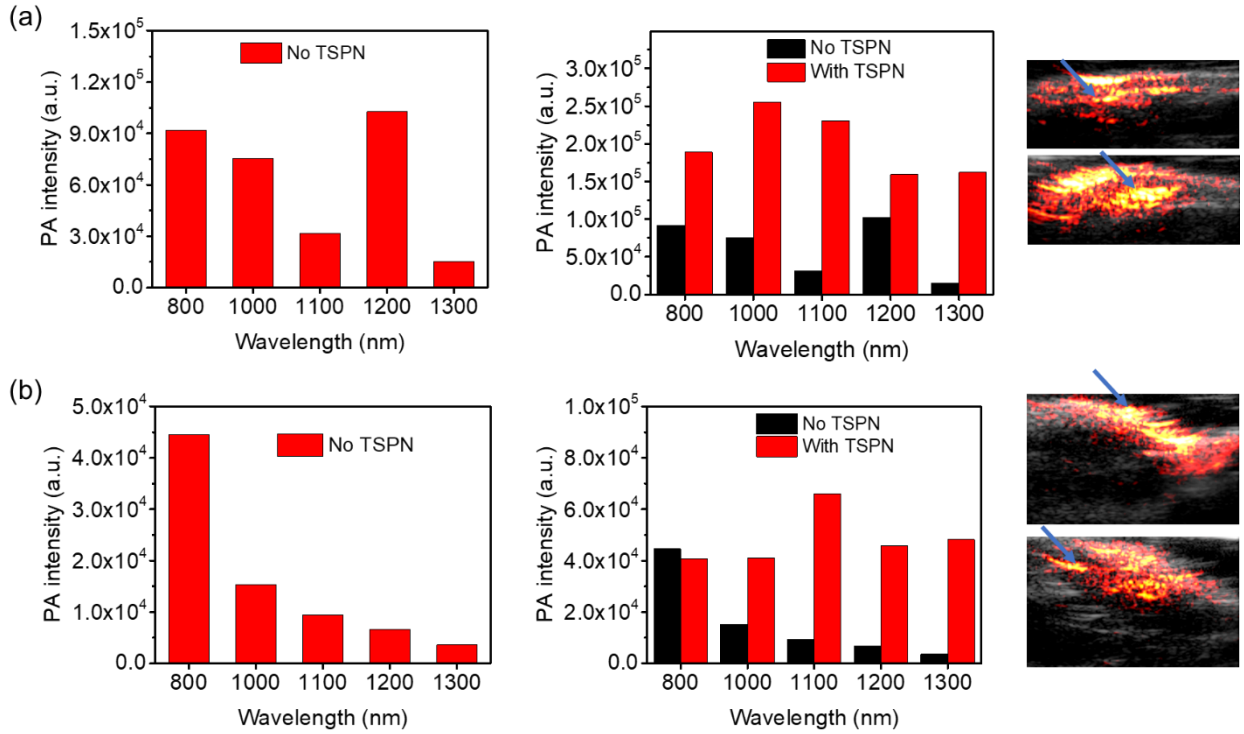

Figure 2.7 The PA intensities extracted from in Figure 2.6. (a) Rat skin without injection of TSPN (upper) and with injection of 50 μL, 40μg·mL^{-1} matrigel inclusions of TSPN (dashed circles) (lower), and in (b) Mouse tumor (dashed circles) without injection of TSPN (upper) and with injection of 50 μL, 40μg·mL^{-1} aqueous solution of TSPN (lower). The region of interest is indicated by an arrow.

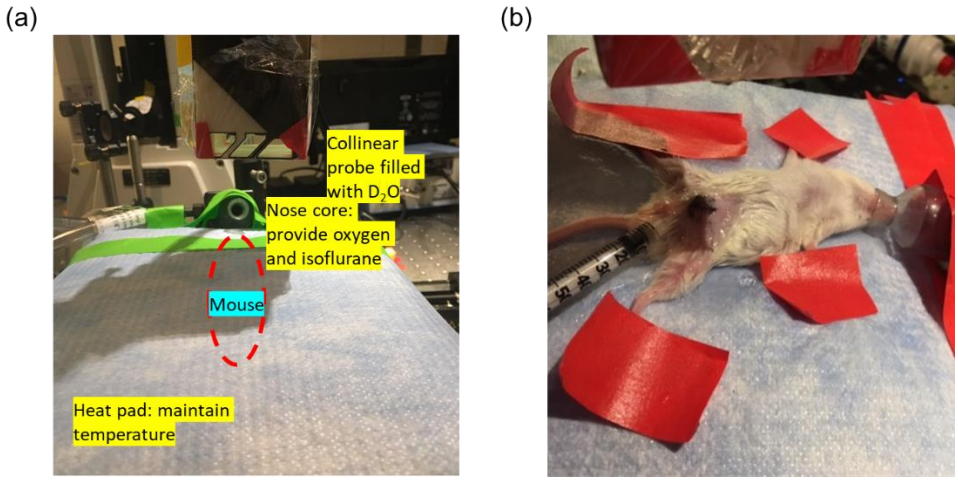

Figure 2.8 *In vivo* PA imaging setup. (a) Photograph of *in vivo* PA tomography imaging setup. (b) Photograph of the intratumoral injection.

Moreover, images of fixed mice prostate tumor xenografts before and after injections of TSPNs were recorded to confirm that the signal enhancements were indeed resulted from the introduction of TSPNs, and significant increases in signal were observed after the injections (**Figure 2.9**).

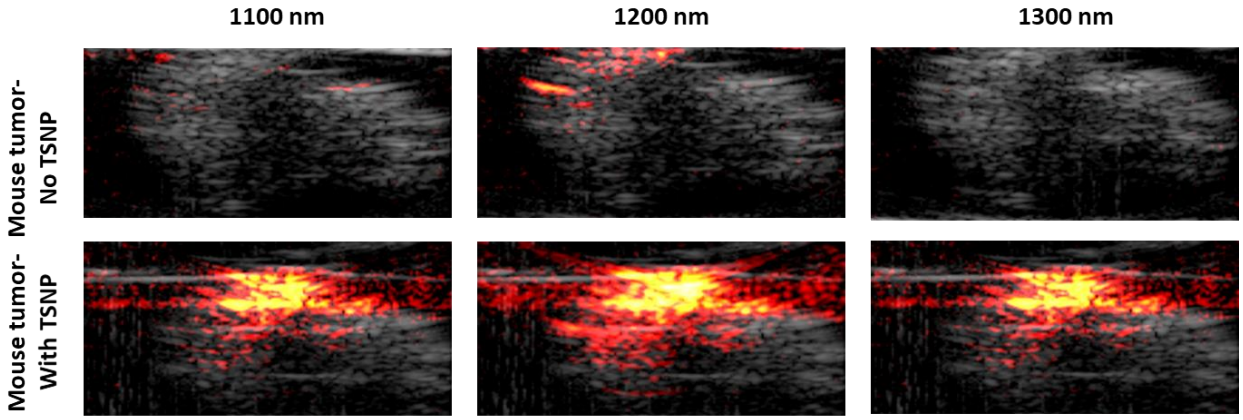

Figure 2.9 *Ex vivo* images of the mouse prostate tumor. (a) without injection of TSPN and (b) with injection of 40 μg·mL^{-1} TSPN. Laser energy density, 10 mJ·cm^{-2}.

2.3 Summary

TSPN as a PA contrast agent in NIR-II window was reported. The TSPN is suitable for biological imaging because of its good aqueous stability, nano-scale size, high photostability, and low cytotoxicity. The TSPNs generated a strong PA signal over the entire NIR-II region. The PA spectra and PA imaging in an agar gel phantom reveal that 1100 nm and 1300nm are theoretically two optimal wavelengths where the PA signals of two major endogenous contrast agents (lipid and blood) are in the local minima. PA imaging of TSPNs at 1300 nm further benefits from even less intrinsic blood signal from tissue background, while PA imaging at 1100 nm laser might provide higher laser energy on the tissue due to the less light attenuation in water. TSPNs at a comparably low concentration (40 μg·mL^{-1}) could be readily imaged through ~5 cm thick of chicken breast

tissues at 1064 nm laser excitation. The potential of TSPN for tumor imaging was demonstrated *via* intratumoral injection of TSPNs into tumor xenografts. Future functionalization of TSPN with targeting groups promises to establish the utility of TSPN in biomedical imaging.

2.4 Experimental Section

Chemicals and Polymer Synthesis: All reagents were purchased from Sigma-Aldrich and used without further purification unless otherwise noted. Anhydrous N, N-dimethylformamide is prepared from MB-SPS solvent purifying system. TII-TEG was synthesized via palladium-catalyzed C-C cross-coupling techniques and will be thoroughly purified to remove any metal residues.

Synthesis of TSPN: A standard protocol has been developed to prepare SPNs through the nanoprecipitation method. Briefly, a 1 mL THF mixture of SPs (1 $mg \cdot mL^{-1}$) and surfactant DSPE-PEG (2.50 $mg \cdot mL^{-1}$) was rapidly injected into deionized water (9 mL) under continuous sonication with a micro tip-equipped probe sonicator (Branson, W-150) at a power output of 6 watts RMS for 30 s. After sonication for additional 1 min, THF was evaporated at 45 ℃ under nitrogen atmosphere. The aqueous solution was filtered through a polyethersulfone (PES) syringe driven filter (0.45 μm) and centrifuged three times using a 30 K centrifugal filter unit at 3,000 rpm for 3 min at 4 ℃. The nanoparticle solution was stored in dark at 4 ℃.

Characterization: ^{1}H and ^{13}C NMR spectra were recorded on a Brucker ARX 400 at 293 K with deuterated chloroform as the solvent. Transmission electron microscopy (TEM) images were obtained on Tecnai T20. Dynamic light scattering (DLS) was performed using a Malvern Nano-zetasizer. UV/VIS/NIR spectra were recorded with Cary-6000.

Photoacoustic Spectroscopy: The complete description of the photoacoustic spectroscopy setup can be found in elsewhere.[92] The OPO Laser (EKSPLA NT320) with pulse width 5 ns,

repetition rate 10 Hz was applied as excitation laser resource. Nikon Eclipse TE2000-U inverted microscope with 10X objective was used to focus the light to the sample. The laser energy after ND filter was 40-120 μJ. Single element transducer (v317-sm, 20 MHz) was used to acquire acoustic and photoacoustic signals. A preamplifier (Olympus 5682, voltage gain 30 dB) and a Pulser/receiver (Olympus 5073 pr, ultrasonic bandwidth 75 MHz, voltage gain 39 dB) were used to improve the system sensitivity. All the samples were in the solution state and were sealed in 1 mm diameter glass tube. D_2O was applied as the sound coupling agent to avoid water absorption.

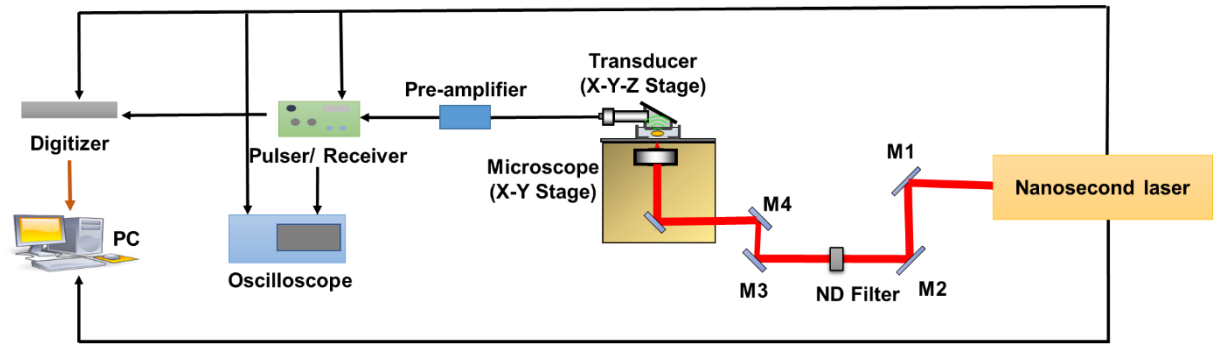

Figure 2.10 PA spectroscopy setup. M1, M2, M3, M4: mirrors.

Photoacoustic Tomography: The ultrasound and photoacoustic signals were processed by a high-frequency ultrasound imaging system (Vantage128, Verasonics Inc.). For the penetration study in chicken breast, a Q-switched Nd:YAG laser (Continuum Surelite SL III-10) with 5 ns pulse with a 10 Hz repetition rate was applied as the laser source. A transmission-mode detection modality was adopted. The laser light was guided to the tissue surface by a fiber bundle and the photoacoustic signals were detected from the other side of the tissue by a low-frequency transducer array (L7-4, PHILIPS / ATL). For the other photoacoustic tomography experiments, the EKSPLA OPO Laser with pulse width 5 ns, repetition rate 10 Hz was applied as excitation laser. In the meantime, a refection-mode detection was applied with using a customized collinear probe, which

has a customized high-frequency ultrasound array with 128 elements and 50% bandwidth (L22-14v, Verasonics Inc.).

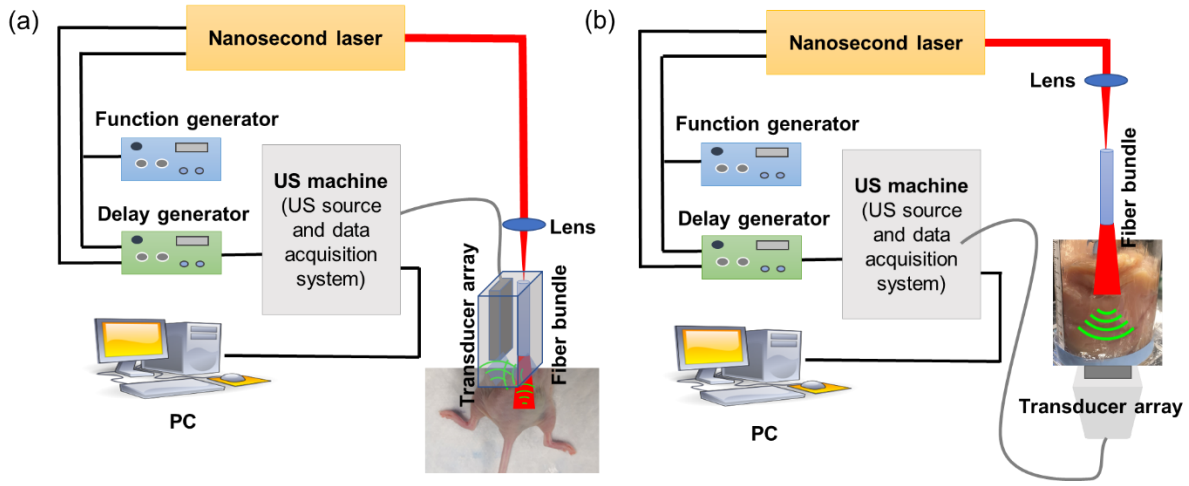

Figure 2.11 PA tomography setup with a (a) reflection-mode or (b) transmission-mode detection. *In vivo* PA imaging and *ex vivo* imaging of organs and tumors were carried out with a reflection-mode detection. Imaging depth evaluation in chicken-breast tissue was carried out with a transmission-mode detection.

Cytotoxicity Test: Cells were cultured in Dulbecco's Modified Eagle Medium (DMEM) containing 10% fetal bovine serum in a humid environment containing 5% CO_2 and 95% air at 37 ^{o}C. The *in vitro* toxicity of different types of human cell lines (A549, HeLa, and Mia PaCa-2) was studied. Cells were first seeded in 96-well plates (3000~5000 cells per well) for, and the culture medium was replaced with fresh medium containing polymer NP at different concentrations (0-100 μg·mL^{-1}) and incubated for 24 h. The cell viability was then measured by Cell Counting Kit-8 cytotoxicity array (Dojindo Molecular Technologies, Inc.).

Tumor mouse model: PC3-M cells were injected into the prostate of male 6-week-old NSG mice (Purdue University Center for Cancer Research) following the protocols reported previously[93, 94] were mixed with an equal volume of Matrigel and injected into the prostate gland

of the mouse. Tumors were grown for three weeks before used for PA tomography imaging. All animal procedures were approved by the Purdue Animal Care and Use Committee.

In vivo PA Tomography Imaging: All protocols for this experiment were approved by the Purdue Animal Care and Use Committee. NSG mice bearing PC3-M tumor xenografts and one-month-old healthy Sprague Dawley rats were anesthetized using 2% isoflurane in oxygen delivered through a nose cone. Prior to photoacoustic imaging, the areas of interest were shaved.

CHAPTER 3. TARGETED PHOTOACOUSTIC IMAGING OF PROSTATE CANCER IN THE NIR-II WINDOW BY USING FUNCTIONALIZED SEMICONDUCTING POLYMER NANOPARTICLES

The work presented in this chapter has been submitted to *Small*.

Development of molecular probes holds great promise for early diagnosis of aggressive prostate cancer. Here, 2-[3-(1,3-dicarboxypropyl) ureido] pentanedioic acid (DUPA)-conjugated ligand and bis-isoindigo-based polymer (BTII) are synthesized to formulate semiconducting polymer nanoparticles (BTII-DUPA SPN) as a prostate-specific membrane antigen (PSMA)-targeted probe for prostate cancer imaging in the NIR-II window. Insights into the interaction of the imaging probes with the biological targets from single cell to whole organ are obtained by transient absorption (TA) microscopy and photoacoustic (PA) tomography. TA microscopy reveals the targeting efficiency, kinetics, and specificity of BTII-DUPA SPN to PSMA-positive prostate cancer at single-cell level. At the organ level, PA tomographic imaging of BTII-DUPA SPN in the NIR-II window demonstrates superior imaging depth and contrast. By intravenous administration, BTII-DUPA SPN demonstrates selective accumulation and retention in the PSMA-positive tumor, allowing noninvasive PA detection of PSMA overexpressing prostate tumors *in vivo*. The distribution of nanoparticles inside the tumor tissue is further analyzed through TA microscopy. These results collectively demonstrate BTII-DUPA SPN as a promising targeted probe for prostate cancer diagnosis by PA tomography.

3.1 Introduction

Prostate cancer is the most common male malignancy and remains the second leading cause of cancer deaths in men in the United States.[95] Serum prostate specific antigen (PSA) test is a standard approach for prostate cancer screening.[96] However, common conditions, such as benign prostatic hyperplasia and prostatitis, are also accompanied by increased PSA levels, resulting in false-positive results and a large number of unnecessary prostate biopsies.[97, 98] Besides, the current standard transrectal ultrasound–guided prostate biopsy is like a "lottery" to patients, because biopsy needles are placed blindly into the prostate owing to the inability to visualize prostate cancer.[99, 100] As a result, indolent tumors with little clinical relevance are substantially overdiagnosed and overtreated, while some aggressive prostate cancer may be missed.[101, 102] The recent introduction of magnetic resonance imaging (MRI)-guided prostate biopsy allows improved accuracy but adds significant cost and lacks real-time imaging capabilities.[100, 103, 104] Thus, there is an urgent need to develop cost-effective diagnostic tools with high sensitivity and specificity for detection and staging of prostate cancer.

Photoacoustic (PA) tomography as a hybrid imaging modality with light excitation and acoustic detection is attractive for clinical applications. Compared to conventional imaging modalities, such as, MRI, computed tomography and positron emission tomography, PA tomography provides advantages in molecular optical sensitivity, spatial and temporal resolutions, as well as non-ionizing radiation risk. [20, 69, 105, 106] When compared to traditional optical imaging modalities, PA tomography has superior imaging depth as both ballistic photons and diffused photons will induce photoacoustic signals. Meanwhile, the acoustic scattering is three orders of magnitude less than the optical scattering.[8]

The most common application of PA tomography in prostate cancer diagnosis is for imaging angiogenesis based on the high PA signal of blood.[107-109] Unfortunately, angiogenesis in the

prostate is not specific to prostate cancer.[110] One way to overcome this limitation is to develop active targeting probes which can selectively bind to the receptors or antigens overexpressed on the surface of cancerous cells, and thus highlighting the malignant tumor without labeling the normal tissues.[111-113] Several PA probes have been reported for prostate cancer detection *via* active targeting, including gold nanorods,[114] NIR dyes,[115, 116] and polymer nanoparticles.[117, 118] Nevertheless, the existing PA probes with absorption in the first near-infrared window (NIR-I: 800 – 1000 nm) suffer from limited penetration depth and imaging contrast. PA imaging in the second near-infrared window (NIR-II: 1000 – 1700 nm) is attracting more and more attention owing to the reduced absorption of endogenous chromophores, lower light scattering and higher maximum permissible exposure of light in this region, which leads to the enhanced photon penetration for *in vivo* deep-tissue imaging.[9, 11, 12, 19, 39, 43, 70, 71, 119-121] Significant breakthroughs have been made to develop organic semiconducting polymer nanoparticles (SPNs) for PA imaging in the NIR-II window, due to their good biocompatibility, excellent photostability, high mass extinction, and controllable dimensions.[9, 122-125] The majority of current NIR-II SPNs rely on the accumulation in tumor through enhanced permeability and retention (EPR) effect. Although this passive targeting approach has been widely used in clinics and in research, it preserves several drawbacks including the lack of cellular specificity for assessing the aggressiveness of tumors and the difficulty in controlling due to the random nature of the approach.[126] Therefore, the development of active targeted SPN in the NIR-II window is desirable for sensitive and accurate prostate cancer diagnosis.

Herein, we report an active targeted SPN that contains NIR-II absorbing semiconducting polymer (bis-isoindigo-based polymer (BTII)) with surface functionalized by glutamate urea ligands (2-[3-(1,3-dicarboxypropyl)ureido]pentanedioic acid (DUPA)), termed as BTII-DUPA

SPN, for targeted imaging of prostate cancer. DUPA is known to have high affinity to prostate specific membrane antigen (PSMA) which is overexpressed in prostate cancer.[127-130] More importantly, the expression level of PSMA increases with the aggressiveness and the recurrence of prostate cancer.[127, 129-131] The potentials of PSMA-based imaging for cancer diagnosis[116, 132-136] and fluorescence-guided surgery[137, 138] have been shown previously. In this study, based on the abovementioned advantages of NIR-II PA tomography over conventional imaging modalities, the BTII-DUPA SPN is expected to bring new opportunities for prostate cancer diagnosis and treatment. We investigated the effective targeting of BTII-DUPA SPN to PSMA-positive prostate cancer at the single-cell level in live cells by using a transient absorption (TA) microscope which provides sub-micrometer resolution and single-particle sensitivity. Then, the deep imaging depth and high imaging contrast in PA tomography were validated to reveal the potential of BTII-DUPA SPN for *in vivo* deep-tissue imaging. Next, the targeting specificity of BTII-DUPA SPN was demonstrated in living mice bearing both PSMA-positive and PSMA-negative tumors. Lastly, the nanoparticle distributions in tumor tissues after intravenous injection of BTII-DUPA SPN were studied in detail by TA microscopy.

3.2 Results and Discussion

3.2.1 Design and synthesis of PSMA-targeted BTII-DUPA SPN with NIR-II absorption

The donor-acceptor-acceptor (D-A-A) type conjugated polymer, BTII, was synthesized according to our previous report (**Figure 3.1a**).[139] The highly planarized BTII has exhibited an extended effective conjugation length with a lowered LUMO level,[139] which attributes to its narrow bandgap with effective absorption in the NIR-II window, and thus is served as the NIR-II absorbing PA agent in this study. Meanwhile, the targeting ligand DUPA was conjugated to the amphiphilic surfactant F127 and formed DUPA-F127-DUPA (Figure 1a).[140]

To prepare a series of water-soluble BTII-DUPA SPNs (**Figure 3.1b**) with different functionalities of DUPA on surface, DUPA-F127-DUPA was blended with F127 in different weight percentages (e.g. 50%, 70% and 100% of DUPA-F127-DUPA) and then co-precipitated with BTII. Considering the purity of DUPA-F127-DUPA was calculated to be ~70%, the actual feeding ratio, which means how many surfactants were initially added to the solution for nanoparticle synthesis, of DUPA-F127-DUPA was 35%, 49% and 70%, respectively. As a control group, the non-targeted BTII SPN was synthesized with BTII and F-127 only (0% DUPA-F127-DUPA). The DLS results show that the number-averaged hydrodynamic diameter of SPN gradually increases from 41.4 nm to 91.3 nm as the feeding ratio of DUPA-F127-DUPA increases from 0% to 70% (**Figure 3.2a**). Since more DUPA could make the particle bulkier, this result indicates the fine-tuned functionality of DUPA on the SPN surface. Transmission electron microscopy (TEM) further revealed the spherical morphology of SPNs and confirmed the size difference between the nanoparticles without DUPA-F127-DUPA (average diameter ~37.6 nm) and with 70% DUPA-F127-DUPA (average diameter ~81.0 nm) (inserted images in **Figure 3.2a**). The slightly smaller size estimated by TEM relative to DLS was probably due to the shrinkage of nanoparticles in the dry state during the preparation of TEM samples.[141]

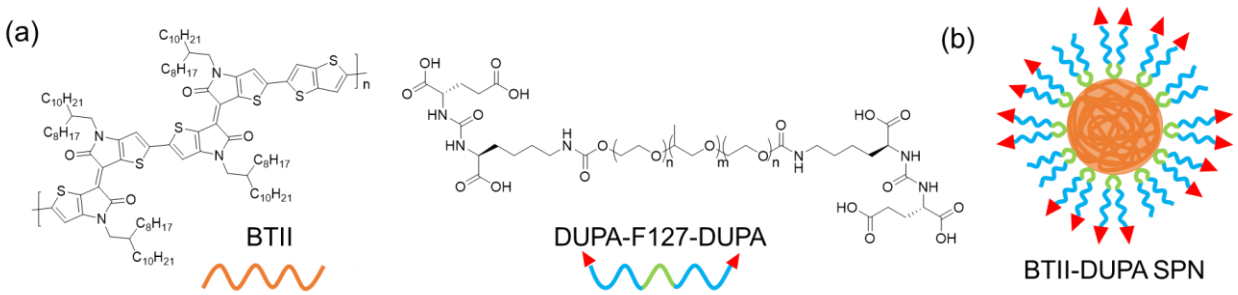

Figure 3.1 Design BTII-DUPA SPN. (a) Chemical structures of BTII and DUPA-F127-DUPA. (b) Schematic illustration of BTII-DUPA SPN.

The absorption spectra of BTII SPN and BTII-DUPA SPN were measured, showing identical absorption spectra in the NIR-II window (**Figure 3.2b)** with the same extinction coefficient of 22.5 $cm^{-1}mg^{-1}mL$ at 1100 nm (normalized by the mass concentration of BTII), which means that the conjugation of DUPA did not alter the optical properties of SPNs. The NIR-II absorption contributed to the efficient PA signal generation (**Figure 3.2c**), demonstrating that BTII-DUPA SPNs are effective NIR-II PA probes.

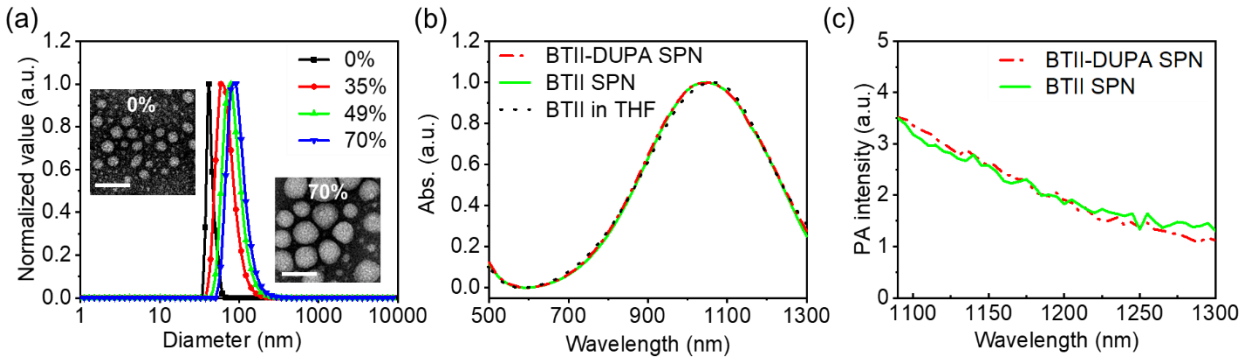

Figure 3.2 Characterization of BTII-DUPA SPNs. (a) DLS profiles of BTII SPN (0% DUPA-F127-DUPA) and BTII-DUPA SPN with 35%, 49% and 70% DUPA-F127-DUPA feeding ratio. Inserts: representative TEM images. Scale bars: 100 nm. (b) Absorption spectra of BTII in tetrahydrofuran (THF), BTII SPN and BTII-DUPA SPN with 70% DUPA-F127-DUPA feeding ratio. (c) PA spectra of BTII SPN and BTII-DUPA SPN with 70% DUPA-F127-DUPA feeding ratio.

3.2.2 Resolution and Sensitivity of TA Microscopy

We explored the feasibility of using TA microscopy for imaging the non-fluorescent BTII-DUPA SPN, which will allow the further in-depth study of BTII-DUPA SPN at cellular level. Experimentally, BTII-DUPA SPN was pumped by fs-pulses at 1045 nm and probed by fs-pulses at 853 nm, and the corresponding frequency difference (2150 cm^{-1}) lies in the "cell silent region" to ensure sensitive and specific detection in living systems (**Figure 3.3**).[142-144] To identify which mechanism contributes to the signal generation in the case of BTII-DUPA SPN detection under

our TA microscopy system settings, we retrieved the intensity and phase information of both the in-phase channel and quadrature channel from a lock-in amplifier, and the signals from BTII-DUPA SPN was found to correspond to an in-phase modulation of the probe beam (**Figure 3.4**).[145] Although both stimulated emission and ground-state depletion processes can lead to an in-phase signal, the possibility of stimulated emission is excluded since the probe wavelength is shorter than the pump wavelength.[146] Therefore, the generation of TA signals from BTII-DUPA SPN can be depicted by ground-state depletion mechanism where the population in ground-state is decreased by the photoexcitation of the pump beam and thus the sequent probe beam is absorbed less, yielding the TA signal (**Figure 3.5a**).

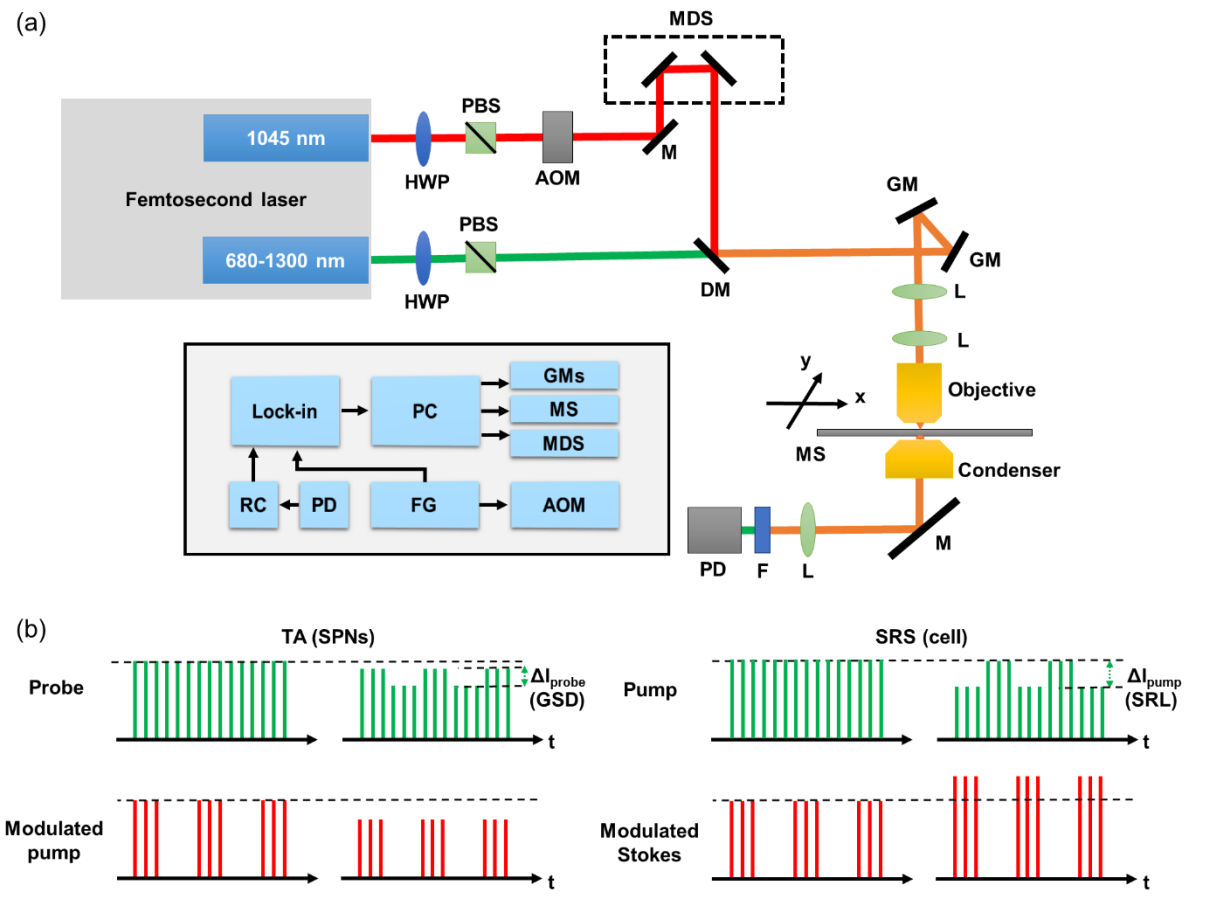

Figure 3.3 TA microscopy setup. (a) Layout of the system. HWP: half-wave plate; PBS: polarization beam splitter; AOM: acousto-optic modulator; L: lens; M: mirror; DM: dichromic mirror; F: filter; GM: galvo mirror; PD: photodiode; PC: personal computer; MS: motorized stage; MDS: motorized delay stage; RC: resonant circuit; FG: function generator. (b) Dectection schemes of TA and SRS peocesses. GSD: ground-state depeletion signal; SRL: stimulated Raman loss signal. In the TA process, the modulated 1045-nm laser beam is acting as the pump beam, and the other laser beam is acting as the probe beam. GSD signal is detected, when the absorption of the pump beam causes the less photons in the probe beam being absrobed. In the SRS process, the other laser beam is acting as the pump beam and the modulated 1045-nm laser beam is acting as the Stokes beam. SRL signal is detected, when the frequency difference between the pump and Stokes matches the viabrational transition of the chemical bond of interest.

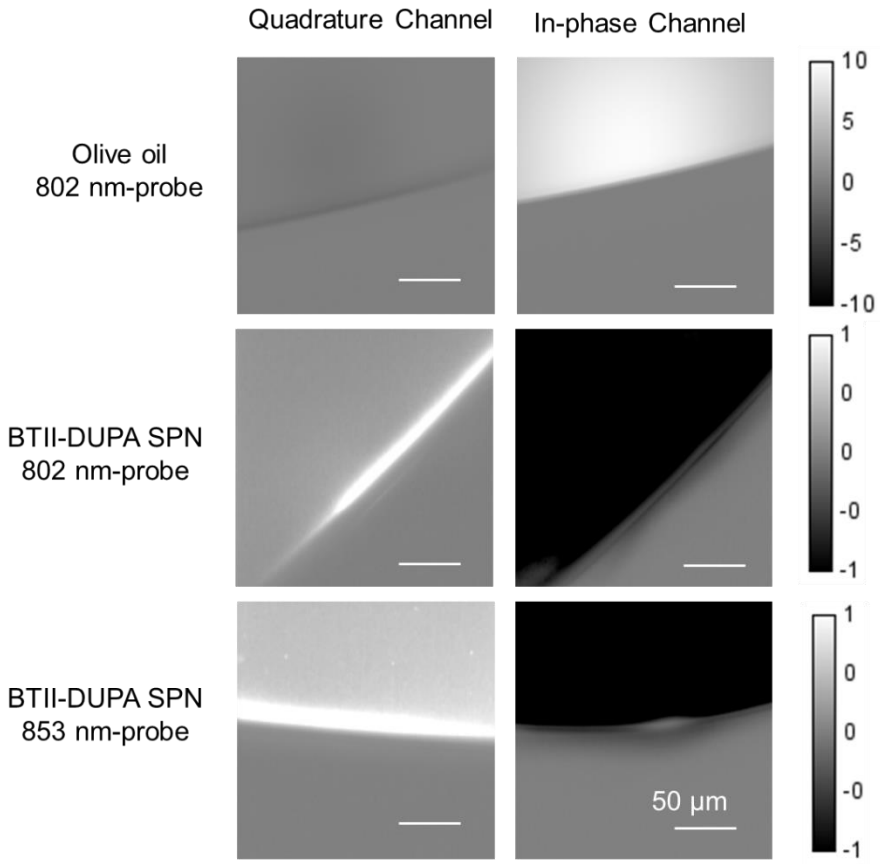

Figure 3.4 In-phase and quadrature-channel TA images of BTII-DUPA SPN and olive oil (a representative of C-H bonds). When imaging of olive oil, the power of pump beam was 100 mW at 1045 nm and the probe beam was 20 mW at 802 nm. When imaging of BTII-DUPA SPN, the power of pump beam was 10 mW at 1045 nm and the probe beam was 10 mW at 802 nm or 853 nm.

Next, the TA kinetics trace is shown in **Figure 3.5b**, of which the decay phase reflects the relaxion of excitons to the ground-state *via* non-radiative decay.[147] By fitting of the decay phase with a bi-exponential model, the non-radiative time constant is determined to be 2.79 ± 0.36 ps, which is 1 to 2 times shorter than the exciton lifetimes of most thiophene-based polymers.[148] The fast non-radiative decay implies the minimized fluorescence. On the other hand, the shorter non-radiative time constant contributes to the higher photothermal conversion efficiency and benefits the efficient generation of PA signal.[147]

The TA intensity of BTII-DUPA SPN solution displays a linear relationship with the concentration, which can be used for a quantitative analysis of intracellular BTII-DUPA SPN (**Figure 3.5c**). To further characterize the sensitivity and resolution of the TA microscopy system, individual BTII-DUPA SPNs were dispersed on a glass substrate by high-speed spin coating. Uniformly monodispersed nanoparticles were clearly visualized under a TA microscope (**Figure 3.5d**), demonstrating the single-particle sensitivity of the system. The intensity profile of an individual particle shows a full-width-half-maximum (FWHM) of 600 to 700 nm *via* Gaussian fitting (**Figure 3.5e** and **3.5f),** which indicates that TA microscopy can reach sub-micrometer resolution. Taken together, we have demonstrated that TA microscopy, as a unique non-fluorescence-based imaging modality, provides high sensitivity and sub-micrometer resolution for imaging BTII-DUPA SPN.

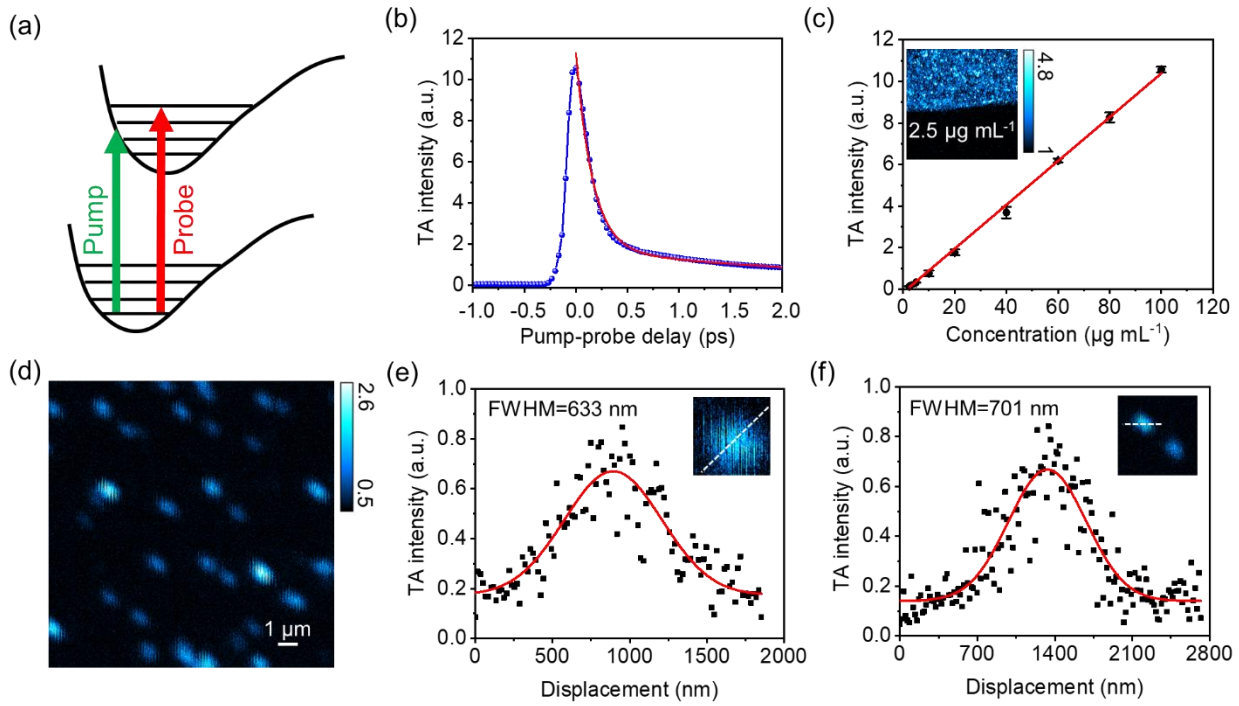

Figure 3.5 TA microscopy: high-sensitivity and high-resolution imaging of BTII-DUPA SPN. (a) Schematic illustration of the ground-state depletion mechanism. (b) Pump-probe decay curve of BTII-DUPA SPN and the corresponding biexponential decay fitting curve ($R^2 > 0.99$). (c) TA intensity as a function of BTII-DUPA SPN concentration and the corresponding linear fitting curve ($R^2 > 0.99$). Insert: TA image of 2.5 μg mL^{-1} BTII-DUPA SPN solution. (d) TA image of individual BTII-DUPA SPNs. (e,f) Intensity profiles of individual nanoparticles extracted from (d) and the coreesponding Gussaian fitting curves. Inserts: TA images of the corresponding nanoparticles. Error bars represent standard deviations. For imaging of BTII-DUPA SPN solutions, laser power was 10 mW for pump beam at 1045 nm and 10 mW for probe beam at 853 nm, before microscope. For imaging of BTII-DUPA SPN thin films, laser power was 2 mW for pump beam at 1045 nm and 2 mW for probe beam at 853 nm, before microscope. Error bars represent for standard deviations.

3.2.3 Specific Targeting In Vitro

The specific targeting of BTII-DUPA SPN to prostate cancer was examined *in vitro*. In order to investigate the biocompatibility of BTII-DUPA SPN, we first carried out cytotoxicity tests. No overt toxicity was found at concentrations up to 100 μg mL^{-1} of BTII-DUPA SPNs with different DUPA functionalities (**Figure 3.6**).

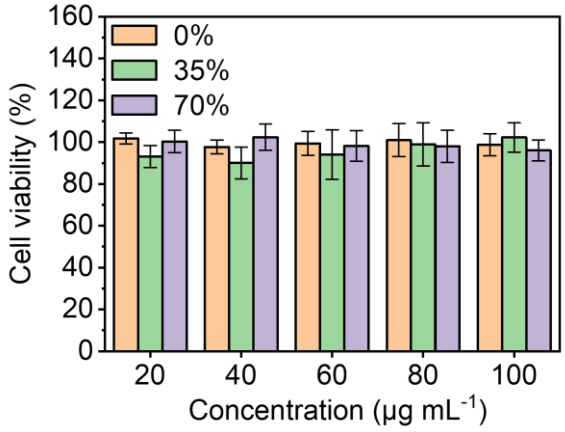

Figure 3.6 Cell viability of LNCaP cells after treated with BTII SPN (with 0% DUPA-F127-DUPA) or BTII-DUPA SPNs (with 35% or 70% DUPA-F127-DUPA feeding ratio) in different concetrarions for 24 h. Error bars represent for standard deviations.

We then determined the optimal DUPA functionality that confers maximal targeted cellular uptake. BTII-DUPA SPNs made with different feeding ratios of DUPA-F127-DUPA were incubated with LNCaP cells (PSMA-positive prostate cancer cell line) for 48 h and then imaged with TA microscopy (**Figure 3.7a**). While non-targeted BTII SPN had negligible uptake by LNCaP cells, obvious cellular uptake was observed by BTII-DUPA SPN made with 35% DUPA-F127-DUPA. This indicates that DUPA plays an essential role in the cellular binding and uptake. Furthermore, there is a significant increase of 4.1 $\pm$ 2.5-fold in intracellular TA intensity when the DUPA-F127-DUPA feeding ratio was increased from 35% to 70% (**Figure 3.7b**). Based on these results, BTII-DUPA SPN with 70% DUPA-F127-DUPA feeding ratio was used for the following study to achieve the maximal cellular targeting unless otherwise mentioned.

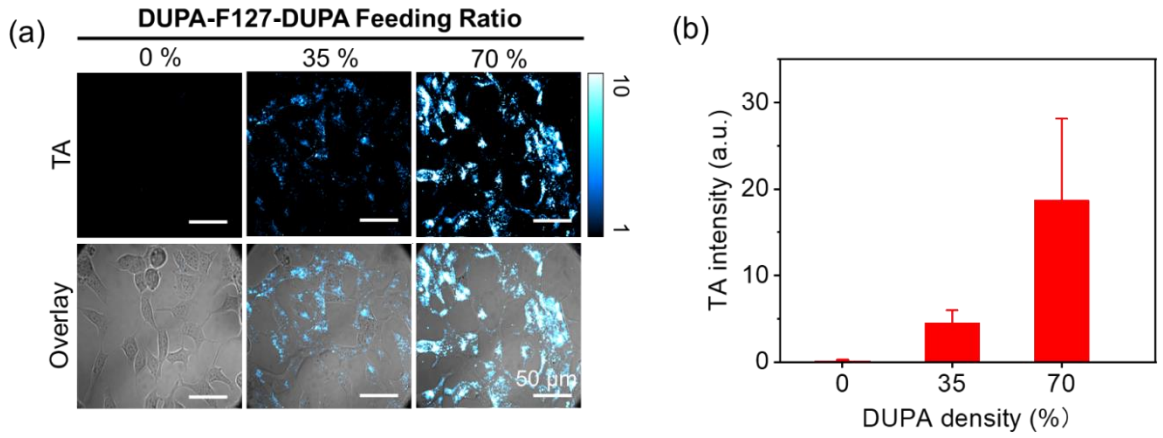

Figure 3.7 The optimal DUPA functionality that confers maximal targeted cellular uptake. (a) TA images of LNCaP cells after treated with 13.3 μg mL^{-1} BTII SPN (with 0% DUPA-F127-DUPA) or BTII-DUPA SPNs (with 35% or 70% DUPA-F127-DUPA feeding ratio) for 48 h. (b) Quantification of TA signals extacted from (a). All the TA images (cyan hot) were overlayed with transmission images (gray) to show the location of nanoparticles. Error bars represent for standard deviations.

To study the cellular uptake process of BTII-DUPA SPN into LNCaP cells, time-dependent TA imaging was performed. As shown in **Figure 3.8a**, BTII-DUPA SPN was first bound to the LNCaP cell membrane, then gradually endocytosed and accumulated inside cells. Such observation can be explained by the endocytic function of cell surface receptors that PSMA undergoes internalization constitutively, resulting in the enhancement in internalization of ligand-conjugates.[129, 149] On the contrary, no noticeable cellular uptake of the non-targeted BTII SPN was observed within 48 h (**Figure 3.8b**).

The targeting specificity of BTII-DUPA SPN to PSMA-positive cells were further validated by comparison among cell lines with different PSMA expression levels. While significant cellular uptake was found in LNCaP cells, minimal amount of BTII-DUPA SPN was presented in PC-3 cells (PSMA-negative prostate cancer cell line) and in HFB cells (PSMA-negative normal human fibroblast cell line) (**Figure 3.8c**). Additionally, the uptake by LNCaP cells was blocked in the presence of excess PMPA (PSMA inhibitor) (Figure 3.8c). The statistical

analysis of intracellular TA signal intensities confirms that cellular uptake in the control groups are significantly lower compared with the PSMA-positive LNCaP cell line (**Figure 3.8d**). In summary, we have shown that BTII-DUPA SPN is a specific targeted agent for PSMA-positive prostate cancer and used TA microscopy to reveal insights into the cellular targeting process.

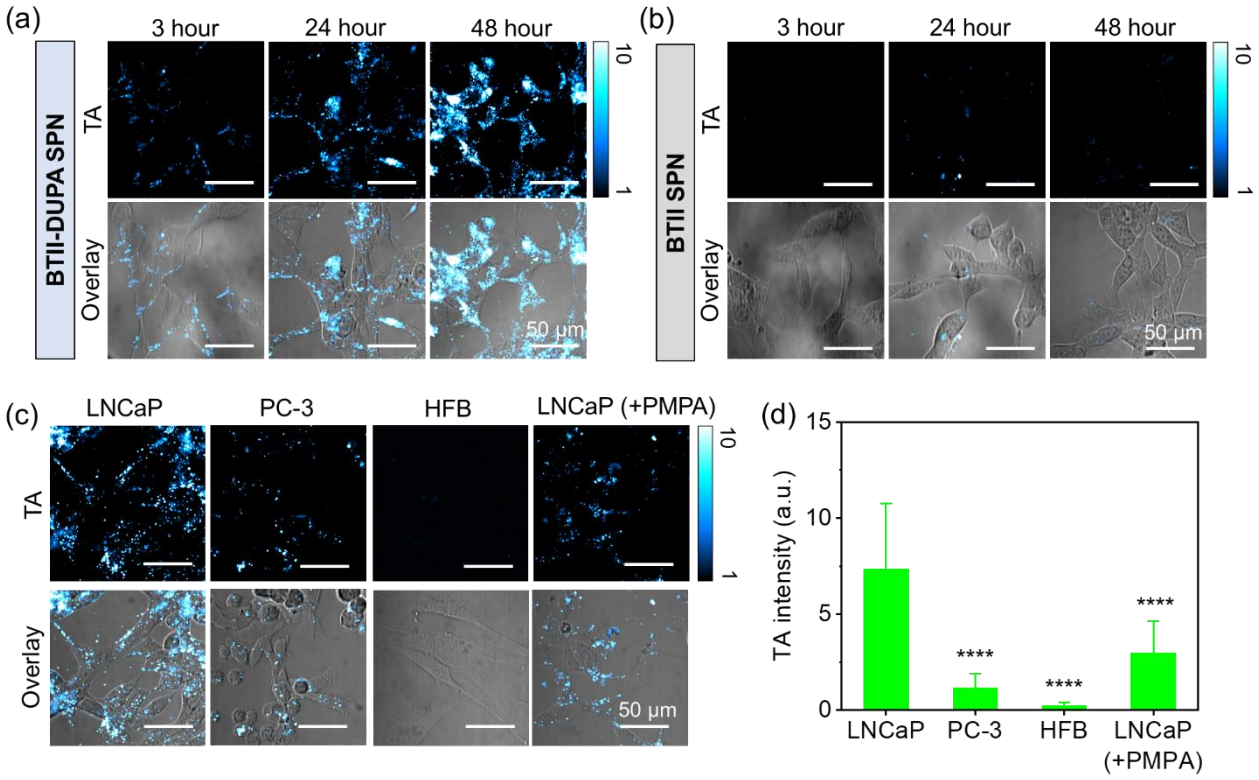

Figure 3.8 Specific targeting of BTII-DUPA SPN to prostate cancer cells reaveled by *in vitro* TA microscopy. Time dependent TA imaging of LNCaP cells treated with 13.3 μg mL^{-1} of (a) BTII-DUPA SPN (with 70% DUPA-F127-DUPA feeding ratio) or (b) BTII SPN (with 0% DUPA-F127-DUPA). TA images were taken after 3 h-, 24 h- and 48 h-treatment. (c) TA images of LNCaP cells, PC-3 cells, HFB cells, and LNCaP cells with excess PMPA. Cells were treated with 13.3 μg mL^{-1} BTII-DUPA SPN (with 70% DUPA-F127-DUPA feeding ratio) for 48 h. LNCaP: PSMA-postive prostate cancer cell line, PC-3: PSMA-negative prostate cancer cell line, HFB: PSMA-negative normal human fibroblast cell line, PMPA: PSMA inhibitor, 100 μg mL^{-1}. (d) Quantatitive ananlysis of TA intensities extrated from (c). All the TA images (cyan hot) were overlayed with transmission images (gray) to show the location of nanoparticles. Error bars represent standard deviations. **** $P<0.0001$ in t-test with equal variance. Laser power was 20 mW for pump beam at 1045 nm and 10 mW for probe beam at 853 nm, before microscope.

3.2.4 Imaging Contrast of PA Tomography in the NIR-II Window

The imaging contrast and depth in deep tissue, in addition to the targeting functionality, are also vital to be evaluated. To investigate the *in vivo* PA imaging contrast in the NIR-II window, multispectral analysis was performed by using least absolute shrinkage and selection operator (LASSO) analysis to specify the source of PA signals in images. Three major components were considered in multispectral analysis, including blood, lipid and BTII-DUPA SPN. The PA spectra of those pure components were recorded by PA spectroscopy and used as reference spectra for LASSO decompositions (**Figure 3.9a**). Then, Matrigel-containing solutions of BTII-DUPA SPN (50 μL, 20 μg mL^{-1}) were administrated into the dorsal area of mice and PA images of the region of interest (ROI) were recorded over the NIR-II wavelengths (1100 nm – 1300 nm) with 20 nm interval. The results after multispectral analysis are shown in **Figure 3.9b-e**. Signals of lipid were mostly distributed in the skin and only small amount of blood signals were found in the tissue background, while strong BTII-DUPA SPN signals were found in the injection site underneath the skin. It is worth noting that the image acquired at a single wavelength of 1100 nm (**Figure 3.9f**) is identical to the concentration image of BTII-DUPA SPN from multispectral analysis (Figure 4d), which suggests that the PA signals at 1100 nm are dominated by BTII-DUPA SPN with minimal tissue background signals.

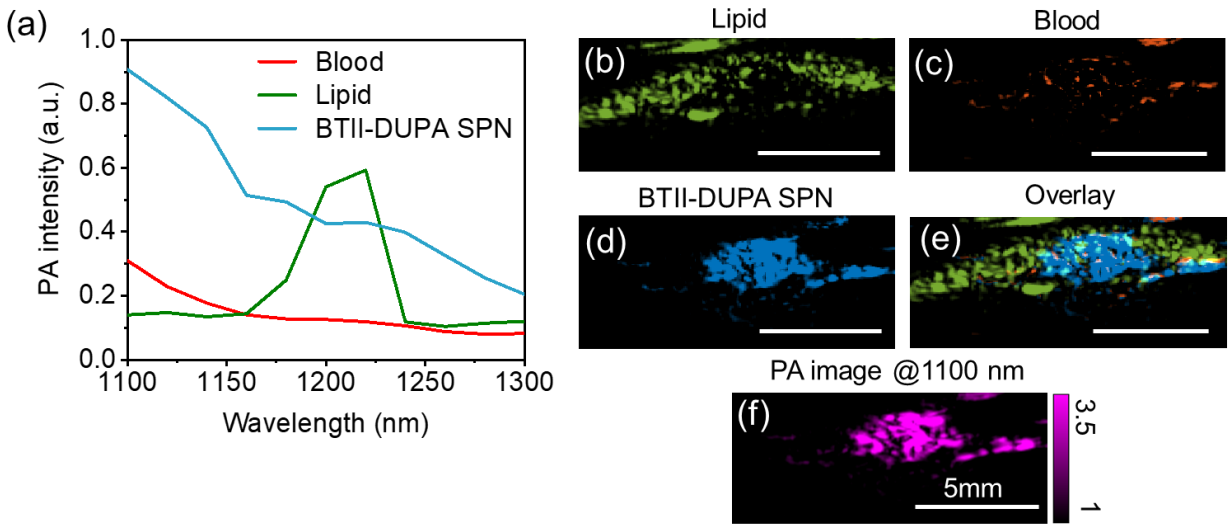

Figure 3.9 Suprior imaging contrast of PA tomographic imaging of BTII-DUPA SPN in the NIR-II window. (a) PA spectra of lipid, blood and BTII-DUPA SPN solution, which were used as reference spectra for LASSO analysis. b-d) LASSO retrieved concetration images of (b) lipid (green), (c) blood (red), and (d) BTII-DUPA SPN (blue) in mouse skin with subcutaneous injection of Marigel containing BTII-DUPA SPN (50 μL, 20 μg mL^{-1}). (e) The overlayed image of (b)(c)(d). (f) PA tomographic imaging (magenta) of the same ROI in mouse skin as beforementioned at 1100 nm. Laser energy density was tuned to 15 mJ cm^{-2} at each wavelength.

In comparison, PA images of Matrigel-containing phosphate-buffered saline (PBS) solution after subcutaneous injection display negligible PA signals close to the background at 1100 nm (**Figure 3.10a**). Furthermore, there exhibits a linear relationship between the PA signal at 1100 nm and the concentration of BTII-DUPA SPN *in vivo* (**Figure 3.10a-d**). In view of the outstanding imaging contrast of BTII-DUPA SPN at around 1100 nm, the following experiments were carried out with a 1064 nm Nd:YAG laser unless otherwise mentioned, which is one of the most reliable and economical nanosecond lasers and will accelerates the clinical translation process.

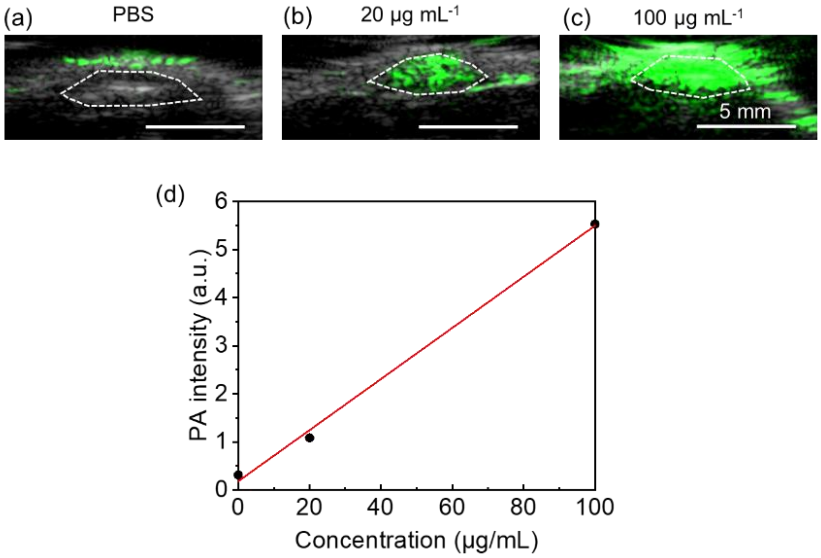

Figure 3.10 PA/US imaging of mouse skin with subcutaneous injection of 50 μL Marigel containing (a) PBS, (b) 20 μg mL^{-1} BTII-DUPA SPN and (c) 100 μg mL^{-1} BTII-DUPA SPN, respectively. (c) 100 μg mL^{-1} BTII-DUPA SPN, respectively. (d) PA intensity as a function of BTII-DUPA SPN concentration and the corresponding linear fitting curve ($R^2 > 0.99$). Laser energy density was tuned to 15 mJ cm^{-2} at 1100 nm.

3.2.5 Imaging Depth of PA Tomography in the NIR-II Window

Next, the imaging depth at 1064 nm was assessed by using chicken-breast tissue as the scattering medium. BTII-DUPA SPN solution was sealed in a transparent polyurethane tube and the PA images at different depths were collected by changing the number of layers of chicken-breast tissues below and above the tube simultaneously. The corresponding laser energy density was ~45 mJ cm^{-2} and 100 images were acquired and averaged at the same position. The polyurethane tube containing 80 μg mL^{-1} BTII-DUPA SPN solution can be visualized at an imaging depth of 4.2 cm with a signal-to-noise ratio (SNR) of 29.2 (**Figure 3.11a**). Notably, the achieved imaging depth with a low concentration of BTII-DUPA SPN is readily larger than the normal size of a human prostate (3.5 cm), indicating a promising potential application in whole-prostate imaging. Furthermore, by increasing the BTII-DUPA SPN concentration to 200 μg mL^{-1}, the SNR was increased to 72.3 at 4.2 cm depth. The SNR of PA signal was plotted as a function

of depth and was fitted into an exponential function based on Lambert–Beer's law (**Figure 3.11b**).[150] The imaging depth-limit where the SNR of BTII-DUPA SPN was equivalent to the SNR of tissue background (SNR = 20) is calculated to be 4.5 cm and 5.7 cm with 80 μg mL^{-1} and 200 μg mL^{-1} BTII-DUPA SPN, respectively.

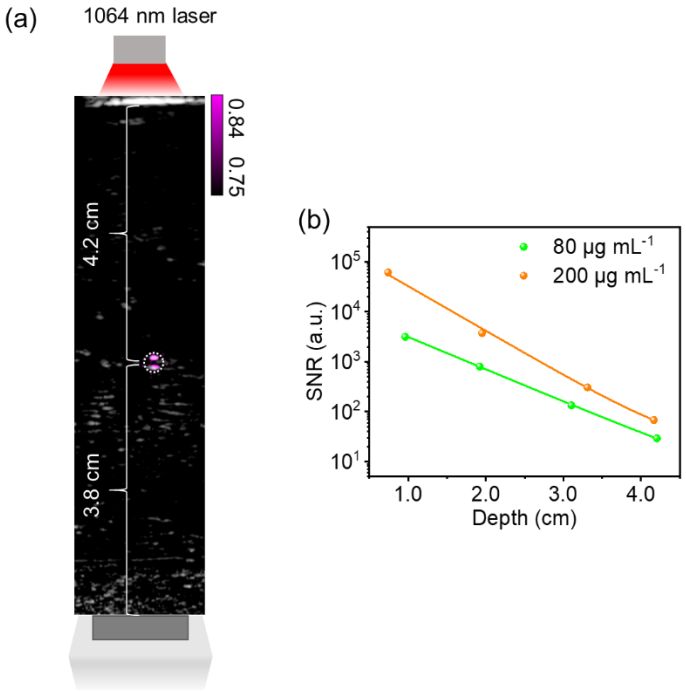

Figure 3.11 Centimeter-deep imaging depth of PA tomographic imaging of BTII-DUPA SPN in the NIR-II Window. (a) PA/ultrasound co-registered image of the 80 μg mL^{-1} BTII-DUPA SPN in a transparent polyurethane tube placed at 4.2-cm depth in chicken breast tissue. PA image is in magenta and ultransound image is in gray. Laser energy density was tuned to 45 mJ cm^{-2} at 1064 nm. (b) SNR of 80 μg mL^{-1} or 200 μg mL^{-1} BTII-DUPA SPN solution as a function of depth from the illuminated tissue surface concentration and the corresponding linear fitting curve (R^2 > 0.99). Laser energy density was tuned to 45 mJ cm^{-2} at 1064 nm.

3.2.6 In Vivo Imaging of PSMA-Positive Prostate Tumor

The tumor targeting capability of BTII-DUPA SPN to PSMA-positive prostate cancer *in vivo* was investigated on living mice bearing LNCaP (PSMA-positive) and PC-3 (PSMA-negative) xenografts on opposite flanks (**Figure 3.12a**). To statistically evaluate the targeting of BTII-DUPA SPN to PSMA-positive tumor, the measurements were repeated with 5 nude mice and consistent

results were obtained. Before systemic administration of nanoparticles, tumors show negligible PA signals due to the minimal absorption of blood and lipid in the NIR-II region (**Figure 3.12b**), which is consistent with our previous results (Figure 3.8).[122] After intravenous injection of BTII-DUPA SPN into the mice, the PA signal increased significantly throughout the entire LNCaP tumor while much less accumulation of BTII-DUPA SPN was observed near the surface of PC-3 tumor (Figure 5b). At 6 h post-injection time, the PA intensities reached maxima in both tumors, which were 3.9-fold and 2.0-fold higher than the tissue background in the LNCaP tumor and the PC-3 tumor, respectively (Figure 3.11b). Importantly, most of the PA signal was eliminated in PC-3 tumor after 72 h post-injection, while the PA signal intensity in LNCaP tumor remained as high as 2.1-fold greater than the tissue background (Figure 3.11b). To understand the targeting of BTII-DUPA SPN in LNCaP and PC-3 tumors quantitatively, the PA intensity increase was plotted against the post-injection time and fitted by a bi-exponential model (**Figure 3.12c**):

$$C(t)=-A\exp(-\alpha t) + B\exp(-\beta t)$$

where A and B intercepts on C(t) for each exponential segment of the curve; α and β represent rate constants in the distribution phase and elimination phase, respectively.[151-153] The distribution half-lives ($\tau_{1/2\alpha}$) and elimination half-lives ($\tau_{1/2\beta}$) were extracted from the fitting curves and summarized in **Figure 3.12d**. The results reveal that BTII-DUPA SPN distributed 1.5-fold faster in LNCaP tumor ($\tau_{1/2\alpha}$= 1.3±0.5 h) than that in PC-3 tumor ($\tau_{1/2\alpha}$= 1.9±0.5 h), while the retention was nearly 2-fold longer in LNCaP tumor ($\tau_{1/2\beta}$ = 41.6±8.7 h) than that in PC-3 tumor ($\tau_{1/2\beta}$ = 21.6±3.9 h). Also, the area under curve (AUC) was calculated as a metric of nanoparticle accumulation in tumors,[154] which suggests 3.8-fold enhanced accumulation of nanoparticles in the LNCaP tumor as compared to that in the PC-3 tumor. The difference in distribution and elimination kinetics of BTII-DUPA SPN between LNCaP tumor and PC-3 tumor reflects the advantages of active

targeting over the passive targeting through EPR effect, that it can differentiate PSMA-positive prostate tumor from other tumors.

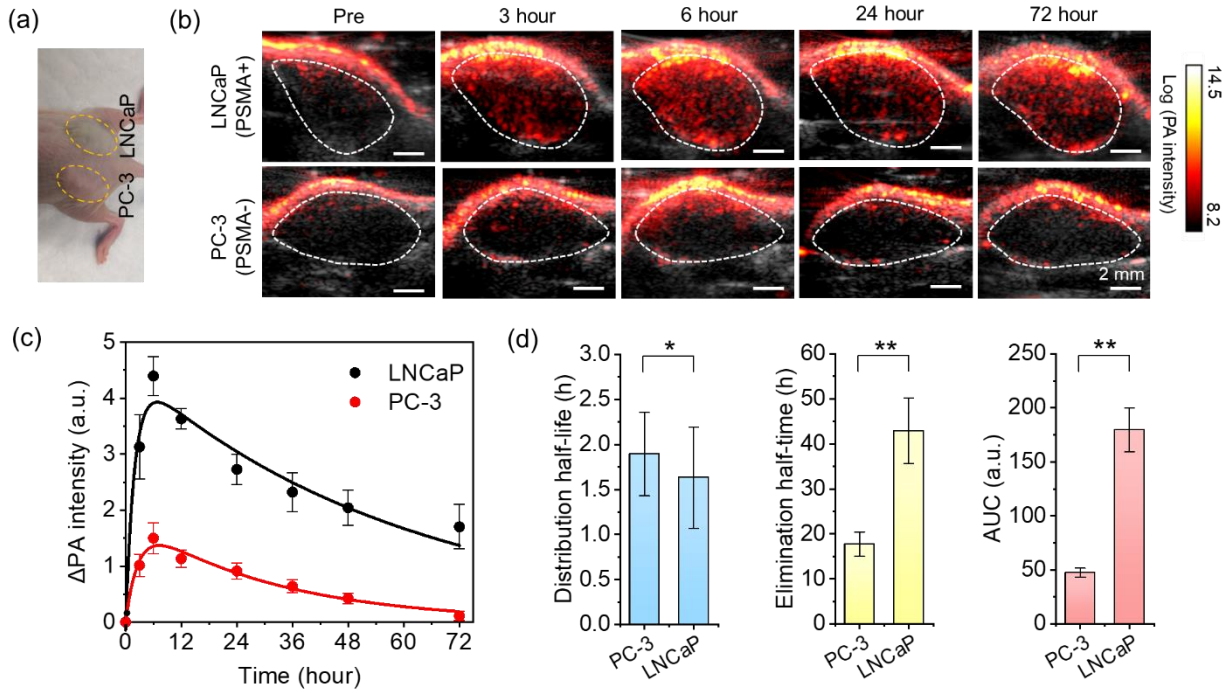

Figure 3.12 *In vivo* PA tomographic imaging of PSMA-positive prostate tumor. (a) Photograph of a nude mouse bearing LNCaP (PSMA-positive) and PC-3 (PSMA-negative) xenografts on opposite flanks. (b) Representative PA/ultrasound co-registered images of LNCaP and PC-3 tumors before and after intravenous injection of BTII-DUPA SPN solution (200 μL, 800 μg mL^{-1}). Ultrasound images (gray) delineate the tumor boundaries, while the PA images (hot red) show the accumulation and distribution of BTII-DUPA SPN in tumor region. (n=5) (c) Quantification of PA intensity increase in LNCaP and PC-3 tumors as a function of time and the corresponding biexponential fitting curves. $R^2 > 0.99$ for both fitting curves (n=5). ΔPA intensity was calculated as the PA signal intensity in the tumor region at different time points subtracted by the PA signal intensity in the tumor region at pre-injection. (d) The calculated distribution half-lives, elimination half-lives and area under curve (AUC) of BTII-DUPA SPN in LNCaP and PC-3 tumors (n=5). Laser energy density was tuned to 20 mJ cm^{-2} at 1064 nm. *P<0.1, **P<0.01.

3.2.7 Ex Vivo Imaging of Major Organs and Tumors

To evaluate the biodistribution of BTII-DUPA SPN, *ex vivo* PA imaging of tumors and major organs was performed at 72 h post-injection time. BTII-DUPA SPN had noticeable accumulation in the major reticuloendothelial system (RES) organs such as liver and spleen, but

minimal accumulation in other organs **(Figure 3.13a)**.[141] Nevertheless, by virtue of the targeting effect, BTII-DUPA SPN shows 2.3-fold higher accumulation in the LNCaP tumor as compared with the PC-3 tumor **(Figure 3.13b)**, which is consistent with the real-time PA measurements *in vivo*.

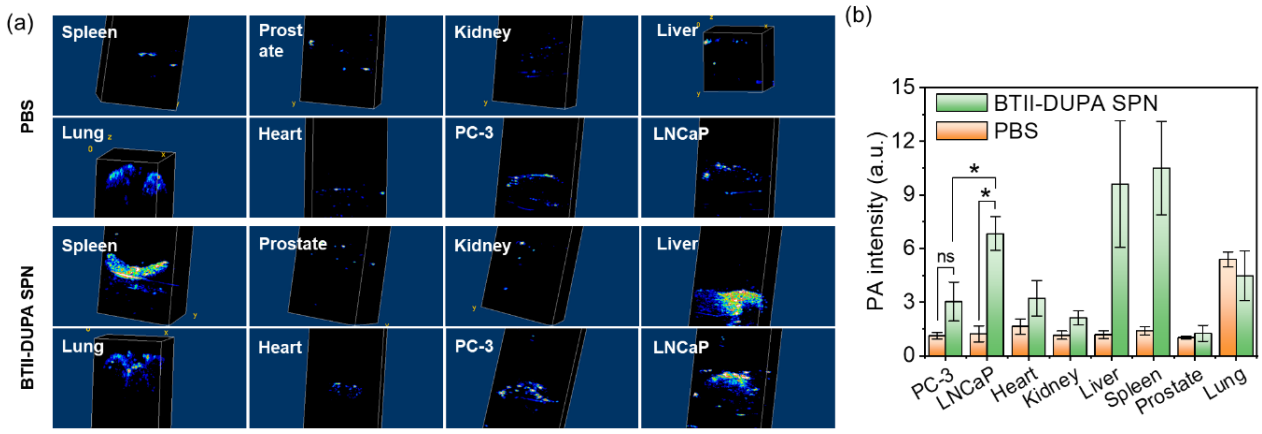

Figure 3.13 *Ex vivo* PA imaging major organs and tumors. (a) PA images 72 h after intravenous injection of PBS (200 µL) or BTII-DUPA SPN solution (200 µL, 800 µg mL^{-1}). (b) Quantification of PA signals extracted from (a). Laser energy density was tuned to 20 mJ cm^{-2} at 1064 nm. *P<0.1, ns: no significant difference in paired t-test. Error bars represent standard error of mean.

3.2.8 In vivo toxicity of BTII-DUPA SPN

Moreover, negligible weight loss was observed in mice (**Figure 3.14a**) and no noticeable histopathological damage was observed in major organs after intravenous administrations of BTII-DUPA SPN (**Figure 3.14b**). These results verify the *in vivo* biocompatibility of BTII-DUPA SPN.

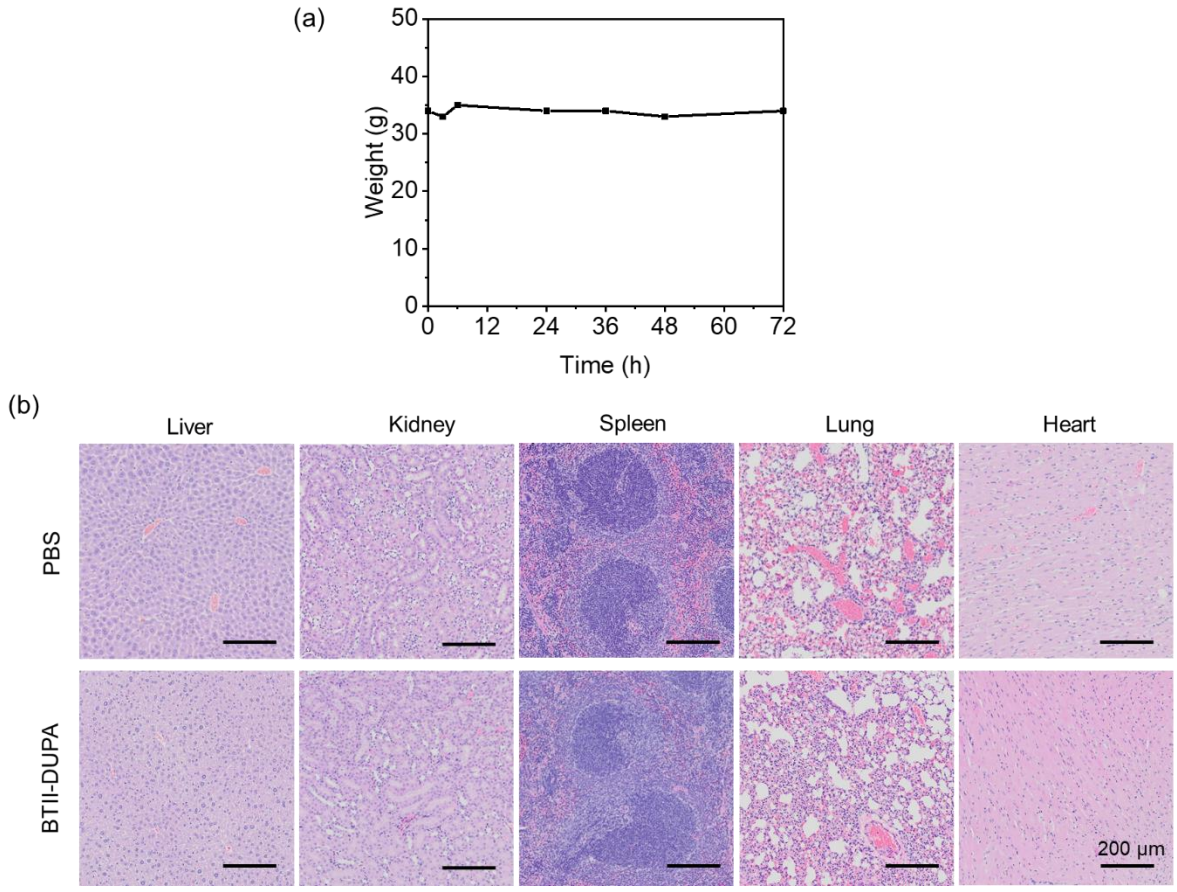

Figure 3.14 *In vivo* toxicity of BTII-DUPA SPN. (a) Body weight data of LNCaP- and PC-3-tumor-bearing mice after intravenous administration of BTII-DUPA SPN (200 μL, 800 μg mL^{-1}). (b) Histological analysis of major organs 72 h after intravenous injection of PBS (200 μL) or BTII-DUPA SPN solution (200 μL, 800 μg mL^{-1}).

3.2.9 Mapping of BTII-DUPA SPN inside Tumor Tissue

The large-area mapping of the whole-tissue slices was achieved by TA microscopy to study the distribution of BTII-DUPA SPN in different tumors at cellular level with high spatial resolution. The probe beam was switched between 853 nm and 802 nm, while the pump beam was fixed at 1045 nm. We hypothesized that with a probe beam at 853 nm only BTII-DUPA SPN will contribute to TA signal, and with a probe beam at 802 nm the detected signal contains both the stimulated Raman scattering (SRS) signal of C-H bonds dominating in cells[155] and some TA signal of BTII-DUPA SPN due to its broad absorption at 800-1100 nm. Our hypothesis was first

validated by imaging of LNCaP and PC-3 tumor tissue slices from the mice without nanoparticles administration, both of which showed negligible signals at 853 nm-probe (**Figure 3.15a**). Then, tissue imaging was performed with LNCaP and PC-3 tumors harvested at 72 h after intravenous injection of BTII-DUPA SPN (**Figure 3.15b**). In the PC-3 tumor tissue slice, relatively intense TA signals only appeared around the blood vessels (BVs, indicated by yellow arrows in the images), meaning that some of the BTII-DUPA SPN escaped from the blood vessels and gradually diffused into the nearby tumor tissue through EPR effect, but most nanoparticles inside the tissue were washed away by blood circulation (**Figure 3.15c**). On the contrary, substantial amount of BTII-DUPA SPN was presented throughout the entire tissue slice of LNCaP tumor, indicating specific binding of nanoparticles to PSMA-positive cancer cells and the consecutive cellular endocytosis to retain the nanoparticles (Figure 3.60). This also highlights the ability of BTII-DUPA SPN to specifically label the entire prostate tumor that has high PSMA expression level.

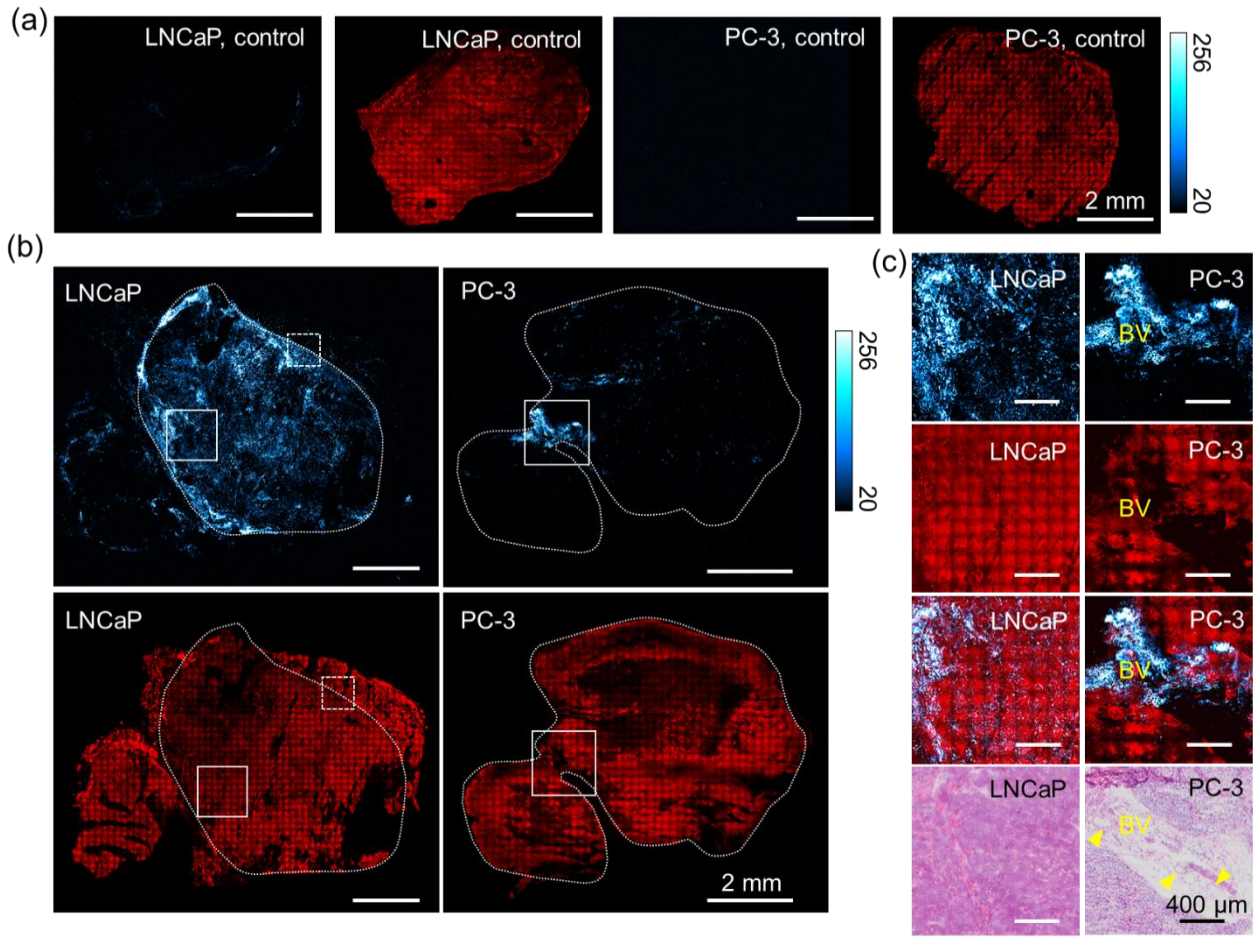

Figure 3.15 High-resolution mapping of BTII-DUPA SPN inside tumor tissue slices. a) and b) SRS (red) and TA (cyan hot) images of LNCaP and PC-3 tumor tissues harvested 72 h after intravenous injection of (a) PBS (200 μL) or (b) BTII-DUPA SPN solution (200 μL, 800 μg mL^{-1}). c) Zoom-in images of the ROI indicated by white solid frames in (b), and their corresponding adjacent H&E staining images. The blood vessels (BVs) are indicated by yellow arrows. Laser power was 20 mW for pump beam at 1045 nm and 10 mW for probe beam at 853 nm or 20 mW for probe beam at 802 nm, before microscope.

Taking advantage of the subcellular resolution of TA microscopy system, the cellular binding and uptake by individual cells were clearly visualized in LNCaP tissue at the single-cell level (**Figure 3.16a**). On the other hand, only a few nanoparticles were randomly trapped in PC-3 tissue without any intracellular accumulation. Interestingly, an obvious separation of nanoparticle distribution between cancerous tissue (left-side of the image) and normal tissue (right-side of the image) at the LNCaP tumor margin was observed, further confirming the binding specificity to PSMA-positive cells (**Figure 3.16b**). In summary, BTII-DUPA SPN shows a great potential for prostate cancer diagnosis with high targeting specificity, and the clear tumor margin delineated by BTII-DUPA SPN will allow precision tumor resection with intraoperative margin assessment.

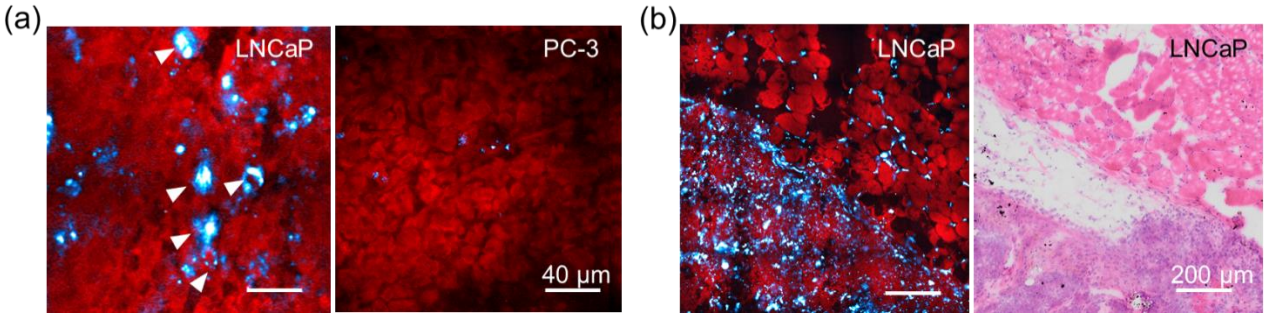

Figure 3.16 Imaging of BTII-DUPA SPN in tumor tissues at cellular level. (a) TA/SRS images of LNCaP and PC-3 tumor tissues at single-cell level. (a) TA/SRS image of the LNCaP tumor margin indicated by white dotted frame in Figure 3.14b, and the adjacent H&E staining image. Laser power was 20 mW for pump beam at 1045 nm and 10 mW for probe beam at 853 nm or 20 mW for probe beam at 802 nm, before microscope.

3.2.10 Discussion

In order to rationally design the targeted PA probe and pushing towards bench-to-bedside translation, insights into the interaction of nano-sized probes with the biological systems at various levels (i.e., organ system, organ, tissue, and cell) are of paramount importance. The high heterogeneity nature of tumor tissues results in the inconsistency in the *in vivo* studies.[156] In addition, the targets are localized at sub-cellular compartments and are not uniformly distributed

throughout a single tumor.[126] Accordingly, it is essential to study SPNs at cellular level by using advanced non-fluorescence microscopy. Although *in vivo* PA tomographic imaging of tumors with SPNs have been extensively studied[125] and more recently NIR-II photoacoustic microscopy imaging of living tissues with SPNs has also been reported,[157] investigation at cellular level has been deficient so far. On the other hand, PA agents usually show low or no fluorescence signals for conventional fluorescence imaging. As an efficient PA agent, the conversion of absorbed optical energy into thermal energy and later acoustic signal is through non-radiative decay, and the radiative decay (fluorescence emission) is inactivated, resulting in minimized fluorescence signal generation.[7]

In TA microscopy, the change of probe beam induced by the transient absorption of the pump beam is sensed. The advantages of TA microscopy include label free, high sensitivity, high temporal and spatial resolution, low photodamage, and inherent sectioning capability.[158-160] TA microscopy has been applied for imaging of metal nanoparticles,[146, 161, 162] carbon nanomaterials,[163, 164] and non-fluorescent chromophores.[165-168] highlighting its potential as an enabling tool for label-free characterization of materials.

PA tomorgaraphy and TA microscopy are two very different methods, and we harnessed the advantages of each technique to study the NIR-II SPN. PA tomorgraphy provided deep imaging depth for *in vivo* imaging and potential clinical applications, but its spatial resolution is usually limited. On the other hand, TA microscopy offered sub-micrometer resolution and ultra-high for imaging non-fluorescent agents, so it is suitable for *in vitro* characterization at single-cell level. In this work, TA microscopy helped us to determine the efficiency, kinetics, and specificity of BTII-DUPA SPN for targeting tumor cells and to map the distribution of SPN inside a tumor tissue at a

much higher resolution, which not only confirmed our *in vivo* PA tomography findings but also provided a deep insight of the tumor targeting mechanisms.

To our best knowledge, it is the first report to utilize TA microscopy to investigate the interaction between non-fluorescent PA probes and the biological systems at single-cell level, which circumvents the heterogeneity in tissues and provides robust evidence for the specific targeting to the sub-cellular compartments. The combined PA tomography and TA microscopy can serve as a new platform to study non-fluorescent PA agents at multiscale to gain complete understanding of their behaviors in biological systems and paves a way for the new development of functionalized PA agents.

3.3 Summary

We have developed NIR-II absorbing BTII-DUPA SPNs with PSMA-targeting function for prostate cancer detection through PA tomography. The unique NIR-II absorption profile of BTII-DUPA provides high SNR in tissue and an imaging depth (>4.2 cm) greater than the size of the entire human prostate. The targeting specificity is investigated at multi-scales from single-cell to whole-organ level by TA microscopy and PA tomography. TA microscopy provides sub-micrometer resolution and ultra-high sensitivity for studying SPN properties at single-cell level. By using TA microscopy, optimal parameters for targeting tumor cells are determined *in vitro* and multiple evidences are revealed to support the specific targeting of BTII-DUPA SPN to prostate cancer cells. The PA tomography study further validates the specific targeting of BTII-DUPA SPN to PSMA-positive prostate tumor *in vivo*. Lastly, the distribution of BTII-DUPA SPN inside a tumor tissue is mapped by TA microscopy to confirm the PA results and to differentiate the active targeting from the EPR effect. Based on the established correlation between prostate cancer progression and PSMA expression[127-132, 136], we expect that BTII-DUPA SPNs can be used not

only for tumor detection but also for evaluation of aggressiveness and recurrence of prostate cancer with superior imaging contrast and depth in NIR-II PA tomography.

3.4 Experimental Section

Synthesis of BTII: All reagents purchased from suppliers were used without further purifications otherwise noted. Monomer BTII-M: This compound was synthesized according to the literature.[139] ^{1}H NMR (300 MHz, $CDCl_3$, ppm) δ: 6.88 (s, 2H), 6.67 (s, 2H), 3.68 (m, 8H), 1.98 (s, 2H), 1.81 (s, 2H), 1.40 – 1.21 (m, 128H), 0.87 – 0.81 (m, 24H). ^{13}C NMR (75 MHz, $CDCl_3$, ppm) δ: 170.48, 169.74, 152.16, 149.50, 145.64, 122.66, 119.02, 118.24, 116.03, 115.13, 114.69, 107.20, 46.96, 46.45, 37.29, 37.15, 32.01, 31.63, 31.35, 30.34, 30.14, 29.84, 29.76, 29.69, 29.48, 26.71, 26.51, 22.80, 14.24. Polymer BTII: To a Schlenk tube charged with a stir bar, BTII-M (449.8 mg, 0.2463 mmol), 2,5-is(trimethylstannyl)thieno[3,2-b]thiophene (114.7 mg, 0.2463 mmol), $Pd_2(dba)_3$ (5.64 mg, 0.00616 mmol), Tri(*o*-tolyl)phosphine (3.00 mg, 0.00985 mmol) and 20 mL of toluene were added. The resulting solution was bubbled with argon for 20 min, and the mixture was stirred for 36 h at 110 °C. After the polymerization was complete, the mixture was taken up and precipitated into methanol. The solids were collected by a Soxhlet thimble, which was purified by Soxhlet extraction successively with methanol, acetone, hexane and chloroform. To remove residual catalyst, *N*,*N*-diethyl-2-henyldiazenecarbothioamide was added to the chloroform fraction, and the mixture was stirred for 30 min at 60 °C before being precipitated into methanol. The collected polymer was dried at 60 °C under vacuum. (412 mg, 93%) The exact molecular weight of BTII cannot be accessed from the GPC measurements. Similar observations with TII substructures were previously reported, where thienoisoindigo polymers are believed to interact strongly with the column material.[54, 139, 169]

Synthesis of DUPA-F127-DUPA: All reagents were purchased and used without further purificationunless otherwise noted. This compound was synthesized according to the literature.[140] Triphosgene (883 mg, 3 mmol) was added in DCM (20 mL) and stirred at 0 ^{o}C. A mixture solution of DIPEA (3.4g, 26.6 mmol) and HCl.Cbz-Lys-Ot-Bu (3 g, 8.1mmol) in dichloromethane (DCM) (20 mL) was added dropwise to the triphosgene solution over 1 h. A solution of L-glutamic acid di-tert-butyl ester hydrochloride (2.4 g, 8.1 mmol) and DIPEA (2.3 g, 17.9 mmol) in DCM (20 mL) was then added into the mixture and stirred for 2 h. The mixture was washed with 2 M $NaHSO_4$ (2× 100 mL) and brine (50 mL) and dried over sodium sulfate to yield a yellow oil. Purification by column chromatography (SiO_2) afforded the desired product as clear oil (3.0 g, 4.8 mmol, 60%). ^{1}H NMR (300 MHz, $CDCl_3$) δ (ppm): 7.38-7.28 (m, 5H), 5.16-5.01 (m,5H), 4.37-4.29 (m,2H), 3.21-3.14 (m,2H), 2.33-1.22 (m,37H). Ammonium formate (1 g, 16.1 mmol) and 10% Pd/C (0.1g) was added to a solution of (S)-2-[3- (5-benzyloxycarbonylamino-1-tert-butoxycarbonylpentyl)ureido]-pentanedioic acid di-tert-butyl ester (1 g, 1.61 mmol) in ethanol (20mL). The solution was stirred at room temperature for 20 h. Then it was filtered to remove the solid and dried in a rotavapor to remove the solvent, yielding the product as a clear oil (750 mg, 95%). ^{1}H NMR (300 MHz, $CDCl_3$) δ (ppm): 5.20-5.17 (m, 2H), 4.36-4.29 (m,2H), 2.71-2.59 (m,2H), 2.40-2.21 (m,2H), 2.10-1.08 (m,35H). To a 20mL DCM solution of F127 (4 g, 0.32 mmol) was added CDI (154 mg, 0.96 mmol). The solution was stirred at room temperature for 20 h. Then, after adding DCM (40 mL) into the solution which was washed by HCl (20 mL, 0.1M) and brine (20 mL) and dried with sodium sulfate. After removing the solvent, the white solid was dissolved into DCM (20mL) and (S)-2-[3-(5-amino-1-tert-butoxycarbonylpentyl) ureido]pentanedioic acid di-tert-butyl ester (375 mg, 0.77mmol) was added into the solution which was stirred at 35 ^{o}C for 20 h. Then the solution was washed by HCl (20mL, 0.1M) twice and then by brine (20 mL), and

dried with sodium sulfate. After removing of solvent, white solid was obtained (3.5g, Y=80%). ^{1}H NMR (300 MHz, $CDCl_3$) δ (ppm): 3.62-3.37 (m, 26.6H), 2.08-2.01 (m,0.62H), 1.42 (H on Boc group, m,1H), 1.23 (m,1.5H), 1.12 (m,4.26H). To a DCM (20mL) solution of tBuDUPA-F127-DUPAtBu (3.3 g, 0.26 mmol) was added TFA (4mL). The solution was stirred at room temperature for 20 h. Then, DCM (20 mL) was added into the solution which was washed by DI water (20 mL) and brine (20 mL), and dried with sodium sulfate. After removing the solvent, white solid was obtained (3.1g, Y=93%). ^{1}H NMR (300 MHz, $CDCl_3$) δ (ppm): 3.62-3.37 (m, 1H), 2.08-2.01 (m,0.02H), 1.23 (m,0.06H), 1.12 (m,0.16H). According to the 1H NMR of the tBuDUPA-F127-DUPAtBu, we calculated 68.4% of surfactant polymer was added with DUPA.

Synthesis of BTII-DUPA SPN: A standard protocol has been developed to prepare SPNs through the nanoprecipitation method. Briefly, a 1 mL THF mixture of BTII (0.5 mg mL^{-1}) and surfactant F127/DUPA-F127-DUPA (20 mg mL^{-1}) was rapidly injected into deionized water (9 mL) under continuous sonication with a micro tip-equipped probe sonicator (Branson, W-150) at a power output of 4 watts RMS for 30 s. After sonication for additional 1 min, THF was removed by nitrogen bubbling. The aqueous solution was filtered through a polyethersulfone syringe driven filter (0.22 μm) and centrifuged three times using a 30 K centrifugal filter unit at 3,500 rpm for 30 min. The nanoparticle solution was finally concentrated to 1.0 mg mL^{-1} (based on the mass of BTII) by ultrafiltration and stored in dark at 4 °C.

Characterization: ^{1}H and ^{13}C NMR spectra were recorded on a Brucker ARX 400 at 293 K with deuterated chloroform as the solvent. DLS was performed using a Malvern Nano-zetasizer. UV/VIS/NIR spectra were recorded with Cary-5000. TEM imaging: For negative staining, 4-6 μL sample was applied to a continuous-carbon or Formvar-carbon coated grid, washed with water, and then stained using 1% uranyl acetate. Grids were imaged in a Philips CM12 transmission

electron microscope equipped with a LaB6 electron source, operated at 120 kV. Images were recorded at a magnification of 13,000 x on a TVIPS CCD camera with a pixel size of 24 um.

PA Spectroscopy: The OPO Laser (EKSPLA NT320) with pulse width 5 ns, repetition rate 10 Hz was applied as excitation laser resource. Nikon Eclipse TE2000-U inverted microscope with 10X objective was used to focus the light to the sample. The laser energy after a ND filter was 40-120 μJ. Single element transducer (v317-sm, 20 MHz) was used to acquire acoustic and photoacoustic signals. A preamplifier (Olympus 5682, voltage gain 30 dB) and a pulser/receiver (Olympus 5073 pr, ultrasonic bandwidth 75 MHz, voltage gain 39 dB) were used to improve the system sensitivity. All the samples were in the solution state and were sealed in 1 mm diameter glass tube. D_2O was applied as the sound coupling agent to avoid water absorption.

PA Tomography System: The ultrasound and photoacoustic signals were processed by a high-frequency ultrasound imaging system (Vantage128, Verasonics Inc.). An EKSPLA OPO Laser with pulse width 5 ns, repetition rate 10 Hz was applied as excitation laser for multispectral PA tomography. A Q-switched Nd:YAG laser (CFR ICE450, Quantel Laer) with 8 ns pulse with a 10 Hz repetition rate was applied as the excitation laser for other experiments. For the imaging depth study in chicken breast, a transmission-mode detection modality was adopted in imaging depth study in chicken breast. The laser light was guided to the tissue surface by a fiber bundle and the photoacoustic signals were detected from the other size of the tissue by a low-frequency transducer array (L7-4, PHILIPS/ATL). For other experiments, a refection-mode detection was applied with using a customized collinear probe, which has a customized high-frequency ultrasound array with 128 elements and 50% bandwidth (L22-14v, Verasonics Inc.).

TA Microscopy System: An 80MHz repetition rate femtosecond pulsed laser (Spectra Physics, InSight X3) provided two synchronized outputs: a fixed 1045 nm beam with ~200 fs pulse

width and a tunable beam ranging from 680 nm to 1300 nm with ~ 120 fs pulse width. In the TA microscopy system, the fixed 1045 nm beam served as pump source and the other beam served as probe beam was tuned to 853 nm. The resulted laser beating frequency (2154 cm^{-1}) is far away from the C-H region between 2800 – 3000 cm^{-1}, avoiding any signals from the biological systems. The pump beam was modulated at 2.3 MHz by an acousto-optic modulator (Isomet, 1205-C). Temporal delay between the pump and probe pulses was controlled by a motorized translation stage (Zaber, TLS28E), and collinearly combined and directed into a homebuilt laser-scanning microscope. Then, the pump and probe beams were focused on the sample by a 60x water immersion objective (NA = 1.2, UPlanApo/IR, Olympus), and the forward signals were collected by an oil condenser (NA = 1.4, U-AAC, Olympus). After passing an 850±120 nm filter, the 853 nm light was blocked and the TA signals (gain in the 1045 nm probe beam) were detected by a photodiode (Hamamatsu, S3994) incorporated with a home-built resonant circuit, which were demodulated by a phase-sensitive lock-in amplifier (Zurich Instruments). All images were acquired with 10 μs $pixel^{-1}$ dwell time. The probe (853 nm) and pump (1045 nm) powers before the microscope were maintained at 10 mW and 20 mW, respectively.

SRS Microscopy System: The setup of SRS microscope was similar to TA microscopy. In the SRS microscopy system, the 1045 nm laser served as the Stokes beam while the tunable laser was adjusted to 802 nm as the pump beam. The resulted laser beating frequency (2899 cm^{-1}) is within the C-H region between 2800 – 3000 cm^{-1}. The SRS signals (loss in the 1045 nm Stokes beam) was detected by the photodiode, which were demodulated with the digital lock-in amplifier (Zurich Instrument). All images were acquired with 10 μs/pixel dwell time. The pump (802 nm) and Stokes (1045 nm) powers before the microscope were maintained at 20 mW and 20 mW, respectively.

In Vitro TA Imaging of BTII-DUPA SPN: For cellular imaging, cells were treated with 13.3 μg mL^{-1} and incubated at 37 ^{o}C for different periods of time. Before the imaging, the cells were washed three times by fresh cell culture medium to remove extracellular and unbound nanoparticles.

Ex Vivo TA Imaging of BTII-DUPA SPN: Mice were euthanatized 72 h after intravenous injection of BTII-DUPA SPNs. Tumor tissues were immediately frozen in liquid nitrogen to preserve the tissue architecture. The frozen tissues were cut in pairs, that one slice in 100 μm for tissue imaging and the neighboring slice in 8-10 μm for H&E staining. The signals outside the region of interest in the large-area TA imaging of tissue slice were cropped.

Cell Culture: All the cell lines were purchased from American Type Culture Collection (ATCC). LNCaP cells were cultured in RPMI-1640 supplemented 10% fetal bovine serum (FBS). PC-3 cells were cultured in F-12K supplemented 10% fetal bovine serum (FBS). HFB cells were cultured in Dulbecco's Modified Eagle Medium (DMEM) supplemented 10% fetal bovine serum (FBS). The cells were maintained in in a humid environment containing 5% CO_2 and 95% air at 37 ^{o}C.

Cytotoxicity Test: LNCaP Cells were first seeded in 96-well plates (3000~5000 cells per well) for, and the culture medium was replaced with fresh medium containing polymer SPN at different concentrations (0-100 μg mL^{-1}) and incubated for 24 h. The cell viability was then measured by MTS Assay Kit (Abcam plc.).

Tumor Mouse Model: 4-6 weeks old male nude mice obtained from Charles River Laboratories were inoculated subcutaneously with $3x10^6$ PC-3 cells in the rear left flanks and $5x10^6$ LNCaP cells in the rear right flanks. Mice were used in imaging studies when either PC-3

or LNCaP tumors reached 8−10 mm in diameter. All protocols were approved by the Boston University Animal Care and Use Committee.

In Vivo PA Tomography Imaging of Tumor: Tumors-bearing mice were anesthetized using 2% isoflurane in oxygen delivered through a nose cone and their body temperature was maintained by a heat pad during the PA imaging period. PA images of PC-3 and LNCaP tumors on the same mouse before (pre) and 3 h, 6 h, 12 h, 24 h, 36 h, 48 h and 72 h after intravenous injection of 200 μL BTII-DUPA SPN (800 μg mL^{-1}) were collected, respectively. All animal experiments were performed in compliance with the Guidelines for the Care and Use of Research Animals established by the Boston University Animal Studies Committee.

Imaging Nanoparticle Solution in Matrigel In Vivo: Nanoparticles were suspended in 50% v/v Matrigel (BD Biosciences) to different concentrations. 50 μL PBS or nanoparticle Matrigel mixture was subcutaneously injected into the dorsal space of male nude mice (Charles River Laboratories), and PA imaging of the inclusions was performed with our PA tomography system at wavelengths from 1100 nm to 1300 nm in 20 nm interval. Then, concentration images of lipid, blood and BTII-DUPA SPN were generated from the multispectral images *via* LASSO analysis in Matlab.

LASSO Analysis: To perform chemical analysis, the hyperspectral image D (consisting of spectra from every pixel) should be decomposed into the linear combination of two smaller matrices C and S, corresponding to concentration maps of each component and the spectral profiles for each component. Once S is determined by measuring spectra from pure samples, we can obtain C through a least square fitting In our study, to further improve the robustness against noise and suppress cross-talks between different channels, we introduced a sparsity constraint, termed

LASSO (least absolute shrinkage and selection operator), to the original least square fitting problem, resulting in the following:

$$\hat{C} = \arg\min_{C}\{\frac{1}{2}(D - CS)^2 + \lambda|C|\}.$$

Solving the above equation yielded the concentration maps for all channels.

CHAPTER 4. PH-ACTIVATABLE PHOTOACOUSTIC IMAGING IN THE NIR-II WINDOW BY USING WATER-SOLUBLE SEMICONDUCTING POLYMER

The emerging second near-infrared (NIR-II: 1000-1700 nm) photoacoustic (PA) probes brighten the future of deep-tissue diagnosis and treatment. A number of efforts have been made to develop NIR-II absorbing semiconducting polymer nanoparticles and small molecules, but the chemical synthesis of them remains challenging and tedious. In this study, the potential of using chemical doping method to tune the absorption of semiconducting polymer from visible range into NIR-II range is investigated. The conjugated polymer (PE) is readily doped by oxygen in the environment, without using any toxic dopants. After doping, PE shows broad-band absorption in the entire NIR-II window, with great chemical stability, photostability and biocompatibility as well as promising PA imaging performance in the NIR-II window. Owing to its merit of broad-band absorption, the imaging depth comparison among different NIR-II wavelengths is achieved. Moreover, the doped PE is readily soluble in normal physiological pH (7-8) by virtue of carboxyl groups on side chains and tends to aggregate at an acidic environment which results in 7.6-fold PA enhancement at pH 5.0. Our study provides a more attainable yet effective platform to the field for achieving water-soluble NIR-II absorbing contrast agents for activatable PA imaging.

4.1 Introduction

The recent developments in the second near-infrared (NIR-II) window photoacoustic (PA) imaging has rapidly attracted extensive interest for both preclinical research and clinical practices.[18, 19, 119, 125, 170, 171] As compared with the first near-infrared (NIR-I) window, NIR-II window provide higher imaging quality and deeper imaging depth since the light scattering and tissue absorption are significantly reduced, and the maximum permissible exposure laser energy

for skin is increased in this window.[18, 19, 170] However, only few exogenous agents are currently available for NIR-II PA imaging, preventing the widespread application of this valued technique.[125]

Among the reported NIR-II PA agents, semiconducting polymer nanoparticles (SPNs) has been recognized as one of the most promising candidates, because of their high absorption coefficient, excellent photostability and outstanding biocompatibility.[44, 125] Most NIR-II semiconducting polymers were attained by narrowing down their bandgaps through donor-acceptor molecular engineering. Nevertheless, the chemical synthesis of those NIR-II semiconducting polymers remains challenging, which is complicated and tedious.[125, 171] Meanwhile, water-dispersed SPNs were mostly fabricated by nanoprecipitation approach, own to their hydrophobicity. Unfortunately, the encapsulated nanoparticles raise concerns in the leakage of polymers, the detachment of surfactants and the tendency to aggregate.[172] An alternative approach emerging recently is grafting hydrophilic poly(ethylene glycol) (PEG) onto the backbone of semiconducting polymers.[172, 173] However, the long PEG is prone to degrade under biological oxidative stress, and higher PEG grafting densities are likely to result in less cellular uptake.[174, 175] Therefore, a simple yet effective approach to prepare water-soluble NIR-II conjugated polymers is highly demanded to broaden the application of NIR-II PA imaging in biomedical research and application.

Besides the molecular structure, the absorption spectra of conjugated polymers is also known to be controlled by their redox states.[176] The redox reaction that converting conjugated polymer from the neutral state into polaron/bipolaron state is called doping, which is realized upon addition of chemical dopants (oxidizing/reducing agents) or application of an appropriate voltage. The new generated electronic levels of polaron/bipolarons are located between the conduction and valence bands of neutral conjugated polymers. As a result, the doped conjugated polymers have a

narrower band gap and corresponding changes in the absorption from visible to NIR ranges.[60] This doping method is typically developed for organic electronics and photovoltaic cell applications to induce desired structural, spectroscopic and electrical transport properties.[60] In the last decade, due to the unique NIR-absorbing property of conjugated polymers with the formation of polaron/biolarons, they have been applied for photoacoustic imaging and photothermal therapy in the NIR-I window.[117, 177-179] Most recently, doped ultrathin polypyrrole nanosheets with NIR-II absorption was reported as a promising photothermal therapy agent.[180] Regardless of numerous bio-applications have been achieved with several popular conjugated polymers (e.g. polypyrrole, poly(3,4-ethylenedioxythiophene):poly(4-styrenesulfonate), and polyaniline), a few long-standing intrinsic problems of conjugated polymers need to be appropriately addressed for NIR-II biological applications. First, these conjugated polymers must be doped by strong chemical dopants to obtain the NIR-II absorption, yet these dopants are susceptible to dissociation in bio-environments resulting in dedoping and losing of the signature optical property. In the meanwhile, the toxicity of the chemical dopants also needs to be taken into consideration. Last but not the least, the reported conjugated polymers are either toxic to cells or insoluble in solution, thus complicated surface modification is required.

Here we explore the scope and versatility of a water-soluble conjugated polymer for NIR-II PA imaging. We show that PE can be doped by atmospheric oxygen at physiological pH and remains stable for months, and it can respond to environment pH for targeted-tumor imaging.

4.2 Results and discussion

4.2.1 Synthesis and optical properties of conjugated polymers in doping process

The functionalized 3,4-ethylenedioxythiophene-alt-3,4-ethylenedioxythiophene copolymer bearing carboxylate side chains (PE) were prepared according to the reported standard

conditions (**Figure 4.1a**).[181, 182] Due to the strong ion-dipole interaction between carboxylates and water, PE were readily dissolved in KOH aqueous solutions without the addition of any stabilizer or surfactant.[182] More importantly, PE has the possibility of switching between its neutral form and the doped oxidized form (**Figure 4.1b**).[182]

The undoped PE displayed a vibrant blue color in the neutral state (**Figure 4.1c**). In order to be applicable in biology, appropriate amount of HCl was added to tune the solution pH to a physiological value of 7.5. Immediately, PE turned into purple with absorption increases in the NIR-II region (~ 1000 nm), which indicates that PE was spontaneously doped (oxidized) to polaron-state by oxygen in the neutral pH solution (**Figure 4.1c** and **4.1d**). For a longer exposure time (4 hours) in an ambient environment, PE was more doped to bipolaron-state leading to the solution color turned pale blue and the absorption further red-shifted towards far NIR-II region (> 1000 nm) (**Figure 4.1c** and **4.1d**). The overall absorption spectrum of PE is flatted from 1000 nm to 1700 nm, achieving a broad absorption in the entire NIR-II region (Figure 1d). While additional oxidizing agents such as $FeCl_3$ or Fe $(OTs)_3$ were commonly employed in the doping of conjugated polymers, here we demonstrated that PE can be directly doped by oxygen in the environment. This oxygen-doping method circumvents the purification and cytotoxicity problems of oxidants existing in previous studies.

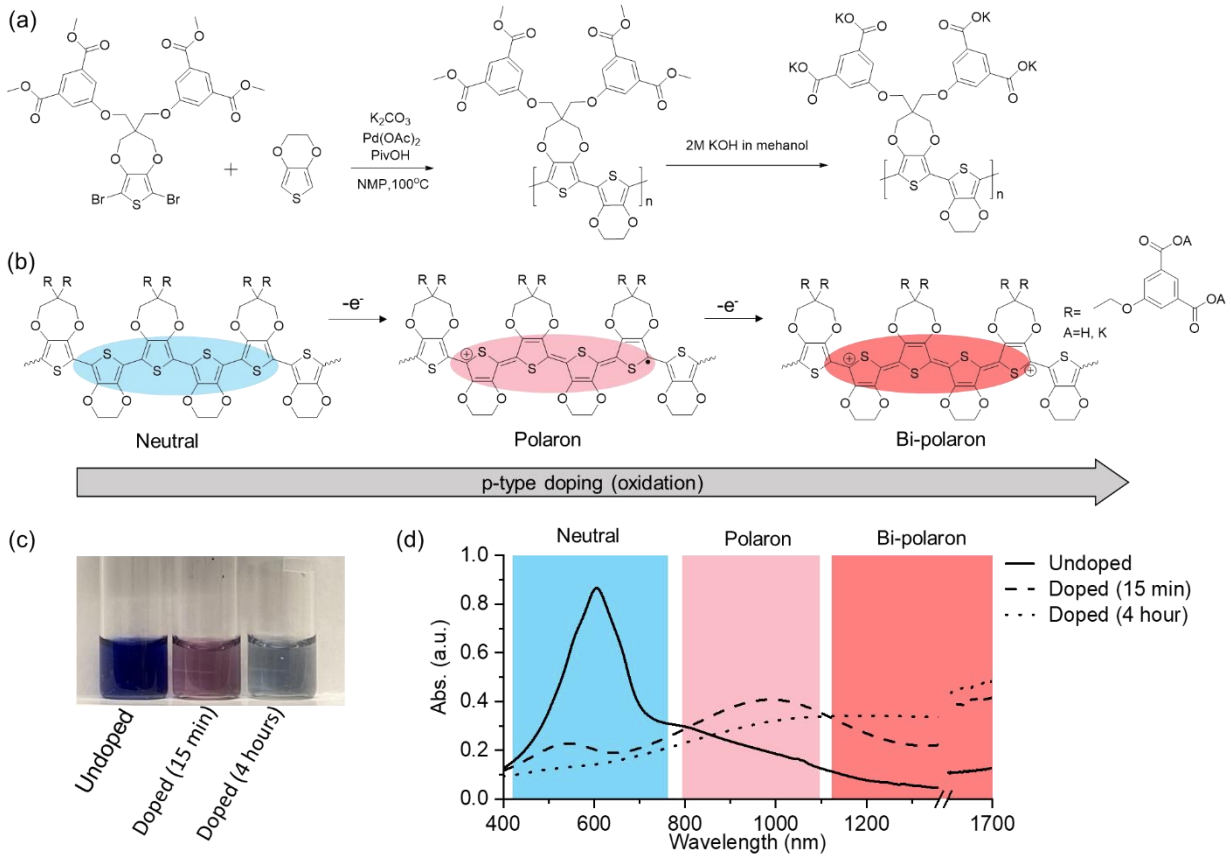

Figure 4.1 Design and mechanism of oxygen doped PE**.** a) Synthetic route of water-soluble PE. b) Mechanism of p-type doping. c) Photograph of PE aqueous solution when undoped (in neutral form, stabilized by N_2H_4), doped by the dissolved oxygen in the solution for 15 min (mostly in polaron state) and doped by the dissolved oxygen in the solution for 4 hours (mostly in polaron state). d) Absorption spectra of PE aqueous solution when undoped (in neutral form, stabilized by N_2H_4), doped by the dissolved oxygen in the solution for 15 min (mostly in polaron state) and doped by the dissolved oxygen in the solution for 4 hours (mostly in polaron state). The wavelength regions corresponding to neutral, polaron, and bipolaron state are highlighted in blue, pink and red, respectively.

4.2.2 Aqueous stability and cytotoxicity of PE after doping

To test the doping stability of PE in the physiological environments, we monitored the absorption spectrum of PE in PBS (pH 7.4) and in Minimum Essential Medium (MEM) cell culture medium (pH 7.4, 10% Fetal Bovine Serum) over time. **Figure 4.2a** shows that the absorption remained unchanged over 2 weeks. When the PE is dissolved in a cell culture medium, PE is less doped than that in PBS (pH 7.4) because of the existing of anti-oxidants (e.g. serum, glucose,

amino acids) in culture medium (**Figure 4.2b**).[183] The partially doped PE with a broad absorption peak at around 1000 nm remains stable for more than 2 weeks as well (Figure 4.2b). The excellent solubility and stability of PE after doping in PBS (pH 7.4) and in MEM indicates the feasibility of using doped PE for *in vivo* imaging in the NIR-II window. Besides, the cytotoxicity test was carried out with MTT assay to confirm the biocompatibility of doped PE (**Figure 4.2c**). No obvious toxicity was found up to 200 ug/ml after 24 hours incubation, showing the promise of the doped PE for biological applications.

In order to further understand the stability of the oxygen doping, the electrochemical properties of the PE were investigated by cyclic voltammetry (**Figure 4.2d**). The redox potential of PE was calculated to be -0.25 V vs. Ag/AgCl. Such negative value of the redox potential indicates the tendency of PE to lose electrons.[184] In addition, the energy associated with the excitation of the doping reaction can be calculated to be 0.65 for PE. [185] Thus, the low concentration of the oxygen dissolved in the solution can dope the PE to polaron or bipolaron states and maintain the stability.

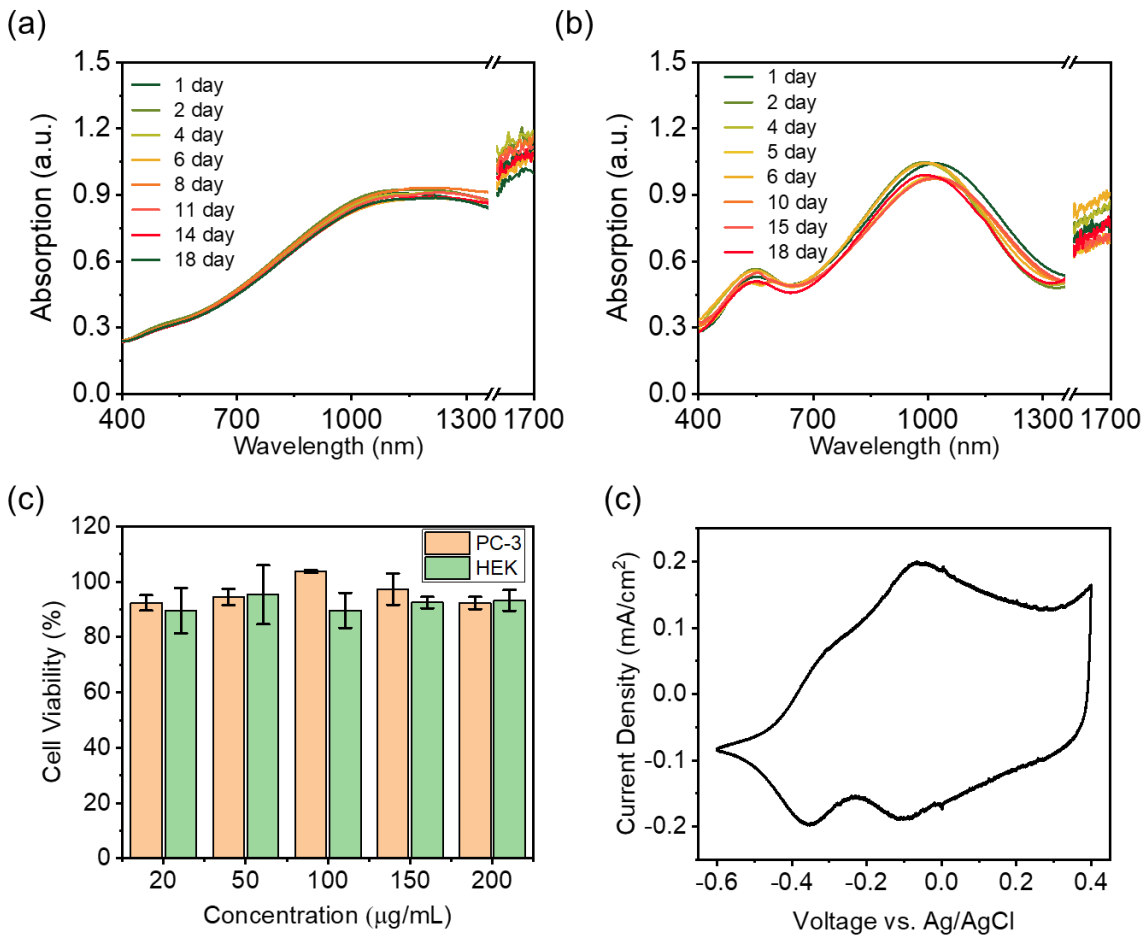

Figure 4.2 Aqueous stability and cytotoxicity of PE after doping. a) Absorption spectra of PE in PBS over time. b) Absorption spectra of PE in MEM cell culture medium (pH 7.4, 10% Fetal Bovine Serum) over time. c) Cell viability of PC-3 and HEK cells after 24-h incubation with PE solutions at various concentrations of PE. The percentage cell viability of treated cells is calculated relative to that of cells treated with the same volume of PBS (viability was arbitrarily defined as 100%). d) Cyclic voltammograms of the PE in Basal cell medium as biologically relevant electrolytes at a scan rate of 40 mV/s. Error bars represent for standard deviations.

4.2.3 **Photoacoustic properties of** PE

After the aqueous stability and biocompatibility of PE was confirmed, its potential for photoacoustic (PA) imaging was evaluated. **Figure 4.3a** and **4.3b** show that the doped PE efficiently generates PA signals in the entire NIR-II region in PBS and in MEM. No obvious PA intensity loss is observed after exposure to 3000 laser pulses at 1100 nm (corresponding to more than 5 minutes), suggesting the good photostability of doped PE (**Figure 4.3b**). Linear relationship

between the concentration and PA signal at 1100 nm is observed (**Figure 4.3c**). Under the same experimental condition, the detection sensitivity, defined as 1:1 signal-to background-ratio, is estimated to be 4.8 μg mL^{-1} and 3.6 μg mL^{-1} in PBS and MEM, respectively.

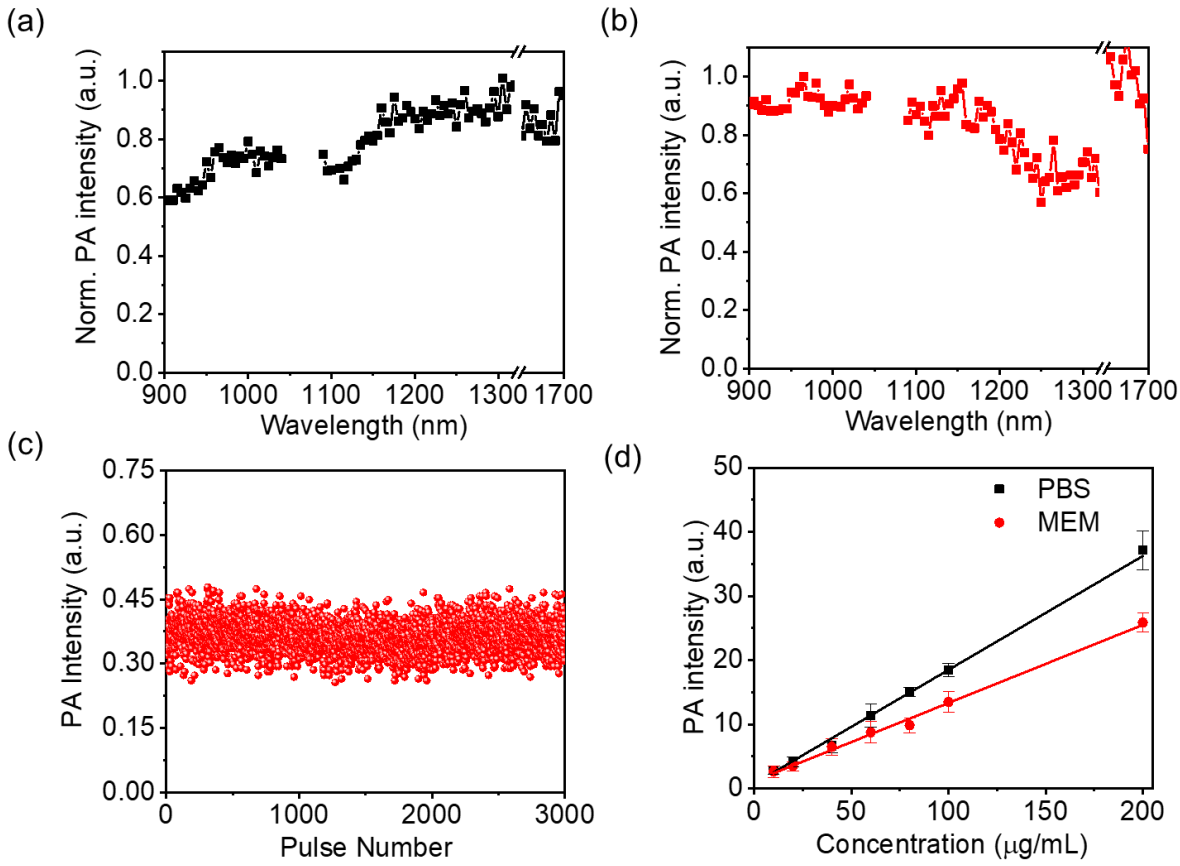

Figure 4.3 Photoacoustic properties of PE**.** PA spectra of PE in (a) PBS and (b) MEM cell culture medium (pH 7.4, 10% Fetal Bovine Serum). c) PA amplitudes of PE aqueous solution versus number of pulses under 1100 nm irradiation. The total exposure time is about 5 minutes for 3000 pulses. The laser light energy at the focus point is ~45 μJ. d) PA intensity of PE at 1100 nm as a function of mass concentration in PBS and in MEM cell culture medium (pH 7.4, 10% Fetal Bovine Serum). $R^2 > 0.99$. Error bars represent for standard deviations.

4.2.4 Deep-tissue imaging in the NIR-II window

Previously, we have demonstrated that NIR-II semiconducting polymer nanoparticles have the advantage of deeper imaging depth over NIR-I PA contrast agents. Therefore, it is worth testing if the water-soluble PE as a molecular contrast agent is also capable for deep-tissue imaging since

it can generate strong PA signal in the NIR-II window. PA imaging of doped PE was conducted with chicken breast tissue phantom a similar manner as our earlier study.[63] A polyurethane tube containing aqueous solution of doped PE was embedded in layers of chicken breast tissue with the same thickness below and above the tube, and a laser light at 1064 nm was illuminated from the top surface of the tissue while the PA signal was detected by a low-frequency ultrasound transducer array from the bottom surface of the tissue. The laser fluence is ~ 45 mJ/cm^2 and 100 images were acquired and averaged at the same position. An imaging depth of ~ 4.4 cm was obtained with the concentration of 0.5 mg/ml (**Figure 4.4a**), which is comparable to the imaging depth (~ 5 cm) that was achieved with NIR-II SPNs.[63, 123] The signal-to-noise ratio (SNR) of 0.5 mg/ml doped PE at ~ 4.4 cm is 56 and reaches 130 by increasing the concentration to 2.0 mg/ml. We also recorded PA images at different depths, and the derived SNR from the images was plotted as a function of depth and fitted into an exponential function (**Figure 4.4b**). The PA imaging depth limit with 0.5 mg/ml doped PE was determined to 4.9 cm by extending the fitted curve to where the SNR was equivalent to that of tissue background (SNR=20), while the optical penetration depth was also calculated to be 0.56 cm with an effective attenuation coefficient of 1.77 cm^{-1} from the fitted curve.[71] Thus, the PA imaging depth of PE at 1064 nm is 8.7 times higher than optical penetration depth in the current experimental conditions, which exhibits that PE as a water-soluble polymer is of great potential for deep-tissue imaging in the NIR-II window.

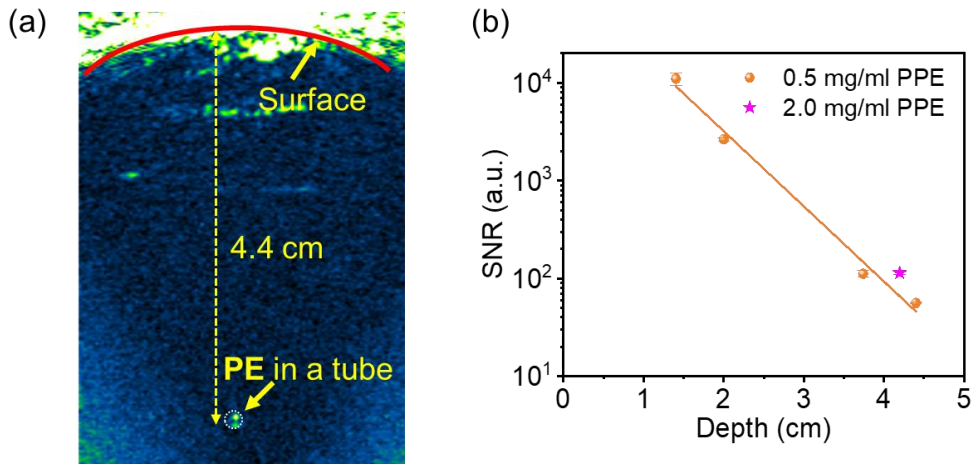

Figure 4.4 Deep-tissue imaging in the NIR-II window. (a) PA image of the 0.5 mg mL^{-1} PE contained in a polyurethane tube at 4.4 cm depth. Laser energy density was tuned to 45 mJ cm^{-2} at 1064 nm. (b) SNR of 0.5 mg mL^{-1} PE contained in a polyurethane tube as a function of depth from the illuminated tissue surface. Laser energy density was tuned to 45 mJ cm^{-2} at 1064 nm.

4.2.5 Imaging depth at different wavelengths in NIR-II window up to 1700 nm

Additionally, although the longer NIR-II wavelengths (beyond 1300 nm) have been highly appreciated in multi-photon imaging for providing a higher resolution and imaging depth due to the significantly reduced scattering at longer wavelengths,[186] the photoacoustic imaging performance at this region has been rarely explored owing to lack of suitable contrast agent and/or laser source. Therefore, it is exciting to use our doped PE that holds a flat PA spectrum in the entire NIR-II window to investigate the optimal wavelength in PA imaging by using our high-power OPO laser (EKSPLA NT320). 0.5 mg/ml fully doped PE was placed under 1.0 cm-thick chicken breast tissue, and the PA images were collected at different laser wavelengths ranging from 1100 nm to 1700 nm with the same laser energy (10 mJ/cm^2) (**Figure 4.5a)**. It is found that images corresponding to 1100 nm and 1300 nm exhibit detectable PA signals from the doped PE, and the high background signal at 1200 nm was mainly attributed to the lipid absorption at this wavelength. However, no PA signal was detected at 1400 nm, 1500 nm, 1600 nm or 1700 nm, suggesting they are not optimal wavelengths for deep-tissue PA imaging.

The observed results can be explained by the optical properties of tissue at different wavelengths. Theoretically, the imaging depth of PA tomography is limited by the penetration of diffused photons,[187] which can be described by the effective attenuation coefficient ($\sqrt{3\mu_a \times (\mu_a + (1-g)\mu_s)}$), where μ_a is absorption coefficient, μ_s is scattering coefficient and g is the anisotropy, which has a representative value of 0.9).[150] Accordingly, the absorption coefficient dominates the penetration depth in PA imaging whereas the scattering coefficient has a minor effect. Therefore, the 2.4-fold higher PA intensity at 1100 nm than that at 1300 nm can be explained by the lower water absorption at 1100 nm (**Figure 5b** and **5c**). Meanwhile, due to the strong absorption of water, blood and lipid at 1400-1700 nm,[13, 14, 188, 189] the PA imaging depth is not superior at this range (Figure 4e). We further calculated the effective attenuation coefficients for different human tissues and found that many of them show their local minima at ≈1100 nm (**Figure 5d**).[17]

These results combined with the previous study enable us to have a comprehensive understanding of optical wavelengths for PA imaging in the NIR-II window, that ≈1100 nm is preferred in terms of imaging depth, and ≈1300 nm benefits from lower background signal in tissue as the absorption of blood is at the local minimum.[19, 63, 189]

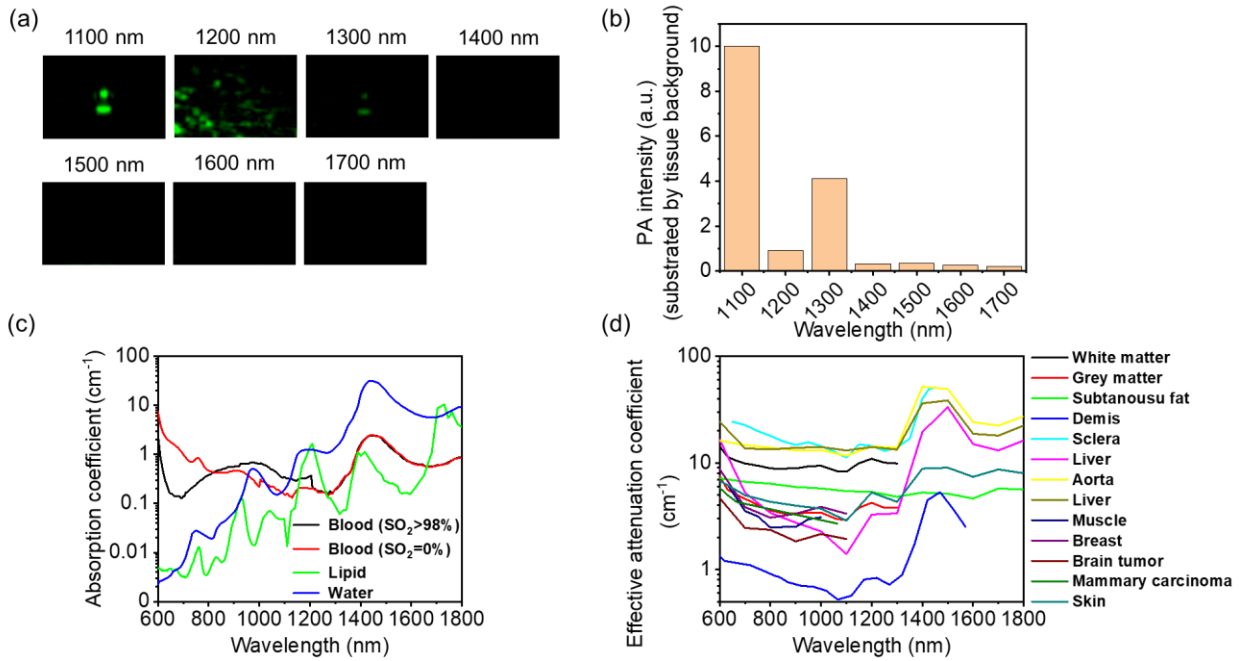

Figure 4.5 Imaging depth at different wavelengths in the NIR-II window. (a) PA images of 0.5 mg mL^{-1} PE contained in polyurethane tubes with a laser wavelength at 1100, 1200, 1400 nm, 1500nm, 1600 nm and 1700 nm, respectively. (b) PA intensities of 0.5 mg mL^{-1} PE at different wavelengths, which were extracted from the PA images in (a) and subtracted by the background signal of the nearby tissue. The laser energy density was tuned to 10 mJ cm^{-2} at each wavelength. (c) Absorption coefficient spectra of endogenous tissue chromophores.[13, 14, 188, 189] Adapted from Ref. [29-32]. (d) Calculated effective attenuation coefficients of human tissue.[17]

4.2.6 PE for pH-sensitive photoacoustic imaging

Besides the outstanding performance in deep-tissue photoacoustic imaging, doped conjugated polymer also has advantages in its functionality for activatable imaging. As an example, the responsivity of PE to pH is demonstrated. By introducing carboxylate ions to the side chains, PE is readily soluble in water under neutral or basic conditions. As the solution becomes more acidic, carboxylates convert into carboxylic acids resulting in the enhanced hydrophobicity of PE and thus it tends to aggregate into larger sizes. The effective diameter of PE was not detectable in those basic solutions, but it increases significantly when the pH is lower than 7.5 (**Figure 4.6a**). Meanwhile, the absorption spectra do not change (**Figure 4.6b**) in this physiological pH range, indicating PE reaches a stable doping state and the aggregation has negligible influence on the

optical absorption profiles. Then, the PA intensity of PE in the solutions with different pH were collected at 1064 nm and plotted. As seen in **Figure 4.6c,** The PA brightness of PE is enhanced by 7.5-fold from pH 7.5 to pH 5.5. Additionally, the PA intensity is proportional to the size of PE **(Figure 4.6d)**. Since we have ruled out the contribution of absorption change to the enhanced PA effect, such observation should be attributed to the increased localized heat flux with the growth of size. Indeed, the PA pressure is proportional to the heat transfer rate in theory,[6] and similar size-growth induced PA enhancements were observed for gold nanoparticles and polymer nanoparticles.[190-192] The unique pH-responsivity property of PE promises its application in the sensitive visualization of the acidic tumor microenvironment with enhanced PA signal.

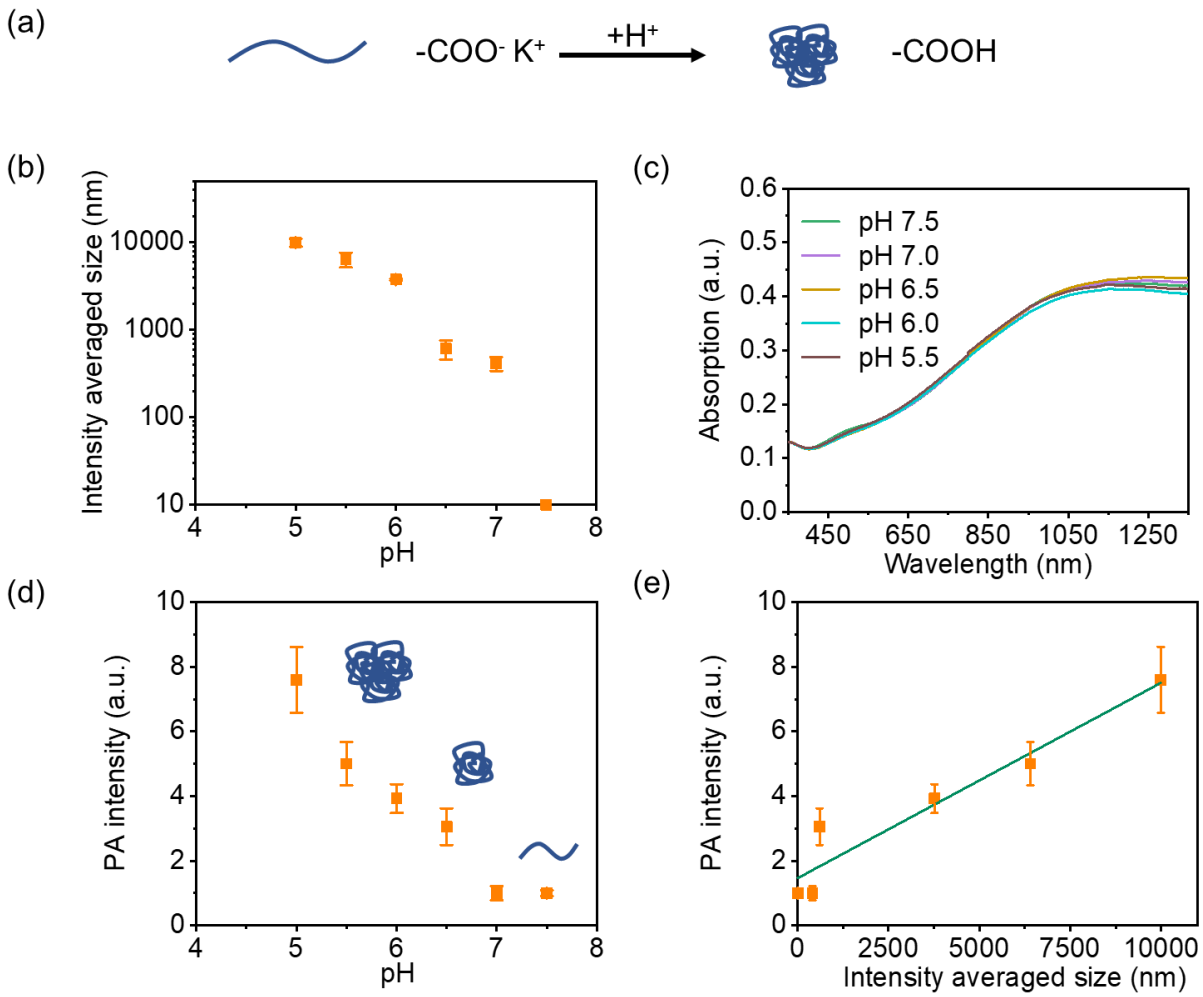

Figure 4.6 The size and PA response of PE towards pH. a) Illustration of the mechanism. b) Intensity averaged size of PE at different pH. c) Absorption spectra of PE at different pH. d) PA intensities at different pH. e) PA intensities as a function of intensity averaged size of PE. $R^2 > 0.9$. Error bars represent for standard deviations.

4.2.7 **In vivo pH imaging with** PE

Due to the glycolysis under hypoxic conditions, tumor microenvironment has been known as characteristically acidic.[193] Therefore, the pH - responsive PE is promising for visualization of tumor *in vivo*. As a proof-of-concept, *in vivo* PA imaging after local administration of PE (40 µL, 150 µg mL^{-1}) in muscle or tumor was carried out. **Figure 4.7a** shows that PE was obviously brighter in the tumor than that in the muscle, and the enhancement was quantified as high as 3.4±1.0-fold (**Figure 4.7b**). These results highlight the potential of PE for sensitive tumor imaging *in vivo*.

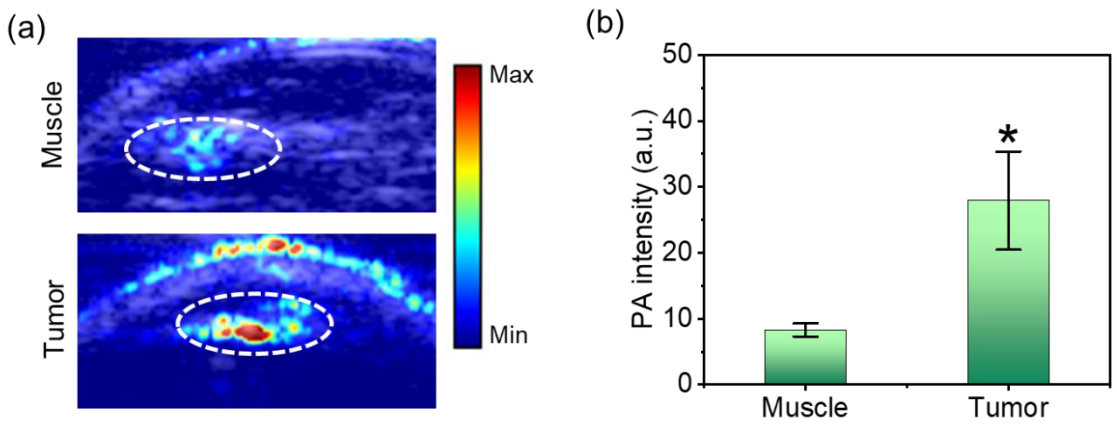

Figure 4.7 In vivo pH imaging with PE. a) PA images and b) quantification of PA signals in muscle and tumor after local administrations of PE (40 µL, 150 µg mL^{-1}). *Statistically significant difference in PA intensity between muscle and tumor *P<0.1 (n=3). Error bars represent standard error of mean.

4.3 Summary

In summary, we have reported a water soluble NIR-II contrast agent that is achieved by oxygen-doping approach. Taking advantages of the low oxidation potential, PE can be directly doped by oxygen in the environment and its absorption shifts to the NIR-II region (1000 – 1700 nm) after doping. The doped PE shows high stability in both PBS and cell culture medium for over time. The utility of doped PE for PA imaging is demonstrated, and by virtue of strong NIR-II absorption PE can provide an imaging depth as deep as 4.4 cm. The broad-band absorbing PE also enabled us to compare the imaging depth at different wavelengths (1100 nm – 1700 nm) in the NIR-II window by using chicken breast as the tissue phantom, and we found that 1100 nm is superior under our experimental conditions. This is mainly because the diffused photons could penetrate deeper at this wavelength according to the calculation of effective attenuation coefficients in tissue. Furthermore, the protonation of PE is capitalized to develop pH-responsive PA probe that tends to aggregate at more acidic pH and results in higher PA brightness as heat flux is enhanced. The pH-responsivity and amplified PA brightness of PE holds the promising future

for targeted-imaging of tumor microenvironment *in vivo*, and as well as other diseases associated with pH, such as inflammation, cardiac ischemia, and Alzheimer's disease.[194] Our study provides a new strategy on how to prepare NIR-II absorbing contrast agents with high water solubility. Besides, there are many other merits of such doped conjugated polymers that worth us to explore in our future study. For instance, utilization of the doped conjugated polymers for detection of redox species which play an essential role in the pathological and physically processes, since their doping-controlled absorption profiles are sensitive to the redox stress.

4.4 Experimental section

Chemicals and Polymer Synthesis: All reagents were purchased from Sigma-Aldrich and used without further purification unless otherwise noted. PE was synthesized according to the previous literature.[182]

Characterization: ^{1}H and ^{13}C NMR spectra were recorded on a Brucker ARX 400 at 293 K with deuterated chloroform as the solvent. Transmission electron microscopy (TEM) images were obtained on Tecnai T20. Dynamic light scattering (DLS) was performed using a Malvern Nano-zetasizer. UV/VIS/NIR spectra were recorded with Cary-5000.

Electrochemistry: A three-electrode cell was fabricated with ITO/glass substrates coated with PE as the working electrode, a leakless Ag/AgCl as the reference electrode, cell culture medium as the electrolyte, and a platinum wire as the counter electrode. Cyclic voltammetry experiments were performed using a three-electrode cell, at a scan rate of 40 mV s^{-1}. The redox potential of PE was estimated by $E_{1/2} = (E_{c,p}+E_{a,p})/2$: $E_{c,p}$-peak potential of the cathodic peak: $E_{a,p}$ -peak potential of the anodic peak.

Photoacoustic Spectroscopy: The complete description of the photoacoustic spectroscopy setup can be found in elsewhere.[92] The OPO Laser (EKSPLA NT320) with pulse width 5 ns,

repetition rate 10 Hz was applied as excitation laser resource. Nikon Eclipse TE2000-U inverted microscope with 10X objective was used to focus the light to the sample. The laser energy after ND filter was 40-120 μJ. Single element transducer (v317-sm, 20 MHz) was used to acquire acoustic and photoacoustic signals. A preamplifier (Olympus 5682, voltage gain 30 dB) and a Pulser/receiver (Olympus 5073 pr, ultrasonic bandwidth 75 MHz, voltage gain 39 dB) were used to improve the system sensitivity. All the samples were in the solution state and were sealed in 1 mm diameter glass tube. D_2O was applied as the sound coupling agent to avoid water absorption.

Photoacoustic Tomography: The ultrasound and photoacoustic signals were processed by a high-frequency ultrasound imaging system (Vantage128, Verasonics Inc.). For the penetration study in chicken breast, a Q-switched Nd:YAG laser (Continuum Surelite SL III-10) with 5 ns pulse with a 10 Hz repetition rate was applied as the laser source. A transmission-mode detection modality was adopted. The laser light was guided to the tissue surface by a fiber bundle and the photoacoustic signals were detected from the other side of the tissue by a low-frequency transducer array (L7-4, PHILIPS / ATL). For the other photoacoustic tomography experiments, the EKSPLA OPO Laser with pulse width 5 ns, repetition rate 10 Hz was applied as excitation laser. In the meantime, a refection-mode detection was applied with using a customized collinear probe, which has a customized high-frequency ultrasound array with 128 elements and 50% bandwidth (L22-14v, Verasonics Inc.).

Cytotoxicity Test: HEK cells were cultured in Dulbecco's Modified Eagle Medium (DMEM) containing 10% fetal bovine serum in a humid environment containing 5% CO_2 and 95% air at 37 ^oC. PC-3 cells were cultured in F-12K containing 10% fetal bovine serum in a humid environment containing 5% CO_2 and 95% air at 37 ^oC. Cells were first seeded in 96-well plates (3000~5000 cells per well), and the culture medium was replaced with fresh medium containing

PE at different concentrations (0-200 $\mu g \cdot mL^{-1}$) and incubated for 24 h. The cell viability was then measured by MTT assay.

Tumor Mouse Model: 4-6 weeks old male nude mice obtained from Charles River Laboratories were inoculated subcutaneously with $3x10^6$ PC-3 cells in the rear left flanks. Mice were used in imaging studies when either PC-3 tumors reached 8−10 mm in diameter. All protocols were approved by the Boston University Animal Care and Use Committee.

In vivo PA Tomography Imaging: Tumors-bearing mice were anesthetized using 2% isoflurane in oxygen delivered through a nose cone and their body temperature was maintained by a heat pad during the PA imaging period. All animal experiments were performed in compliance with the Guidelines for the Care and Use of Research Animals established by the Boston University Animal Studies Committee.

CHAPTER 5. CONCLUSIONS

In this dissertation work, the performance of PA imaging in the NIR-II window was extensively characterized by using semiconducting polymers as NIR-II contrast agents, and their potentials in biomedical applications (targeted cancer imaging) were explored. In the Chapter 2, NIR-II absorbing SPN was synthesized and its advantages in outstanding imaging contrast and deep imaging depth have been collectively demonstrated *in situ* and *in vivo*. Then in the Chapter 3, the potential application of NIR-II SPN for targeted prostate cancer imaging was further demonstrated, after functioning with DUPA. The targeting specificity has been validated *in vitro* and *in vivo.* Specifically, the investigation at single-cell level was achieved by using TA microscopy and the targeted prostate tumor imaging *in vivo* was achieved by using PA tomography. Besides the nanoparticles, water-soluble semiconducting polymer as PA contrast has also been developed by doping method, which also showed effective PA response in the NIR-II window. Meanwhile, it has sensitivity to pH and thus can be used for imaging of the acidic microenvironment in tumor. In conclusion, NIR-II PA imaging as a new molecular imaging modality provides new opportunities for disease diagnosis, drug design and therapy assessment, and we have showed strategies for how to synthesize semiconducting polymers as NIR-II contrast agents through molecular engineering and doping methods.

CHAPTER 6. OUTLOOK

1. Towards the clinical applications, the *in vivo* toxicity of the semiconducting polymer nanoparticles needs to be characterized more completely. Although, the cytotoxicity and H&E results are frequently shown in the literature. These results are still superficial and cannot fully convince the doctors in clinic.
2. Besides, one way to improve the biocompatibility is to develop biodegradable semiconducting polymer nanoparticles, so that the particles will not be trapped in the reticuloendothelial system.[174, 195, 196] The other ways are to use water-soluble doped conjugated polymer as we discussed in CHAPTER 4 or to incorporate long PEG chain to the conjugated polymer.[197] Yet, the knowledge of such types of conjugated polymers in terms of biocompatibility is also deficient.
3. Currently, there is no gold-standard guideline for how to optimize the photoacoustic efficacy of semiconducting polymer, other than improving the absorption coefficients. In the previous study of gold nanoparticles, it is believed that acoustic pressure waves generated by the particle itself is negligible. Instead, most of the heat is transferred to the surrounding medium and generating acoustic pressure waves.[198-200] However, it is not clear yet if it is the exact case for semiconducting polymer, since semiconducting polymer has very different physicochemical properties from gold. Therefore, more investigation in the mechanisms of PA generation through semiconducting polymer is needed.
4. In order to address the abovementioned question, it is demanding to develop advanced technology with high spatial and temporal resolutions, which is capable to precisely measure the heat, thermal expansion and acoustic waves from a single particle/molecule. At current, we usually measure the heat and acoustic waves of a bulk solution, which

contains the effects from both the agent and the solvent. As a result, it is difficult to extract the accurate information of the contrast agent alone for further analysis. In addition, the current mechanism studies are mainly based on the temperature-dependence and size-dependence experiments[199, 200], but they are all indirect measurements and may be affected by multiple factors. Therefore, single-particle/molecule-resolution measurement is critical to gain direct observations of the changes in a particle/molecule and in surrounding medium upon laser irradiation. By doing so, we could have a more solid and complete understanding of the mechanisms in PA generation through semiconducting polymer and provide strategies for how to design new materials with improved the PA efficacy.

5. Additionally, simulation software, like COMSOL, can be useful tools to help us to understand the mechanism by theoretical modeling.[201]

REFERENCES

[1] R. L. Siegel, K. D. Miller, A. Jemal, *CA: a cancer journal for clinicians* **2020**, *70*, 7.

[2] M. L. James, S. S. Gambhir, *Physiological reviews* **2012**, *92*, 897.

[3] T. F. Massoud, S. S. Gambhir, *Genes & development* **2003**, *17*, 545.

[4] X. Song, Q. Chen, Z. Liu, *Nano Research* **2014**, *8*, 340.

[5] Z. Sheng, B. Guo, D. Hu, S. Xu, W. Wu, W. H. Liew, K. Yao, J. Jiang, C. Liu, H. Zheng, B. Liu, *Advanced materials* **2018**, e1800766.

[6] L. V. Wang, *IEEE Journal of Selected Topics in Quantum Electronics* **2008**, *14*, 171.

[7] L. V. Wang, J. Yao, *Nature methods* **2016**, *13*, 627.

[8] L. V. Wang, S. Hu, *Science* **2012**, *335*, 1458.

[9] P. K. Upputuri, M. Pramanik, *Journal of biomedical optics* **2019**, *24*, 1.

[10] L. Lin, P. Hu, J. Shi, C. M. Appleton, K. Maslov, L. Li, R. Zhang, L. V. Wang, *Nature communications* **2018**, *9*, 2352.

[11] Y. Zhou, D. Wang, Y. Zhang, U. Chitgupi, J. Geng, Y. Wang, Y. Zhang, T. R. Cook, J. Xia, J. F. Lovell, *Theranostics* **2016**, *6*, 688.

[12] K. Welsher, Z. Liu, S. P. Sherlock, J. T. Robinson, Z. Chen, D. Daranciang, H. Dai, *Nature nanotechnology* **2009**, *4*, 773.

[13] R. L. van Veen, H. Sterenborg, A. Pifferi, A. Torricelli, R. Cubeddu, "Determination of VIS-NIR absorption coefficients of mammalian fat, with time-and spatially resolved diffuse reflectance and transmission spectroscopy", presented at *Biomedical Topical Meeting*, 2004.

[14] G. M. Hale, M. R. Querry, *Applied optics* **1973**, *12*, 555.

[15] S. Prahl, *http://omlc.ogi.edu/spectra/hemoglobin/index.html* **1998**.

[16] K. Welsher, S. P. Sherlock, H. Dai, *Proceedings of the National Academy of Sciences of the United States of America* **2011**, *108*, 8943.

[17] A. N. Bashkatov, E. A. Genina, V. V. Tuchin, in *Handbook of biomedical optics*, CRC Press, 2016, 87.

[18] G. Hong, A. L. Antaris, H. Dai, *Nature biomedical engineering* **2017**, *1*.

[19] A. M. Smith, M. C. Mancini, S. Nie, *Nature nanotechnology* **2009**, *4*, 710.

[20] S. Mallidi, G. P. Luke, S. Emelianov, *Trends in biotechnology* **2011**, *29*, 213.

[21] P. Wang, H. W. Wang, M. Sturek, J. X. Cheng, *Journal of biophotonics* **2012**, *5*, 25.

[22] H.-W. Wang, N. Chai, P. Wang, S. Hu, W. Dou, D. Umulis, L. V. Wang, M. Sturek, R. Lucht, J.-X. Cheng, *Physical review letters* **2011**, *106*, 238106.

[23] B. Wang, A. Karpiouk, D. Yeager, J. Amirian, S. Litovsky, R. Smalling, S. Emelianov, *Ultrasound in medicine & biology* **2012**, *38*, 2098.

[24] Y. Cao, J. Hui, A. Kole, P. Wang, Q. Yu, W. Chen, M. Sturek, J.-X. Cheng, *Scientific reports* **2016**, *6*, 1.

[25] K. Jansen, A. F. Van Der Steen, H. M. van Beusekom, J. W. Oosterhuis, G. van Soest, *Optics letters* **2011**, *36*, 597.

[26] R. Li, M. N. Slipchenko, P. Wang, J.-X. Cheng, *Journal of biomedical optics* **2013**, *18*, 040502.

[27] R. Li, L. Lan, Y. Xia, P. Wang, L. K. Han, G. L. Dunnington, S. Obeng-Gyasi, G. E. Sandusky, J. A. Medley, S. T. Crook, *Medical devices & sensors* **2018**, *1*, e10018.

[28] A. Oraevsky, E. Savateeva, S. Solomatin, A. Karabutov, V. Andreev, Z. Gatalica, T. Khamapirad, P. Henrichs, *Optoacoustic imaging of blood for visualization and diagnostics of breast cancer*, Vol. 4618, SPIE, 2002.

[29] J. R. Rajian, G. Girish, X. Wang, *Journal of biomedical optics* **2012**, *17*, 096013.

[30] R. Siphanto, K. Thumma, R. Kolkman, T. Van Leeuwen, F. De Mul, J. Van Neck, L. Van Adrichem, W. Steenbergen, *Optics express* **2005**, *13*, 89.

[31] L. Li, L. Zhu, C. Ma, L. Lin, J. Yao, L. Wang, K. Maslov, R. Zhang, W. Chen, J. Shi, *Nature biomedical engineering* **2017**, *1*, 1.

[32] H.-P. F. Brecht, R. Su, M. P. Fronheiser, S. A. Ermilov, A. Conjusteau, A. A. Oraevsky, *Journal of biomedical optics* **2009**, *14*, 064007.

[33] Y. Wang, K. I. Maslov, Y. Zhang, S. Hu, L.-M. Yang, Y. Xia, J. Liu, L. V. Wang, *Journal of biomedical optics* **2011**, *16*, 011014.

[34] L. Wang, J. Yao, R. Zhang, S. Xu, G. Li, J. Zou, L. V. Wang, "Photoacoustic imaging of single circulating melanoma cells in vivo", presented at *Photons Plus Ultrasound: Imaging and Sensing 2015*, 2015.

[35] G. P. Luke, D. Yeager, S. Y. Emelianov, *Annals of biomedical engineering* **2012**, *40*, 422.

[36] J. Weber, P. C. Beard, S. E. Bohndiek, *Nature methods* **2016**, *13*, 639.

[37] L. Nie, X. Chen, *Chemical Society reviews* **2014**, *43*, 7132.

[38] B. Kang, D. Yu, Y. Dai, S. Chang, D. Chen, Y. Ding, *Small* **2009**, *5*, 1292.

[39] M. Pramanik, M. Swierczewska, D. Green, B. Sitharaman, L. V. Wang, *Journal of biomedical optics* **2009**, *14*, 034018.

[40] G. P. Luke, A. Bashyam, K. A. Homan, S. Makhija, Y.-S. Chen, S. Y. Emelianov, *Nanotechnology* **2013**, *24*, 455101.

[41] Y.-S. Chen, K. Homan, D. Xu, W. Frey, S. Emelianov, "Feasibility of contrast-enhanced photoacoustic liver imaging at a wavelength of 1064 nm", presented at *Biomedical Optics*, 2012.

[42] W. Li, X. Chen, *Nanomedicine* **2015**, *10*, 299.

[43] Y. S. Chen, Y. Zhao, S. J. Yoon, S. S. Gambhir, S. Emelianov, *Nature nanotechnology* **2019**, *14*, 465.

[44] K. Pu, A. J. Shuhendler, J. V. Jokerst, J. Mei, S. S. Gambhir, Z. Bao, J. Rao, *Nature nanotechnology* **2014**, *9*, 233.

[45] K. Pu, J. Mei, J. V. Jokerst, G. Hong, A. L. Antaris, N. Chattopadhyay, A. J. Shuhendler, T. Kurosawa, Y. Zhou, S. S. Gambhir, Z. Bao, J. Rao, *Advanced materials* **2015**, *27*, 5184.

[46] K. Pu, A. J. Shuhendler, J. V. Jokerst, J. Mei, S. S. Gambhir, Z. Bao, J. Rao, *Nat Nanotechnol* **2014**, *9*, 233.

[47] K. Pu, A. J. Shuhendler, J. Rao, *Angewandte Chemie* **2013**, *52*, 10325.

[48] J. Zhang, X. Zhen, P. K. Upputuri, M. Pramanik, P. Chen, K. Pu, *Adv Mater* **2017**, *29*.

[49] Q. Miao, Y. Lyu, D. Ding, K. Pu, *Advanced materials* **2016**, *28*, 3662.

[50] J. Gierschner, J. Cornil, H. J. Egelhaaf, *Advanced materials* **2007**, *19*, 173.

[51] A. Banerji, A.-K. Sch?nbein, L. Halbr¨¹gge, *World Journal of Chemical Education* **2018**, *6*, 54.

[52] G. Li, W.-H. Chang, Y. Yang, *Nature Reviews Materials* **2017**, *2*.

[53] A. Ajayaghosh, *Chemical Society reviews* **2003**, *32*, 181.

[54] T. Hasegawa, M. Ashizawa, J. Hiyoshi, S. Kawauchi, J. Mei, Z. Bao, H. Matsumoto, *Polymer Chemistry* **2016**, *7*, 1181.

[55] K. Mullen, W. Pisula, *Journal of the American Chemical Society* **2015**, *137*, 9503.

[56] L. Lu, T. Zheng, Q. Wu, A. M. Schneider, D. Zhao, L. Yu, *Chemical reviews* **2015**, *115*, 12666.

[57] M. S. Vezie, S. Few, I. Meager, G. Pieridou, B. Dorling, R. S. Ashraf, A. R. Goni, H. Bronstein, I. McCulloch, S. C. Hayes, M. Campoy-Quiles, J. Nelson, *Nature materials* **2016**, *15*, 746.

[58] J. Zhang, C. Yang, R. Zhang, R. Chen, Z. Zhang, W. Zhang, S. H. Peng, X. Chen, G. Liu, C. S. Hsu, C. S. Lee, *Advanced functional materials* **2017**, *27*.

[59] D. Li, G. Zhang, W. Xu, J. Wang, Y. Wang, L. Qiu, J. Ding, X. Yang, *Theranostics* **2017**, *7*, 4029.

[60] J. L. Bredas, G. B. Street, *Accounts of chemical research* **1985**, *18*, 309.

[61] Y. Li, **2015**, *91*, 23.

[62] P. Camurlu, *RSC Adv.* **2014**, *4*, 55832.

[63] J. Wu, L. You, L. Lan, H. J. Lee, S. T. Chaudhry, R. Li, J. X. Cheng, J. Mei, *Advanced materials* **2017**, *29*.

[64] R. G. Aswathy, Y. Yoshida, T. Maekawa, D. S. Kumar, *Anal Bioanal Chem* **2010**, *397*, 1417.

[65] G. S. Filonov, A. Krumholz, J. Xia, J. Yao, L. V. Wang, V. V. Verkhusha, *Angew Chem Int Ed Engl* **2012**, *51*, 1448.

[66] F. Helmchen, W. Denk, *Nat Methods* **2005**, *2*, 932.

[67] L. V. Wang, *Nature photonics* **2009**, *3*, 503.

[68] J. Hui, R. Li, E. H. Phillips, C. J. Goergen, M. Sturek, J. X. Cheng, *Photoacoustics* **2016**, *4*, 11.

[69] M. Xu, L. V. Wang, *Review of Scientific Instruments* **2006**, *77*, 041101.

[70] Y. Sheng, L. D. Liao, N. Thakor, M. C. Tan, *Scientific reports* **2014**, *4*, 6562.

[71] G. Ku, M. Zhou, S. Song, Q. Huang, J. Hazle, C. Li, *ACS nano* **2012**, *6*, 7489.

[72] A. Taruttis, E. Herzog, D. Razansky, V. Ntziachristos, *Opt Express* **2010**, *18*, 19592.

[73] K. Homan, S. Kim, Y. S. Chen, B. Wang, S. Mallidi, S. Emelianov, *Opt Lett* **2010**, *35*, 2663.

[74] L. A. Sordillo, Y. Pu, S. Pratavieira, Y. Budansky, R. R. Alfano, *Journal of biomedical optics* **2014**, *19*, 056004.

[75] K. Pu, N. Chattopadhyay, J. Rao, *Journal of controlled release : official journal of the Controlled Release Society* **2016**, *240*, 312.

[76] Y. Jiang, K. Pu, *Small* **2017**.

[77] Y. Jiang, P. K. Upputuri, C. Xie, Y. Lyu, L. Zhang, Q. Xiong, M. Pramanik, K. Pu, *Nano letters* **2017**.

[78] Y. Koizumi, M. Ide, A. Saeki, C. Vijayakumar, B. Balan, M. Kawamoto, S. Seki, *Polymer Chemistry* **2013**, *4*, 484.

[79] T. Hasegawa, M. Ashizawa, J. Hiyoshi, S. Kawauchi, J. Mei, Z. Bao, H. Matsumoto, *Polym. Chem.* **2016**, *7*, 1181.

[80] G. Ferrauto, F. Carniato, E. Di Gregorio, L. Tei, M. Botta, S. Aime, *Nanoscale* **2017**, *9*, 99.

[81] Y. Cai, P. Liang, Q. Tang, X. Yang, W. Si, W. Huang, Q. Zhang, X. Dong, *ACS Nano* **2017**.

[82] M. Landsman, G. Kwant, G. Mook, W. Zijlstra, *Journal of applied physiology* **1976**, *40*, 575.

[83] F. Danhier, O. Feron, V. Preat, *Journal of controlled release : official journal of the Controlled Release Society* **2010**, *148*, 135.

[84] V. Torchilin, *Adv Drug Deliv Rev* **2011**, *63*, 131.

[85] B. C. Wilson, S. L. Jacques, *IEEE Journal of Quantum Electronics* **1990**, *26*, 2186.

[86] L. Wang, S. L. Jacques, *Journal of the Optical Society of America A* **1993**, *10*, 1746.

[87] G. M. El Maghraby, B. W. Barry, A. C. Williams, *european journal of pharmaceutical sciences* **2008**, *34*, 203.

[88] R. C. Wester, H. I. Maibach, *Journal of Toxicology: Cutaneous and Ocular Toxicology* **2001**, *20*, 411.

[89] J. Folkman, *New england journal of medicine* **1971**, *285*, 1182.

[90] J. Folkman, *CancerSpectrum Knowledge Environment* **1990**, *82*, 4.

[91] A. De la Zerda, C. Zavaleta, S. Keren, S. Vaithilingam, S. Bodapati, Z. Liu, J. Levi, B. R. Smith, T. J. Ma, O. Oralkan, Z. Cheng, X. Chen, H. Dai, B. T. Khuri-Yakub, S. S. Gambhir, *Nat Nanotechnol* **2008**, *3*, 557.

[92] H. W. Wang, N. Chai, P. Wang, S. Hu, W. Dou, D. Umulis, L. V. Wang, M. Sturek, R. Lucht, J. X. Cheng, *Phys Rev Lett* **2011**, *106*, 238106.

[93] J. Pavese, I. M. Ogden, R. C. Bergan, *JoVE (Journal of Visualized Experiments)* **2013**, e50873.

[94] S. I. Park, S. J. Kim, L. K. McCauley, G. E. Gallick, *Current Protocols in Pharmacology* **2010**, 14.15. 1.

[95] R. L. Siegel, K. D. Miller, A. Jemal, *CA: a cancer journal for clinicians* **2019**, *69*, 7.

[96] W. R. Farwell, J. A. Linder, A. K. Jha, *Arch Intern Med* **2007**, *167*, 2497.

[97] K. Lin, R. Lipsitz, T. Miller, S. Janakiraman, *Ann Intern Med* **2008**, *149*, 192.

[98] F. Algaba, **2018**, 47.

[99] G. L. Andriole, *Nature Reviews Urology* **2009**, *6*, 188.

[100] I. G. Schoots, M. J. Roobol, D. Nieboer, C. H. Bangma, E. W. Steyerberg, M. M. Hunink, *European urology* **2015**, *68*, 438.

[101] V. Scattoni, A. Zlotta, R. Montironi, C. Schulman, P. Rigatti, F. Montorsi, *European urology* **2007**, *52*, 1309.

[102] S. C. Berngard, K. O. Rove, J. Rassweiler, O. Kalthoff, M. Hruz, E. D. Crawford, **2013**, 103.

[103] D. Fehr, H. Veeraraghavan, A. Wibmer, T. Gondo, K. Matsumoto, H. A. Vargas, E. Sala, H. Hricak, J. O. Deasy, *Proceedings of the National Academy of Sciences* **2015**, *112*, E6265.

[104] M. Kongnyuy, A. K. George, A. R. Rastinehad, P. A. Pinto, *Current urology reports* **2016**, *17*, 32.

[105] C. Li, L. V. Wang, *Physics in medicine and biology* **2009**, *54*, R59.

[106] L. V. Wang, L. Gao, *Annual review of biomedical engineering* **2014**, *16*, 155.

[107] X. Wang, W. W. Roberts, P. L. Carson, D. P. Wood, J. B. Fowlkes, *Biomedical optics express* **2010**, *1*, 1117.

[108] K. S. Valluru, J. K. Willmann, *Ultrasonography* **2016**, *35*, 267.

[109] A. Horiguchi, M. Shinchi, A. Nakamura, T. Wada, K. Ito, T. Asano, H. Shinmoto, H. Tsuda, M. Ishihara, *Urology* **2017**, *108*, 212.

[110] G. Russo, M. Mischi, W. Scheepens, J. J. De la Rosette, H. Wijkstra, *BJU international* **2012**, *110*, E794.

[111] L. Fass, *Molecular oncology* **2008**, *2*, 115.

[112] S. Lee, J. Xie, X. Chen, *Biochemistry* **2010**, *49*, 1364.

[113] K. Strebhardt, A. Ullrich, *Nature Reviews Cancer* **2008**, *8*, 473.

[114] A. Agarwal, S. W. Huang, M. O'Donnell, K. C. Day, M. Day, N. Kotov, S. Ashkenazi, *Journal of Applied Physics* **2007**, *102*, 064701.

[115] V. Dogra, B. Chinni, S. Singh, H. Schmitthenner, N. Rao, J. J. Krolewski, K. L. Nastiuk, *Journal of biomedical optics* **2016**, *21*, 66019.

[116] H. K. Zhang, Y. Chen, J. Kang, A. Lisok, I. Minn, M. G. Pomper, E. M. Boctor, *Journal of biophotonics* **2018**, *11*, e201800021.

[117] J. Li, S. J. Yoon, B. Y. Hsieh, W. Tai, M. O'Donnell, X. Gao, *Nano letters* **2015**, *15*, 8217.

[118] G. Xu, M. Qin, A. Mukundan, J. Siddiqui, M. Takada, P. Vilar-Saavedra, S. A. Tomlins, R. Kopelman, X. Wang, *Proceedings of SPIE--the International Society for Optical Engineering* **2016**, *9708*.

[119] G. Hong, S. Diao, J. Chang, A. L. Antaris, C. Chen, B. Zhang, S. Zhao, D. N. Atochin, P. L. Huang, K. I. Andreasson, *Nature photonics* **2014**, *8*, 723.

[120] F. Wang, H. Wan, Z. Ma, Y. Zhong, Q. Sun, Y. Tian, L. Qu, H. Du, M. Zhang, L. Li, H. Ma, J. Luo, Y. Liang, W. J. Li, G. Hong, L. Liu, H. Dai, *Nature methods* **2019**, *16*, 545.

[121] H. Liu, G. Hong, Z. Luo, J. Chen, J. Chang, M. Gong, H. He, J. Yang, X. Yuan, L. Li, X. Mu, J. Wang, W. Mi, J. Luo, J. Xie, X. D. Zhang, *Advanced materials* **2019**, *31*, e1901015.

[122] J. Wu, L. You, L. Lan, H. J. Lee, S. T. Chaudhry, R. Li, J. X. Cheng, J. Mei, *Advanced materials* **2017**, *29*.

[123] Y. Jiang, P. K. Upputuri, C. Xie, Y. Lyu, L. Zhang, Q. Xiong, M. Pramanik, K. Pu, *Nano letters* **2017**, *17*, 4964.

[124] B. Guo, Z. Sheng, K. Kenry, D. Hu, X. Lin, S. Xu, C. Liu, H. Zheng, B. Liu, *Mater. Horiz.* **2017**, *4*, 1151.

[125] Q. Miao, K. Pu, *Advanced materials* **2018**, *30*, e1801778.

[126] D. Peer, J. M. Karp, S. Hong, O. C. Farokhzad, R. Margalit, R. Langer, *Nature nanotechnology* **2007**, *2*, 751.

[127] G. L. Wright Jr, C. Haley, M. L. Beckett, P. F. Schellhammer, "Expression of prostate-specific membrane antigen in normal, benign, and malignant prostate tissues", presented at *Urologic Oncology: Seminars and Original Investigations*, 1995.

[128] D. A. Silver, I. Pellicer, W. R. Fair, W. Heston, C. Cordon-Cardo, *Clinical cancer research* **1997**, *3*, 81.

[129] A. Ghosh, W. D. Heston, *Journal of cellular biochemistry* **2004**, *91*, 528.

[130] A. Barve, W. Jin, K. Cheng, *Journal of controlled release : official journal of the Controlled Release Society* **2014**, *187*, 118.

[131] D. G. Bostwick, A. Pacelli, M. Blute, P. Roche, G. P. Murphy, *Cancer: Interdisciplinary International Journal of the American Cancer Society* **1998**, *82*, 2256.

[132] S. A. Kularatne, K. Wang, H. K. Santhapuram, P. S. Low, *Molecular pharmaceutics* **2009**, *6*, 780.

[133] Y. Chen, S. Dhara, S. R. Banerjee, Y. Byun, M. Pullambhatla, R. C. Mease, M. G. Pomper, *Biochemical and biophysical research communications* **2009**, *390*, 624.

[134] T. Liu, L. Y. Wu, M. R. Hopkins, J. K. Choi, C. E. Berkman, *Bioorganic & medicinal chemistry letters* **2010**, *20*, 7124.

[135] Y. Chen, M. Pullambhatla, S. R. Banerjee, Y. Byun, M. Stathis, C. Rojas, B. S. Slusher, R. C. Mease, M. G. Pomper, *Bioconjugate chemistry* **2012**, *23*, 2377.

[136] A. Afshar-Oromieh, E. Avtzi, F. L. Giesel, T. Holland-Letz, H. G. Linhart, M. Eder, M. Eisenhut, S. Boxler, B. A. Hadaschik, C. Kratochwil, W. Weichert, K. Kopka, J. Debus, U. Haberkorn, *European journal of nuclear medicine and molecular imaging* **2015**, *42*, 197.

[137] L. E. Kelderhouse, V. Chelvam, C. Wayua, S. Mahalingam, S. Poh, S. A. Kularatne, P. S. Low, *Bioconjugate chemistry* **2013**, *24*, 1075.

[138] S. A. Kularatne, M. Thomas, C. H. Myers, P. Gagare, A. K. Kanduluru, C. J. Crian, B. N. Cichocki, *Clinical cancer research : an official journal of the American Association for Cancer Research* **2019**, *25*, 177.

[139] X. Luo, D. T. Tran, H. Sun, T. Mi, N. M. Kadlubowski, Y. Zhao, K. Zhao, J. Mei, *Asian Journal of Organic Chemistry* **2018**, *7*, 2248.

[140] K. P. Maresca, S. M. Hillier, F. J. Femia, D. Keith, C. Barone, J. L. Joyal, C. N. Zimmerman, A. P. Kozikowski, J. A. Barrett, W. C. Eckelman, J. W. Babich, *Journal of medicinal chemistry* **2009**, *52*, 347.

[141] C. Xie, P. K. Upputuri, X. Zhen, M. Pramanik, K. Pu, *Biomaterials* **2017**, *119*, 1.

[142] H. Yamakoshi, K. Dodo, M. Okada, J. Ando, A. Palonpon, K. Fujita, S. Kawata, M. Sodeoka, *Journal of the American Chemical Society* **2011**, *133*, 6102.

[143] H. J. Lee, W. Zhang, D. Zhang, Y. Yang, B. Liu, E. L. Barker, K. K. Buhman, L. V. Slipchenko, M. Dai, J. X. Cheng, *Scientific reports* **2015**, *5*, 7930.

[144] L. Wei, F. Hu, Y. Shen, Z. Chen, Y. Yu, C. C. Lin, M. C. Wang, W. Min, *Nature methods* **2014**, *11*, 410.

[145] Y. Jung, M. N. Slipchenko, C. H. Liu, A. E. Ribbe, Z. Zhong, C. Yang, J. X. Cheng, *Physical review letters* **2010**, *105*, 217401.

[146] S. Chong, W. Min, X. S. Xie, *The journal of physical chemistry letters* **2010**, *1*, 3316.

[147] Y. Cao, J.-H. Dou, N.-j. Zhao, S. Zhang, Y.-Q. Zheng, J.-P. Zhang, J.-Y. Wang, J. Pei, Y. Wang, *Chemistry of Materials* **2016**, *29*, 718.

[148] S. D. Dimitrov, B. C. Schroeder, C. B. Nielsen, H. Bronstein, Z. Fei, I. McCulloch, M. Heeney, J. R. Durrant, *Polymers* **2016**, *8*.

[149] H. Liu, A. K. Rajasekaran, P. Moy, Y. Xia, S. Kim, V. Navarro, R. Rahmati, N. H. Bander, *Cancer research* **1998**, *58*, 4055.

[150] L. Wang, S. L. Jacques, L. Zheng, *Computer Methods and Programs in Biomedicine* **1995**, *47*, 131.

[151] R. Urso, P. Blardi, G. Giorgi, *European review for medical and pharmacological sciences* **2002**, *6*, 33.

[152] J. Liu, M. Yu, C. Zhou, S. Yang, X. Ning, J. Zheng, *Journal of the American Chemical Society* **2013**, *135*, 4978.

[153] Y. Zhang, L. Zhang, G. Yin, W. Ma, J. Li, Z. Zhou, F. Gao, *Molecular imaging and biology : MIB : the official publication of the Academy of Molecular Imaging* **2019**.

[154] E. A. Sykes, Q. Dai, C. D. Sarsons, J. Chen, J. V. Rocheleau, D. M. Hwang, G. Zheng, D. T. Cramb, K. D. Rinker, W. C. Chan, *Proceedings of the National Academy of Sciences of the United States of America* **2016**, *113*, E1142.

[155] C. W. Freudiger, W. Min, B. G. Saar, S. Lu, G. R. Holtom, C. He, J. C. Tsai, J. X. Kang, X. S. Xie, *Science* **2008**, *322*, 1857.

[156] I. Dagogo-Jack, A. T. Shaw, *Nature reviews Clinical oncology* **2018**, *15*, 81.

[157] B. Guo, J. Chen, N. Chen, E. Middha, S. Xu, Y. Pan, M. Wu, K. Li, C. Liu, B. Liu, *Advanced materials* **2019**, *31*, e1808355.

[158] W. R. Zipfel, R. M. Williams, W. W. Webb, *Nature biotechnology* **2003**, *21*, 1369.

[159] D. Fu, T. Ye, T. E. Matthews, G. Yurtsever, W. S. Warren, *Journal of biomedical optics* **2007**, *12*, 054004.

[160] D. y. Davydova, A. de la Cadena, D. Akimov, B. Dietzek, *Laser & photonics reviews* **2016**, *10*, 62.

[161] O. L. Muskens, N. Del Fatti, F. Vallee, *Nano letters* **2006**, *6*, 552.

[162] G. V. Hartland, *Chemical science* **2010**, *1*, 303.

[163] L. Tong, Y. Liu, B. D. Dolash, Y. Jung, M. N. Slipchenko, D. E. Bergstrom, J. X. Cheng, *Nature nanotechnology* **2011**, *7*, 56.

[164] J. Li, W. Zhang, T. F. Chung, M. N. Slipchenko, Y. P. Chen, J. X. Cheng, C. Yang, *Scientific reports* **2015**, *5*, 12394.

[165] T. Ye, D. Fu, W. S. Warren, *Photochemistry and photobiology* **2009**, *85*, 631.

[166] T. E. Matthews, I. R. Piletic, M. A. Selim, M. J. Simpson, W. S. Warren, *Sci Transl Med* **2011**, *3*, 71ra15.

[167] W. Min, S. Lu, S. Chong, R. Roy, G. R. Holtom, X. S. Xie, *Nature* **2009**, *461*, 1105.

[168] P. T. Dong, H. Lin, K. C. Huang, J. X. Cheng, *Science advances* **2019**, *5*, eaav0561.

[169] G. W. P. Van Pruissen, F. Gholamrezaie, M. M. Wienk, R. A. J. Janssen, *Journal of Materials Chemistry* **2012**, *22*, 20387.

[170] Y. Jiang, J. Li, X. Zhen, C. Xie, K. Pu, *Advanced materials* **2018**, *30*, e1705980.

[171] S. He, J. Song, J. Qu, Z. Cheng, *Chemical Society reviews* **2018**, *47*, 4258.

[172] C. Xie, X. Zhen, Q. Lei, R. Ni, K. Pu, *Advanced functional materials* **2017**, *27*, 1605397.

[173] Y. Jiang, D. Cui, Y. Fang, X. Zhen, P. K. Upputuri, M. Pramanik, D. Ding, K. Pu, *Biomaterials* **2017**, *145*, 168.

[174] J. Ulbricht, R. Jordan, R. Luxenhofer, *Biomaterials* **2014**, *35*, 4848.

[175] D. B. Chithrani, *Journal of Nanomedicine Research* **2014**, *1*.

[176] P. M. Beaujuge, J. R. Reynolds, *Chemical reviews* **2010**, *110*, 268.

[177] L. Cheng, K. Yang, Q. Chen, Z. Liu, *ACS nano* **2012**, *6*, 5605.

[178] J. Zhou, Z. Lu, X. Zhu, X. Wang, Y. Liao, Z. Ma, F. Li, *Biomaterials* **2013**, *34*, 9584.

[179] J. Yang, J. Choi, D. Bang, E. Kim, E. K. Lim, H. Park, J. S. Suh, K. Lee, K. H. Yoo, E. K. Kim, Y. M. Huh, S. Haam, *Angewandte Chemie* **2011**, *50*, 441.

[180] X. Wang, Y. Ma, X. Sheng, Y. Wang, H. Xu, *Nano letters* **2018**, *18*, 2217.

[181] J. F. Ponder Jr, A. M. Österholm, J. R. Reynolds, *Macromolecules* **2016**, *49*, 2106.

[182] J. F. Ponder Jr, A. M. Österholm, J. R. Reynolds, *Chemistry of Materials* **2017**, *29*, 4385.

[183] A. Lewinska, M. Wnuk, E. Slota, G. Bartosz, *Clinical and experimental pharmacology and physiology* **2007**, *34*, 781.

[184] P. Zanello, C. Nervi, F. F. De Biani, *Inorganic electrochemistry: theory, practice and application*, Royal Society of Chemistry, 2011.

[185] M. S. Abdou, F. P. Orfino, Y. Son, S. Holdcroft, *Journal of the American Chemical Society* **1997**, *119*, 4518.

[186] N. G. Horton, K. Wang, D. Kobat, C. G. Clark, F. W. Wise, C. B. Schaffer, C. Xu, *Nature photonics* **2013**, *7*.

[187] V. Ntziachristos, J. Ripoll, L. V. Wang, R. Weissleder, *Nature biotechnology* **2005**, *23*, 313.

[188] R. R. Anderson, W. Farinelli, H. Laubach, D. Manstein, A. N. Yaroslavsky, J. Gubeli III, K. Jordan, G. R. Neil, M. Shinn, W. Chandler, *Lasers in Surgery and Medicine: The Official Journal of the American Society for Laser Medicine and Surgery* **2006**, *38*, 913.

[189] N. Bosschaart, G. J. Edelman, M. C. Aalders, T. G. van Leeuwen, D. J. Faber, *Lasers in medical science* **2014**, *29*, 453.

[190] C. L. Bayer, S. Y. Nam, Y. S. Chen, S. Y. Emelianov, *Journal of biomedical optics* **2013**, *18*, 16001.

[191] H. D. Lu, B. K. Wilson, A. Heinmiller, B. Faenza, S. Hejazi, R. K. Prud'homme, *ACS applied materials & interfaces* **2016**, *8*, 14379.

[192] C. Xie, X. Zhen, Y. Lyu, K. Pu, *Advanced materials* **2017**, *29*, 1703693.

[193] R. A. Gatenby, R. J. Gillies, *Nature reviews cancer* **2004**, *4*, 891.

[194] Q. Miao, Y. Lyu, D. Ding, K. Pu, *Advanced materials* **2016**, *28*, 3662.

[195] Y. Jiang, P. K. Upputuri, C. Xie, Z. Zeng, A. Sharma, X. Zhen, J. Li, J. Huang, M. Pramanik, K. Pu, *Advanced materials* **2019**, *31*, e1808166.

[196] P. Huang, J. Lin, W. Li, P. Rong, Z. Wang, S. Wang, X. Wang, X. Sun, M. Aronova, G. Niu, R. D. Leapman, Z. Nie, X. Chen, *Angewandte Chemie* **2013**, *52*, 13958.

[197] X. Lu, P. Yuan, W. Zhang, Q. Wu, X. Wang, M. Zhao, P. Sun, W. Huang, Q. Fan, *Polymer Chemistry* **2018**, *9*, 3118.

[198] H. Shinto, T. Fukasawa, H. Aoki, S. Ito, M. Ohshima, *Colloids and Surfaces A: Physicochemical and Engineering Aspects* **2013**, *430*, 51.

[199] T. Fukasawa, S. Noguchi, H. Shinto, H. Aoki, S. Ito, M. Ohshima, *Colloids and Surfaces A: Physicochemical and Engineering Aspects* **2015**, *487*, 42.

[200] Y. Shi, S. Yang, D. Xing, *The Journal of Physical Chemistry C* **2017**, *121*, 5805.

[201] X. Zhen, X. Feng, C. Xie, Y. Zheng, K. Pu, *Biomaterials* **2017**, *127*, 97.

VITA

Jiayingzi Wu

Chemistry Department, Purdue University, United States

Education

Ph.D.	**Analytical Chemistry**, Purdue University, West Lafayette, IN, United States	2016-2020
M.S.	**Polymer Science**, The University of Akron, Akron, OH, United States	2013-2015
B.E.	**Polymer Science and Engineering**, Beijing University of Chemical Technology (BUCT), Beijing, China	2010-2013
Visiting student	Photonics Center, Boston University, Boston, MA, United States	2018-2020

Research Interest

Polymer materials

Biomedical imaging

Photoacoustic

Nanotechnology

Biosensing

PUBLICATIONS

1. **Jiayingzi Wu**, Hyeon Jeong Lee, Liyan You, Xuyi Luo, Tsukasa Hasegawa, Kai-Chih Huang, Peng Lin, Timothy Ratliff, Minoru Ashizawa, Jianguo Mei*, Ji-Xin Cheng*. "*Functionalized NIR-II Semiconducting Polymer Nanoparticles for Single-cell to Whole-Tumor Imaging of PSMA-Positive Prostate Cancer*" Submitted to Small.

2. **Jiayingzi Wu**, Liyan You, Jiazhi He, Ji-Xin Cheng*, and Jianguo Mei*. "*Stably doped semiconducting polymer as a water-soluble photoacoustic imaging probe with broad absorption in the NIR-II window and pH-sensitivity"* Manuscript in preparation.

3. **Jiayingzi Wu**, Liyan You, Jiazhi He, Ji-Xin Cheng*, and Jianguo Mei*. "*Semiconducting Polymers for Bacteria Detection"* Manuscript in preparation.

4. **Jiayingzi Wu**, Liyan You, Lu Lan, Hyeon Jeong Lee, Saadia T. Chaudhry, Rui Li, Ji-Xin Cheng*, and Jianguo Mei*. "*Semiconducting Polymer Nanoparticles for Centimeters-Deep Photoacoustic Imaging in the Second Near-Infrared Window*" Advanced Materials, **2017**, 29 (41)

5. Yimin Huang, Ying Jiang, **Jiayingzi Wu**, Xuyi Luo, Cheng Yang*, Ji-Xin Cheng*, and Jianguo Mei*. "*Semiconducting Polymer Nanoparticles for Neuron Stimulation"* Manuscript in preparation.

6. Lan, Lu, Kaiming Liu, Yan Xia, **Jiayingzi Wu**, Rui Li, Pu Wang, Linda K. Han, and Ji-Xin Cheng. "An optoacoustic guide with augmented reality system towards precision breast conserving surgery (Conference Presentation)." International Society for Optics and Photonics, **2017**